DEVELOPMENT OF A SUBSTRATE WITH PHOTO-MODULATABLE RIGIDITY FOR PROBING SPATIAL AND TEMPORAL RESPONSES OF CELLS TO MECHANICAL SIGNALS

A Dissertation Presented

By

Margo Tilley Frey

Submitted to the Faculty

of the

University of Massachusetts Graduate School of Biomedical Sciences, Worcester

and the

Department of Biomedical Engineering at Worcester Polytechnic Institute, Worcester

in partial fulfillment of the requirements for the

Degree of Doctor of Philosophy

in

Biomedical Engineering and Medical Physics

July 2008

DEVELOPMENT OF A SUBSTRATE WITH PHOTO-MODULATABLE RIGIDITY FOR PROBING SPATIAL AND TEMPORAL RESPONSES OF CELLS TO MECHANICAL SIGNALS

A Dissertation

Submitted to the Faculty

of the

WORCESTER POLYTECHNIC INSTITUTE

and

THE UNIVERSITY OF MASSACHUSETTS MEDICAL SCHOOL

in partial fulfillment of the requirements for the

Degree of Doctor of Philosophy

in

Biomedical Engineering and Medical Physics

July 2007

By

Margo T. Frey

APPROVED:

Yu-Li Wang, Ph.D.
Professor, Advisor
Department of Physiology
University of Massachusetts Medical School

Elizabeth Ryder, Ph.D.
Associate Professor
Department of Biology and Biotechnology
Worcester Polytechnic Institute

Glen Gaudette, Ph.D.
Associate Professor
Biomedical Engineering Department
Worcester Polytechnic Institute

Joyce Wong, Ph.D.
Associate Professor
Biomedical Engineering Department
Boston University

Peter Grigg, Ph.D.
Professor
Department of Physiology
University of Massachusetts Medical School

Kristen Billiar, Ph.D.
Associate Professor
Biomedical Engineering Department
Worcester Polytechnic Institute

Anthony Carruthers, Ph.D.
Dean of the Graduate School of Biomedical Sciences
University of Massachusetts Medical School

Grant McGimpsey
Associate Provost for Research and Graduate Studies ad interim
Worcester Polytechnic Institute

DEDICATION

For my husband, Gregory Frey, you have exceeded your pledge to support me in this process. Thank you for your love, encouragement, and support. I will never forget all you have done and all you make possible. For my daughters, Caitlin and Kristin, you have managed with less of me in the hopes that this will serve as an example for you to always listen to your inner voice and follow your dreams. Know that when you believe in yourself, you can achieve whatever it is you put your mind to with a little perseverance.

ACKNOWLEDGEMENTS

There are many who have contributed to my ability to complete this endeavor to whom I am most grateful for. First to thank is Dr. Yu-Li Wang, who has been more than an advisor, but a beloved mentor. His gentle guidance, understanding, and support, both professional and personal, have made this not only a productive, but enjoyable journey. I have been truly blessed to be his understudy. I thank my Thesis Committee Chair, Dr. Kristen Billiar, for his technical guidance, encouragement, and support from early on. Also to thank for their time and guidance are the other (past and present) members of my thesis committee: Drs. Glen Gaudette, Peter Grigg, Elizabeth Ryder, Joyce Wong, and George Pins. For all the moral support, technical support, and comic relief, I thank several fellow colleagues: Angela Throm, Katie Bush, Corrie Painter, Kevin Cornwell, Brett Downing, and Jessica Crowley. For creating an environment that makes being at work more enjoyable, I thank all the past and present members of the Wang Lab (Karen Beningo, Minakshi Guha, Weihui Guo, Mian Zhou, Javier Satulovsky, and Jin-Jia Hu) and the friendly staff on the third floor of Biotech IV. Accomplishing this endeavor while starting a family would not have been possible without several others that deserve a tremendous thank you. Most notably, I thank my husband, Gregory Frey for all his support and encouragement. Other notable people providing their time and/or moral support have been my parents-in-law, Irene and James Frey, my parents, David and Carole Tilley, my sister and brother, Anne O'Connor-Smith and David Ryan Tilley, and our nanny, Regina Leduc.

COPYRIGHT NOTICE

Parts of this thesis have appeared in the following publications:

Frey, M.T., Tsai, I.Y., Russell, T.P., Hanks, S.K., and Wang, Y.L., Cellular Responses to 3D Substrate Topography: Role of Myosin II and Focal Adhesion Kinase, *Biophysical Journal* 90:3774-3782 (2006).

Guo, W.H., **Frey, M.T.,** Burnham, N.A., and Wang, Y.L., Substrate Rigidity Regulates the Formation and Maintenance of Tissues, *Biophysical Journal*, 90:2213-2220 (2006).

Frey, M.T., Engler, A., Lee, J., Wang, Y.L., and Discher, D.E., Microscopic Methods for Measuring the Elasticity of Gel Substrates for Cell Culture: Microspheres, Microindenters, and Atomic Force Microscopy. *Cell Mechanics, Methods in Cell Biology.* 83:45-63 (2007). Elsevier, Inc.

Frey, M.T. and Wang, Y.L., A Photo-Modulatable Material for Probing Cellular Responses to Substrate Rigidity. (Submitted).

Material in Table 1.1 is adapted with permission from the following publication:

Cukierman, E., Roumen, P., Stevens, D.R., Yamada, K.M., Taking Cell-Matrix Adhesions to the Third Dimension, *Science*, 294:1708-1712 (2001).

Figure 1.1 is reprinted here with permission from:

Wozniak, M. A., Modzelewska, K., Kwong, L. and Keely, P.J., Focal adhesion regulation of cell behavior, Biochim Biophys Acta, 1692: 103-119 (2004).

Figure 1.2 is reprinted here with permission from the following website:

http://www.biocarta.com/pathfiles/h_INTEGRINPATHWAY.asp

ABSTRACT

Topographical and mechanical properties of adhesive substrates provide important biological cues that affect cell spreading, migration, growth, and differentiation. The phenomenon has led to the increased use of topographically patterned and flexible substrates in studying cultured cells. However, these studies may be complicated by various limitations. For example, the effects of ligand distribution and porosity are affected by topographical features of 3D biological constructs. Similarly, many studies of mechanical cues are compounded with cellular deformation from external forces, or limited by comparative studies of separate cells on different substrates. Furthermore, understanding cell responses to mechanical input is dependent upon reliable measurements of mechanical properties. This work addresses each of these issues.

To determine how substrate topography and focal adhesion kinase (FAK) affect cell shape and movement, I studied FAK-null (FAK -/-) and wild type mouse 3T3 fibroblasts on chemically identical polystyrene substrates with either flat surfaces or micron-sized pillars, I found that, compared to cells on flat surfaces, those on pillar substrates showed a more branched shape, an increased linear speed, and a decreased directional stability, which were dependent on both myosin-II and FAK.

To study the dynamic responses to changes in substrate stiffness without other confounding effects, I developed a UV-modulatable substrate that softens upon UV irradiation. As atomic force microscopy (AFM) proved inadequate to detect microscale changes in stiffness, I first developed and validated a microsphere indentation method

that is compatible with fluorescence microscopy. The results obtained with this method were comparable to those obtained with AFM. The UV-modulatable substrates softened by ~20-30% with an intensity of irradiation that has no detectable effect on 3T3 cells on control surfaces. Cells responded to global softening of the substrate with an initial retraction followed by a gradual reduction in spread area. Precise spatial control of softening is also possible - while there was little response to posterior softening, anterior softening elicited a pronounced retraction and either a reversal of cell polarity or a significant decrease in spread area if the cells move into the softened region.

In conclusion, these techniques provide advances in gaining mechanistic insight into cellular responses to topographical and mechanical cues. Additionally, there are various other potential applications of the novel UV-softening substrate, particularly in regenerative medicine and tissue engineering.

TABLE OF CONTENTS

LIST OF TABLES

LIST OF FIGURES

CHAPTER 1. INTRODUCTION

1.1. Introduction

The processes of cellular growth, differentiation, and motility are important during embryonic development, in homeostasis of adult animal tissues, and in wound healing of damaged tissues. When these processes are unregulated, they are responsible for tumorigenesis and cancer metastasis. During development, cells must correctly follow migratory and growth cues in order to proliferate and organize properly to form tissues and organs. In the developed organism, the physical microenvironment and architecture of the tissue must be maintained during the continuous flux of normal cellular/tissue turnover. Cells must also respond appropriately to a variety of mechanical stimuli, such as hydrostatic pressure, compression, fluid flow, and shear. Damaged tissues must be repaired properly, or else fibrosis and cancer can set in. Fibroblast cells are an integral component of many tissues and play an active role in many of these processes and responses.

While regulation of cellular behavior in response to chemical cues has occupied the attention of biologists for decades, the importance of cellular responses to physical signals, such as topography and stiffness, has only recently gained significant attention. Although the phenomenon of contact guidance has been known for over fifty years and many studies to determine cellular responses to various topographical features have resulted, the mechanisms responsible for these responses remain largely unexplored. Similarly, only within the few decades have studies revealed that cell behavior can be

controlled by physical interactions between cells and their surrounding extracellular matrix (ECM). For example, studies using polyacrylamide (PA) gels of varied stiffness revealed that the mechanical properties of the substrate affect cellular growth, spreading and migration (Pelham and Wang 1997; Lo, Wang et al. 2000; Wang, Dembo et al. 2000).

How are these complex responses regulated? The process by which external physical signals are transduced into intracellular biochemical signals, termed mechanotransduction, likely occurs through cellular adhesions. Cells adhere to their extracellular matrix (ECM) through focal adhesions, in which cytosolic proteins are recruited and anchor the membrane-bound complex to the actin cytoskeleton. Even small changes in the magnitude or distribution of mechanical forces can trigger redistribution of these cytosolic proteins within adhesion sites. This gives rise to multiprotein signaling complexes that are likely relayed to the nucleus to affect various cellular functions.

For example, the proteins focal adhesion kinase (FAK) and myosin-II are required in the response to substrate stiffness (Pelham and Wang 1997; Wang, Dembo et al. 2001; Lo, Buxton et al. 2004). The mechanisms underlying the responses to topographical features may be similar to those for mechanical signals. Therefore, I hypothesized that these proteins were also required in the response to topography. I was able to confirm this hypothesis using FAK-mutant (FAK -/-) and -rescued fibroblasts and a potent myosin II inhibitor, blebbistatin, on 3T3 fibroblasts on chemically identical flat and pillar substrates.

Although many proteins have been identified as critical in responding to physical cues, how and when the many cytosolic proteins are recruited to these complexes and their downstream mechanisms of action are still largely unknown. The recent appreciation for the three-dimensional dynamics of signal complex formation at focal adhesions has led to a need for understanding the spatial and temporal elements of mechanotransduction. Since current studies of mechanotransduction are done on separate stiff and soft PA substrates in parallel fashion, it is difficult to determine the transition dynamics of cell behavior during changes in substrata stiffness. This led to the motivation to create a substrate with modulatable stiffness such that the dynamics of the response could be visualized within the same cell. I was able to prepare and characterize a cell culture substrate with UV-modulatable stiffness in order to perform mechanotransduction studies at high spatial and temporal resolution.

1.2. Connective tissue

Cells *in vivo* are surrounding by their ECM, such as within connective tissue. Connective tissues provide a major portion of the architectural framework and structural support for the body, and their cells are integral in the repair of almost every tissue and organ (described in (Alberts, Johnson et al. 2002). Connective tissues support, both structurally and functionally, the basement membranes (non-cellular mixtures of carbohydrates and proteins) that underlie the vast number of epithelial tissues of the body. Connective tissues consist of specific cells and mostly ECM, in addition to a three-

dimensional composition of various cytokines, growth factors, ions, water, and adhesive proteins that are secreted by the cell.

Connective tissue ECM mediates at least a portion of the physical interactions between cells and the environment. It is comprised mostly of collagen fibers and a large variety of other adhesive proteins, such as fibronectin. Collagen lends structure and strength to most body structures, such as skin, blood vessels, and bone (described in (Dee, Puleo et al. 2002). Nineteen types of collagen have been identified, accounting for at least 25% of the total body protein in higher vertebrates. The highly organized structure of collagen fibrils and fibers is responsible for their high uniaxial tensile strength. The primary structure of collagen is represented by the motif, Gly-Pro-Hyp-Gly-X-Y, where X and Y can be any amino acid. The polypeptide chains form left-handed helices called α-chains. Three α-chains then wind around each other to form a right-handed procollagen superhelix. The type of collagen is determined from the individual α-chains in the triple helix; types I, II, III, V, XI are the main types of collagen found in connective tissues. Collagen molecules are formed by secretion of the procollagen molecule, followed by enzymatic cleavage of the propeptide region at its ends. Collagen molecules then self-assemble into collagen fibrils in a "quarter-stagger" array, resulting in characteristic striations every 67 nm.

Fibronectin (FN) is a large glycoprotein found in all vertebrates (Reviewed in (Wierzbicka-Patynowski and Schwarzbauer 2003). It exists in multiple isoforms. Plasma, or soluble, FN circulates in the blood and other bodily fluids and is thought to enhance blood clotting and wound healing. All the other forms of FN form highly

insoluble fibrils, which assemble on the cell surface at fibrillar adhesions (discussed later) before deposition into the ECM. FN is a dimer composed of two subunits, 220 kDa each, joined near their carboxyl termini by two disulfide bonds. Each subunit is comprised of repeats of three types of functionally distinct domains, classified as type I, II and III repeats. FN is multifunctional due to the affinity of its domains with various cell surface receptors, collagen, and heparin. The cell-binding tripeptide, Arg-Gly-Asp (RGD), found in one of the type III repeats is of particular importance as it mediates cell adhesion; cell attachment and spreading can be promoted on solid surfaces by coupling short peptides containing the RGD sequence (Rajagopalan, Marganski et al. 2004). Soluble sequences that compete with RGD for cell binding also effectively compete with FN for the binding sites on cells, inhibiting attachment to the FN matrix (Dedhar, Ruoslahti et al. 1987; Gehlsen, Argraves et al. 1988).

Cells in connective tissues, including fibroblasts, smooth muscle cells, adipocytes, osteoblasts, chondrocytes, and vascular endothelial cells, are potentially interconvertible (Alberts, Johnson et al. 2002). These cells are typically stable, but proliferate in response to appropriate stimuli, such as tissue injury. Fibroblasts seem to be the most versatile. The adaptability of their differentiation is an important feature of their response to many types of injury.

1.3. Tissue injury and wound healing

Tissue injury, either acute or chronic, can result from infections and autoimmununne reactions, exposure to toxins and radiation, and trauma. It can involve

either cell death or damage to the ECM components. Wound healing is the body's natural and automatic response to tissue injury that serves to replace damaged blood vessels and connective tissues. Wound healing involves a series of highly coordinated processes that overlap in time, regulated by the balanced action of growth factors, cytokines, and proteases, in addition to unknown chemical compounds and histological changes (Reviewed in (Martin 1997; Eckes, Zigrino et al. 2000; Darby and Hewitson 2007).

Wound healing in vascularized tissues is first triggered by the damage to blood vessels in the form of a coagulated blood clot (Martin 1997). The blood clot provides a provisional matrix for cells to attach to and migrate over during the healing process. Growth factors released by cells during inflammation can either induce cell migration by serving as a chemoattractant or increasing the rate of random migration. Additionally, growth factors can act in an autocrine manner, affecting the same type of cell that released them, or in a paracrine manner, affecting other cell types in surrounding tissues. For example, growth factors released from platelets during coagulation and from leukocytes during inflammation may cause surrounding cells such as fibroblasts to produce their own growth factors. In addition to chemical factors, the distinct physical properties of the blood clot may contribute to the wound healing response.

The release of growth factors during the inflammatory stage is critical for the proliferative phase that follows. Activation and/or expression of cell-membrane receptors are induced during this proliferative phase. Both cell-cell and cell-membrane adhesions (discussed later) are critical to the regulation of cell migration and proliferation

in wound healing. In the case of stimulated cell migration, collagen receptors are downregulated and integrins that bind fibrin, FN, and vitronectin are upregulated (Juhasz, Murphy et al. 1993). FN, in soluble form, circulates in the blood and other body fluids and enhances this focal adhesion-mediated response. In contrast, insoluble fibrillar FN and other ECM proteins are secreted and deposited from the margin of the wound inward, typically by fibroblasts, further stimulating cellular migration into the wound. For the cells to migrate through the fibrin clot and the remnants of the original ECM, upregulation of collagenase and matrix metalloproteinases (MMPs), which cleave specific matrix proteins, are also required (Galvez, Matias-Roman et al. 2001).

Repopulation of the wound site with cells is achieved by initiation of mitosis of normally quiscent cells at the wound margins. New blood vessels are formed within the wound, followed by the appearance of granulation tissue. Early granulation is marked by the synthesis of proteoglycans by fibroblasts, while later stages of granulation involve collagen synthesis. It is in this latter stage that the connective tissue is compacted and the wound is closed (Martin 1997). Myofibroblasts, contractile fibroblasts that have been activated to express increased levels of alpha smooth muscle actin (α-SMA), compact the wound by tugging on themselves and the collagen fibers. A variety of factors, such as apoptotic cell fragments, matrix components, growth factors, the immune response, oxidative stress, or mechanical cues can activate myofibroblasts (Olaso, Salado et al. 2003; Bataller, Sancho-Bru et al. 2005). For example, myofibroblast precursor cells in culture undergo activation in response to increasing substrata stiffness (Georges, Hui et

al. 2007). The last phase of wound healing is remodeling, whereby the myofibroblastic cells apoptose and return the tissue to its quiescent state.

1.4. Tensional homeostasis: Implications for fibrosis, cancer and metastasis

What triggers regulation of apoptosis to conclude the wound healing process is unknown, but cell-cell contact inhibition or other mechanical cues are likely involved (Dee, Freer et al. 2002). If these cues are ignored or if inflammation is chronic (e.g. viral hepatitis), an excess deposition of ECM occurs such that normal tissue is replaced with stiffer permanent scar tissue, called fibrosis. For example, early stages of liver fibrosis are preceded by an increase in liver stiffness, likely a result of matrix cross-linking in addition to increased deposition of the ECM and other factors (Georges, Hui et al. 2007).

Tissue injury may lead to changes in the morphology, function, and phenotype of cells. While these changes are short-term and reversible in the case of normal wound healing, they can also be permanent and irreversible, leading to cell death in extreme cases. During normal wound healing, the repair process is regenerative; injured cells are replaced by healthy cells of the same type and the tissue regains normal function. When this process is not controlled properly, such as during chronic inflammation, the wound healing process can become pathogenic, causing hypertrophy (increase in cell size), atrophy (decrease in cell size and/or function), necrosis (cell death), hyper- or neoplasia (increase in cell numbers), metaplasia (change of the cell type), changes in phenotype (altered production of characteristic proteins within or excreted by the cell), and fibrosis (stiff scar tissue from excess ECM deposition).

There is also accumulating evidence that altered physical properties of the tissue microenvironment may contribute to the development of cancer, as proposed by Ingber and coworkers over 25 years ago (Ingber, Madri et al. 1981). The original paradigm of cancer development involves neoplasia caused by carcinogen-mediated damage to the DNA, potentially with malignant invasion of the surrounding connective tissue stroma (the first step in metastasis). As a result, cancer research has generally focused on the genetic causes and downstream biochemical signaling mechanisms. However, cancer is often detected and later diagnosed based on palpation of a rigid mass within a more compliant tissue, and patients with "rigid" lesions are at higher risk for metastasis (Colpaert, Vermeulen et al. 2001; Akiri, Sabo et al. 2003). The stiffness of many diseased tissues is greater than healthly tissues (Fig. 1.1; (Levental, Georges et al. 2007).

Early experiments in the field of cancer research support the notion that both structural and mechanical changes in the tissue microenvironment may contribute to the development of cancer. For example, cancer formation can be triggered by implantation of a rigid piece of metal or plastic, yet no tumors are produced when the same material is implanted as a powder (Bischoff and Bryson 1964). Small increases in tissue stiffness can perturb normal tissue architecture and enhance cellular growth (Zhong, Kinch et al. 1997; Paszek, Zahir et al. 2005) and "neoplastic transformation" occurs only after the normal tissue architecture has been disorganized sufficiently (Wiseman and Werb 2002).

Many adult tissues undergo continuous turnover, during which their cells and ECM are continually removed and replaced. Therefore, it is not individual cellular or molecular components that are maintained over time, but the 3D architecture of the tissue

(Ingber 2008). The tissue architecture will determine cell shape, or morphology, as a result of adhesive contacts between the two. Tension is generated within an object when there is pulling force on one end that is resisted at the opposite end. In the case of a cell, tension results from the forces generated by the cytoskeleton within the cell (actin and myosin), which are then resisted by adhesions to the ECM, substrata, or other cells that anchor the cell. The net result determines cell shape, such that changes in the architecture of the ECM will cause profound changes in cellular morphology.

Normal adult tissues that turnover properly do not exhibit changes in the ECM structure, yet these occur during early phases of cancer formation, prior to the development of a palpable tumor (Lu, Huang et al. 2000; Li, Chen et al. 2001). In addition, dissolution of local basement membrane occurs before cell proliferation during normal growth of epithelium (Vasiliev 1958) and endothelium (Ausprunk and Folkman 1977). Most ECM-degrading matrix metalloproteinases (MMPs) are upregulated in cancers of the epithelium and are secreted by stromal cells within and around the tumor mass (Sternlicht, Bissell et al. 2000). Thus ECM remodeling likely drives growth, not the other way around. For example, overexpression of the ECM-degrading enzyme, stromelysin, causes normal breast epithelial cells to transform into cancerous tissue in transgenic mice (Sternlicht, Lochter et al. 1999). These cells were also found to exhibit genetic abnormalities as a result of changes in the tissue architecture (Lochter, Werb et al. 1999; Sternlicht, Lochter et al. 1999; Sternlicht, Bissell et al. 2000).

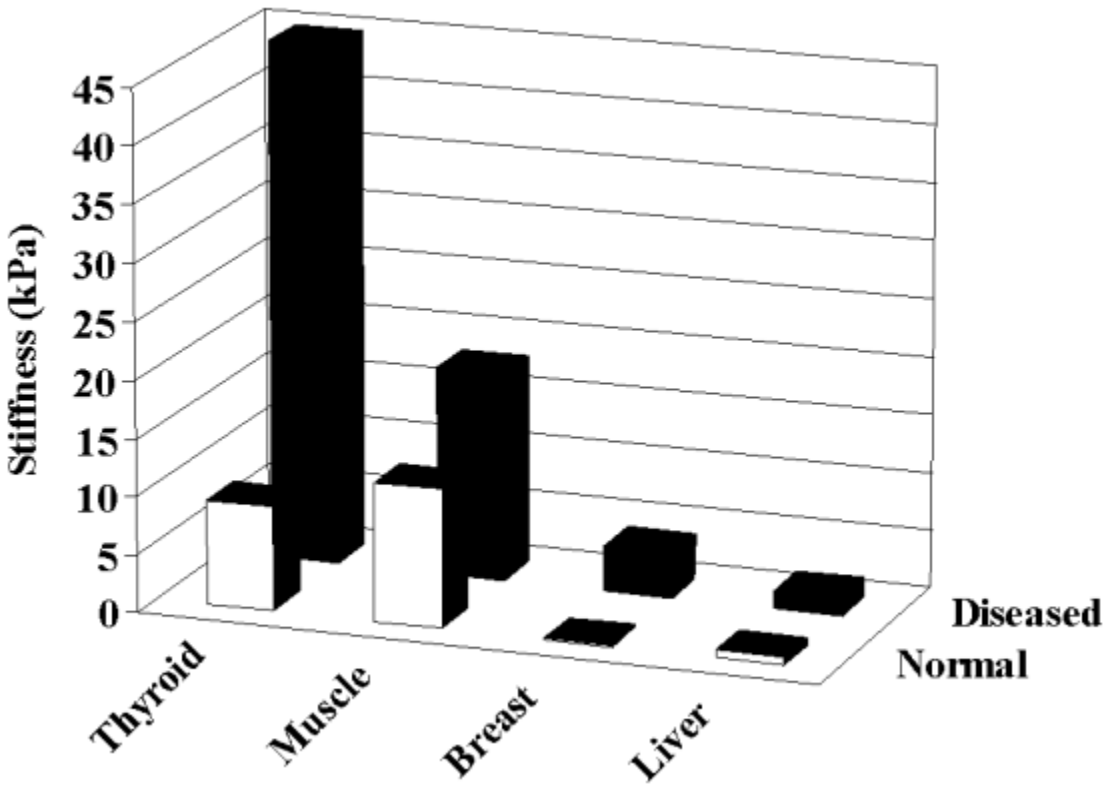

Figure 1.1. Stiffness of various normal and diseased tissues

Disease increased tissue stiffness in a variety of tissues, as measured by atomic force microscopy (values from Levental, Georges et al. 2007).

Thinning of a basement membrane will cause it to stretch out more than its surrounding, thicker regions, thereby stretching the associated cells. Mechanical stresses that are exerted locally on the cells at the sites of these adhesions will thus increase as a result of thinning-induced stretching, increasing the tension within the cell. Stretched cells are also more sensitive to soluble mitogens (Folkman and Moscona 1978; Singhvi, Kumar et al. 1994; Chen, Mrksich et al. 1997).

These alterations in cell morphology likely stimulate proliferation (Folkman and Moscona 1978). Normal cells fail to divide when confined to a spherical shape, either by culturing them in suspension or by allowing them to adhere but not spread. Normal cells require attachment to a rigid matrix to proliferate, yet cancer cells lose this "shape dependence" (Wittelsberger, Kleene et al. 1981; Wang, Dembo et al. 2000). Furthermore, application of stress to integrins induces similar signaling responses in round versus spread cells (Meyer, Alenghat et al. 2000), yet spread cells proliferate whereas round cells undergo apoptosis (Chen, Mrksich et al. 1997). Therefore, uninhibited growth could result from altered tissue morphology and associated changes in microstructure.

Tumor development may be influenced by altered mechanical properties of the ECM, and there is evidence that cancers can originate within the connective tissue stroma (Maffini, Soto et al. 2004). Increased breast tissue density, associated with both epithelial proliferation and stromal fibrosis, is a leading risk factor for breast carcinoma and is associated with approximately 30% of all breast cancers (Boyd, Lockwood et al. 1998).

Conversely, grafting mammary epithelial cancer cells into healthy stroma encourages normal growth (Maffini, Calabro et al. 2005).

The rigidity of tumors likely results from matrix stiffening linked to fibrosis (Paszek and Weaver 2004), an increased stiffness, or elastic modulus, of transformed cells (Beil, Micoulet et al. 2003) due to enhanced Rho-mediated cytoskeletal contractility (Fritz, Just et al. 1999), and elevated pressure of interstitial tissue from the perturbed vasculature and expansive growth of the tumor (Padera, Stoll et al. 2004). A highly stiff matrix or high Rho activity (discussed later) could facilitate tumor invasion through enhanced adhesion that promotes migration (Paszek, Zahir et al. 2005). Indeed, "stiff" tumors show altered integrin levels (Guo and Giancotti 2004). Furthermore, stromal fibroblasts within tumors may promote tumor progression and metastasis, as tracks created by stromal fibroblasts co-cultured with squamous cell carcinoma cells within dense matrices were sufficient to enable invasion of the cancer cells (Gaggioli, Hooper et al. 2007). Therefore, the expression of a malignant phenotype could be driven by increased tissue stiffness through force-dependent regulation of integrin expression, activity, or adhesions. A chronic increase in cytoskeletal tension, as a result of sustained matrix stiffness in chronic inflammation or fibrosis, and/or oncogene amplification in cancer (potentially as a result of shape-stimulated growth), could drive the assembly of adhesions to enhance growth and perturb tissue organization, thus promoting malignant transformation (Paszek, Zahir et al. 2005). Since chronic fibroproliferative diseases collectively account for nearly 45% of all deaths in the developed world (Wynn 2008), an

understanding of how cells respond to mechanical cues has significant clinical implications.

1.5. Cell-ECM adhesions: elements of mechanosensing and mechanotransducing

To understand the process by which cells sense and respond to mechanical forces, the path by which these forces are transmitted through tissues and across the cell surface must first be identified. Forces applied to tissues would be distributed to individual cells through their adhesions to the ECM and to neighboring cells, mediated by focal adhesions and by cadherin-dependent adhesions respectively (Takeichi 1995; Steinberg and McNutt 1999). These adhesion structures are the likely sites by which cells transfer mechanical signals across their surface (Ingber 2003), as application of mechanical stresses to other transmembrane receptors fails to produce similar responses. For instance, stretching isolated cytoskeletons causes binding of focal adhesion proteins (Sawada and Sheetz 2002). The focal adhesion is probably not a unique molecular mechanosensor, as complexes of adherens junctions and the Z-disks in striated muscle are likely analogous structures in other cellular systems (Bershadsky, Balaban et al. 2003). Similarly, cadherins and selectins may function in an analogous manner in transmitting forces between neighboring cells (Ingber 2003).

Different combinations of transmembrane α- and β- integrin subunits on the plasma membrane mediate different types of ECM ligand binding (e.g. α5β1 and αvβ3 integrin binding of the RGD sequence on FN (Stupack and Cheresh 2002)). Cytoplasmic domains in the α-subunit appear to regulate the localization of the proper integrins to the

ligand (Ylanne, Chen et al. 1993), whereas the cytoplasmic tail of the β-subunit appears to be important for regulating binding affinity (O'Toole, Ylanne et al. 1995). The cytoplasmic tail of the β-subunit is also the binding site for a complex battery of structural (e.g., vinculin, α-actinin, and the actin cytoskeleton) and signaling proteins (e.g. focal adhesion kinase, or FAK, and src (Geiger, Bershadsky et al. 2001). Although the exact functions of these signaling molecules are unclear, they presumably play the important role of transmitting and translating extracellular physical or mechanical signals into intracellular chemical signals, potentially using forces generated by the cytoskeleton as part of the probing mechanism. Although this process, termed mechanotransduction, occurs locally at the cell periphery, the forces and biochemical signals are propagated throughout the cell (Choquet, Felsenfeld et al. 1997; Riveline, Zamir et al. 2001; Galbraith, Yamada et al. 2002).

Furthermore, the signals are returned to the cell periphery through a feedback mechanism, as mechanical forces generated by the intracellular actin-myosin contractile cytoskeleton are transferred to the cell surface integrin receptors, which in turn cause changes in the assembly and/or disassembly of crosslinking, scaffolding, and signaling molecules. Signaling events within the cell, presumably reaching to the nucleus, provide the feedback, or 'inside-out signaling', that regulates integrin expression and affinity. Thus, adhesion formation, maturation, and disassembly are also regulated from the inside out (Wozniak, Modzelewska et al. 2004).

1.6. Regulation of cell migration by cell-ECM adhesions

Migration of a cell through an ECM or on any substrate involves at least four interdependent elements: leading edge protrusion, attachment to the substrate, contraction, and detachment of the rear end (Friedl and Brocker 2000). Protrusion of the leading edge likely also serves a mechanosensory function, whereby the cell detects the physical state of the ECM, including both chemical (e.g. growth factors, glycoproteins, etc.) and physical parameters (architecture, ligand distribution, stiffness, forces, etc) (Janmey and Weitz 2004). The protrusive structures contain actin and are classified as either lamellipodia or filopodia (Fig 1.2). Lamellipodia are characterized by actin filaments arranged in a homogenous network, and small radial bundles embedded in the network. In contrast, filopodia are actin bundles that protrude from the periphery. Lamellipodia formation and ruffling are induced by the small GTPase Rac (Ridley, Paterson et al. 1992), whereas filopodia are induced by a different small GTPase, cdc42 (Lim, Bu et al. 2008).

These protrusive structures may localize and harness actin polymerization for cell migration. Evidence suggests that actin polymerization is sufficient to account for the forces of protrusion (Abraham, Krishnamurthi et al. 1999), yet this would require a balance of steady state maintenance and transient responses. The steady state may be achieved through the normal assembly-disassembly dynamics of actin filaments, whereby growth at the one end is balanced by shortening at the other end of the filament.

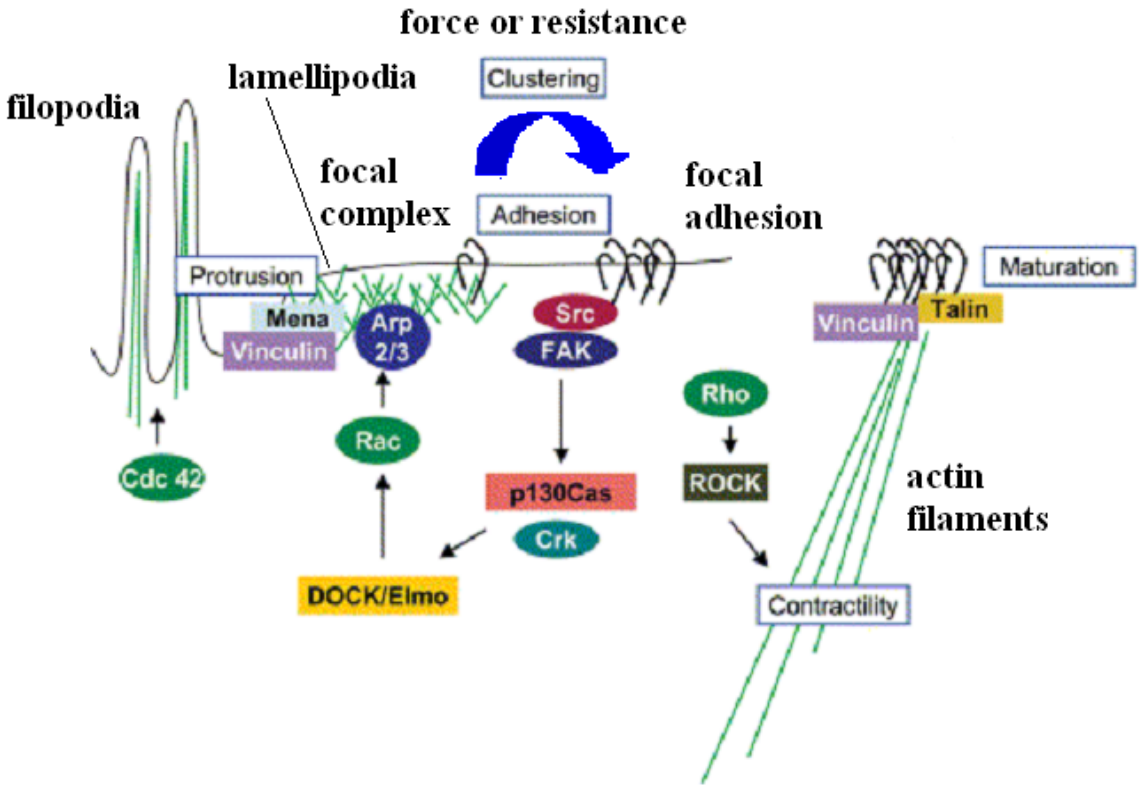

Figure 1.2. Protrusion and adhesion dynamics

Filopodia and lamellipodia are distinct types of protrusions. Within lamellipodia, adhesions initially form as focal complexes. If external force or resistance is present, integrins will cluster causing focal complexes to "mature" or evolve into focal adhesions that are connected to the cellular contractile apparatus. (Adapted from Wozniak, M. et al., Biochim Biophys Acta, 2004)

Transient responses likely occur in response to adhesions and downstream intracellular signals.

Remodeling and detachment of adhesions, combined with intracellular contractile forces, propel the cell body and drive net cell displacement. Thus, migration is made possible through the coordinated effort at hundreds of adhesions that are transiently formed, remodeled, and disassembled (Beningo, Dembo et al. 2001).

1.7. Types of cell-ECM adhesions and molecules of mechanotransduction

Structurally and functionally distinct types of adhesions are formed in response to biochemical and physical properties of the ECM (Katz, Zamir et al. 2000). Based on the colocalization of specific integrins and/or cytoskeletal proteins, four different structures of adhesions have been characterized: fibrillar adhesions, 3D-matrix adhesions, focal complexes, and focal adhesions (Table 1.1; Cukierman, Pankov et al. 2001). Fibrillar adhesions are distinct types of adhesions responsible for assembling FN into fibrils. 3D-matrix adhesions are more like those found *in vivo* within healthly tissues, whereas focal complexes and focal adhesions may be more representative of those formed during wound healing and potentially within stiffer, diseased tissues.

Fibrillar adhesions are distinct from the other types of adhesions by their more elongated morphology, localization to more central regions of the cell, and different composition of integrins ($\alpha_5\beta_1$) and intracellular proteins (Zaidel-Bar, Ballestrem et al. 2003). Whereas some other molecules like collagen can self-assemble into fibers, FN

Table 1.1. Molecular composition of cell-matrix adhesions

Molecule	Fibrillar Adhesion	3D-matrix adhesion	Focal Adhesion (mature)
α_5 integrin	+	+	-*
β_1 integrin	+	+	+
β_3 integrin	-	-	+
Fibronectin (fibrillar)	+	+	-*
α-actinin	+/-	+	+
F-actin	+	+	+
Talin	+	+	+
Tensin	+	+	+
Vinculin	-	+	+
Phosphotyrosine	-	+	+
FAK	-	+	+
FAK P397	-	-	+
Paxillin	-	+	+

(*Absent other than small amounts localized only to the periphery of the structure.)

(Adapted with permission from (Cukierman, Pankov et al. 2001).)

molecules must be assembled into fibrils on the cell surface. Fibrillar adhesions are the sites of FN binding and assembly on fibroblast surfaces, where they are stretched to expose cryptic binding sites that allows the molecules to bind one another prior to being deposited into the ECM (Zhong, Chrzanowska-Wodnicka et al. 1998). Integrins are required for binding and the contractile actin and myosin cytoskeleton are required to generate the tension necessary for this process.

Each other type of adhesion may represent a distinct strategy among a spectrum of ways to overcome differential biophysical constraints imposed by the ECM, such as the spatial size and flexibility of the ECM relative to the cell body (Friedl, Zanker et al. 1998; Friedl and Brocker 2000) (Table 1.1). Each of these types of adhesion may create different arrangements of signaling molecules within the cytoskeleton, differentially affecting intracellular signaling pathway(s). The mechanisms are complex and still poorly understood.

The 3D-matrix adhesion was discovered in cells cultured in ECM recovered from native tissues, or tissue-derived 3D matrices, and in matrices naturally deposited by fibroblasts in culture, or cell-derived 3D matrices (CDM) (Cukierman, Pankov et al. 2001). This type of adhesion is dependent upon both a very pliable structure and a 3D architecture, as increasing the stiffness of these matrices by crosslinking with gluteradehyde or plating the cells on the same CDM material in 2D abolished their formation. Both the 3D-matrix adhesion structure and the cellular morphology within the 3D-CDM are characteristic of those of cells in normal tissues *in vivo*, which lack stress

fibers and focal adhesions (Bondy, Wilson et al. 1985; Cukierman, Pankov et al. 2002; Beningo, Dembo et al. 2004).

In contrast, cells in stiffer 3D matrices and on stiffer 2D surfaces form adhesive structures at the cell periphery that likely mimic those found in wound healing and fibrotic diseases. The cytoplasmic components of focal complexes and focal adhesions include scaffolding molecules, GTPases, and enzymes such as kinases, phosphatases, and various proteases (Figs. 1.1 and 1.2). Focal complexes (< 1-2 μm in length) form after clustering of engaged integrin receptors and are highly tyrosine phosphorylated structures. They are formed immediately behind a 1-2 μm wide area at the front of the lamellipodium, where active actin polymerization also takes place (Zaidel-Bar, Ballestrem et al. 2003). The recruitment of proteins into focal complexes appears to follow a defined sequence, with the earliest being α-actinin (see below), paxillin, integrins ($\alpha_v\beta_3$), talin, then vinculin and FAK (Laukaitis, Webb et al. 2001).

Early membrane protrusion and focal adhesion formation are controlled by small GTPases, such as Rac. Activation of Rac (Rottner, Hall et al. 1999; Ballestrem, Hinz et al. 2001) is believed to induce the recruitment of high-affinity integins to the lamellipodia (Kiosses, Shattil et al. 2001). Talin, which is a substrate for the Ca^{2+}-activated protease calpain, is required for the recruitment of vinculin and paxillin (Giannone, Jiang et al. 2003) and the activation of vinculin (Izard, Evans et al. 2004; Humphries, Wang et al. 2007). Vinculin in turn drives the formation of focal adhesions through its interaction with talin and actin (Chen, Choudhury et al. 2006). Vinculin also provides the main mechanical coupling between integrins and the cytoskeleton (Geiger and Bershadsky

2002; Goldmann and Ingber 2002), binding several proteins: α-actinin and talin to its head, vasodilator-stimulated phosphoprotein (VASP) and Arp2/3 to the neck, and actin and paxillin to the tail (Zamir and Geiger 2001).

Paxillin binds the cell membrane (either at β_1 or α_4 cytoplasmic tail) (Liu, Kiosses et al. 2002) independently of vinculin (Humphries, Wang et al. 2007). FAK, a 120 kDa cytoplasmic non-receptor tyrosine kinase, binds to integrin clusters, talin, paxillin, and p130Cas (Polte and Hanks 1995; Harte, Hildebrand et al. 1996). As a result, both paxillin and p130Cas are heavily phosphorylated by FAK (Tachibana, Urano et al. 1997). Phosphorylation of paxillin creates docking sites for its interaction with Crk (an adapter/oncoprotein), Csk (C-terminal Src kinase), and Src (discussed later) (Schaller and Parsons 1995). Thus, paxillin is both a scaffold and an adapter protein. Paxillin also plays a pivotal role in the regulation of focal adhesion formation and F-actin organization (Nakamura, Yano et al. 2000). FAK will be discussed in greater detail in section 1.9.a.

Only a minority (25%) of focal contacts contain α-actinin, which localizes to stress fibers during later stages of adhesion (Edlund, Lotano et al. 2001), presumably as an actin crosslinker. In support of this, there is evidence that α-actinin serves to strengthen initial focal adhesions and cause their maturation, which may be regulated by its association with paxillin (Laukaitis, Webb et al. 2001) and FAK (von Wichert, Haimovich et al. 2003). These early focal adhesions, also referred to as focal complexes or nascent focal adhesions, contain a small amount of zyxin (which interacts with α-actinin (Drees, Andrews et al. 1999)) and provide the primary exertion points of propulsive forces in the cell (Beningo, Dembo et al. 2001). The association of zyxin is

sufficient to induce the development of cell protrusions (Golsteyn, Beckerle et al. 1997), and its displacement causes retraction of the cell edge and adversely affects cell spreading and migration (Drees, Andrews et al. 1999).

Integrin clustering leads to the maturation of focal contacts into focal adhesions (Figs. 1.2 and 1.3), which are elongated structures typically ~ 2-10 μm in length and ~ 0.5 μm wide (Abercrombie and Dunn 1975). During this process focal complexes gradually accumulate adhesion-associated molecules. This transition requires Rho-A activation (Rottner, Hall et al. 1999), as treatment with Rho kinase (ROCK) inhibitor Y2762 leads to an accumulation of focal complexes with no formation of focal adhesions (Ballestrem, Hinz et al. 2001; Zaidel-Bar, Ballestrem et al. 2003). Rho may be activated by FAK, as FAK activates p190RhoGEF (Zhai, Lin et al. 2003), which in turn activates Rho (Ingber 2003).

Rho-A, a small GTPase, stimulates contractility which generates tension in cells tightly adhered to the substrate, and induces the assembly of stress fibers (Ridley and Hall 1992). The initial engagement of actomyosin driven forces causes the recruitment of zyxin to focal complexes and stabilizes the protrusion (Zaidel-Bar, Ballestrem et al. 2003). In addition to its role in nascent focal adhesions, zyxin likely plays a role in the assembly and integrity of the actin cytoskeleton and in transducing mechanical signals from cellular adhesions to the nucleus. In addition, zyxin recruits VASP for cytoskeletal reinforcement (actin bundling) in response to cyclic stretch (Yoshigi, Hoffman et al. 2005). Zyxin is expressed in greater levels in mechanically active tissues like the lung, bladder, and vasculature and is frequently overexpressed in hepatocellular carcinomas

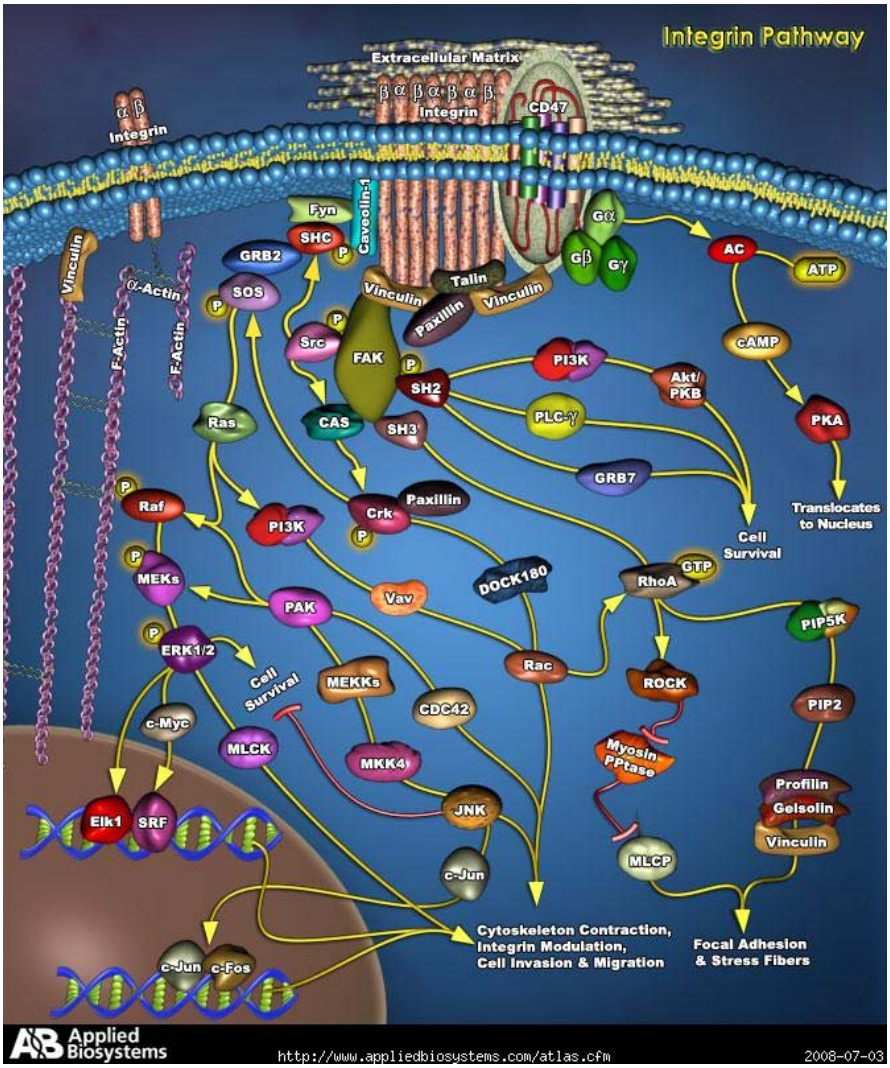

Figure 1.3. Integin mediated signaling pathways

Focal complexes (upper left) "mature" as a result of integrin clustering to form focal adhesions (upper middle), leading to the activation of multiple pathways. Reprinted from: http://www.biocarta.com/pathfiles/h_INTEGRINPATHWAY.asp.

(Sy, Lai et al. 2006). It interacts directly with the stretch sensitive protein, p130Cas (Yi, Kloeker et al. 2002; Tamada, Sheetz et al. 2004) and also shuttles between the cytoplasm and the nucleus (Nix and Beckerle 1997). Although the implications of its nuclear translocation are largely unknown, the process appears to be associated with increased expression of mechanosensitive genes (Cattaruzza, Lattrich et al. 2004). Unlike vinculin, the dissociation rate constant of zyxin at focal adhesions was found to decrease with increasing applied tension (Lele, Pendse et al. 2006.6). Therefore, zyxin is a candidate molecule of mechanotransduction.

Myosin II-based contractility plays a profound role in focal adhesion assembly, growth, and maintenance. It is required for the formation of sustained protrusions (Sandquist, Swenson et al. 2006), the orientation of protrusions in a persistent direction during migration (Honer, Citi et al. 1988; Wessels, Soll et al. 1988; Lo, Buxton et al. 2004), and the organization of F-actin into stress fiber bundles (Sandquist, Swenson et al. 2006). Myosin undergoes cycles of attachment and detachment from the actin filament during contraction. The motor activity of myosin II is stimulated by phosphorylation of its regulatory light chain by myosin light chain kinase (MLCK) (Griffith, Downs et al. 1987) or ROCK, which also inhibits a phosphatase that causes dephosphorylation. Chemical inhibition of myosin II blocks adhesion strengthening (Beningo, Hamao et al. 2006), and fibroblasts lacking myosin IIB (an isoform) are defective in their responses to mechanical stimulations (Lo, Buxton et al. 2004).

The differences between subsets of focal complexes that mature or disassemble, and the intracellular mechanisms responsible for the transition into focal adhesions are

largely unknown. However, recent evidence suggests a mechanism involving active survey of the rigidity of the environment, possibly through periodic retractions at extending lamellipodia (Giannone, Ronde et al. 2004). These retractions occur over a period similar to the traveling time of actin subunits from the front to the back of the lamellipodia, and require actomyosin contractility. This process, combined with the formation of focal complexes at the leading edge, may be analogous to a fisherman who repeats the process of casting and slowly reeling in his bait-laden hook until resistance is detected, signaling the action to tug harder on the line and more quickly reel in his line.

The disassembly of focal adhesions may also be facilitated by microtubules. Dynamic microtubes are locally stabilized during many morphogenic events, such as migration (Bulinski and Gundersen 1991; Gundersen and Cook 1999), and may be required for polarization (Rhee, Jiang et al. 2007). Stable microtubules contribute to cell polarity during migration by serving as tracks for motors, membrane transport, and intermediate filaments (Kreitzer, Liao et al. 1999; Lin, Gundersen et al. 2002). Focal adhesions may direct signaling through a Rho-mediated pathway to stabilize microtubles at the leading edge (Palazzo, Eng et al. 2004), which appears to stimulate their dissociation from the substrate (Kaverina, Krylyshkina et al. 1999). This response is dependent on both active Rho and FAK (Ezratty, Partridge et al. 2005), as microtubule stabilization cannot be stimulated by activated Rho without FAK activity (Palazzo, Eng et al. 2004).

Relaxation of actomyosin contractility causes rapid release of zyxin and VASP from focal adhesions, yet it does not signal the release of vinculin (Lele, Pendse et al.

2006), which likely acts as a key regulatory protein in the turnover of focal adhesions (Humphries, Wang et al.). Fluorescently labeled vinculin is often used as a marker for focal adhesions, as it is present in the focal adhesion from cradle to grave; the size and vinculin content of focal adhesions are proportional to the local force applied to them (Balaban, Schwarz et al. 2001); and its unbinding kinetics remain stable regardless of force (Lele, Pendse et al. 2006).

Although linked to the actin cytoskeleton, mature focal adhesions themselves likely act more as stable anchors that binds the cell to the ECM, as the cell no longer exerts as strong forces through them (Beningo, Dembo et al. 2001). Bundling of actin filaments and aggregation of integrins activate FAK and lead to assembly of multi-component signaling complexes. (Burridge and Chrzanowska-Wodnicka 1996) Signaling from these complexes (outside-in signaling) then initiate changes in morphology through remodeling of the actin cytoskeletal and focal adhesion dynamics (inside-out signaling).

1.8. Techniques to elucidate cell response(s) to mechanical cues

Many cytosolic proteins are recruited to adhesive complexes for scaffolding and signaling, but how and when they are recruited is still largely unknown. The use of biochemical assays, knockout cell lines, and various inhibitors has created much understanding regarding signaling. However, with the complex spatial and temporal arrangements of focal adhesions, more sophisticated techniques are needed to better understand the mechanisms of mechanotransduction.

In order to explore the mechanisms of mechanotransduction through focal adhesions, different methods (Reviewed by Huang, et al, 2004) have been developed to alter the mechanical state within the cell through the application of externally or internally generated forces, either to groups of cells or individually (Reviewed in (Brown 2000; Huang, Kamm et al. 2004). Typical measurements in these studies include dynamics of adhesion structures (Wang, Butler et al. 1993; Katz, Zamir et al. 2000; Zamir, Katz et al. 2000; Galbraith, Yamada et al. 2002), stiffness of the cytoskeleton (Wang, Butler et al. 1993), traction forces exerted by cells (Galbraith and Sheetz 1997; Balaban, Schwarz et al. 2001; Munevar, Wang et al. 2001; Galbraith, Yamada et al. 2002; Tan, Tien et al. 2003), biochemical analysis of adhesion complex proteins (Chen, Kinch et al. 1994; Ren, Kiosses et al. 2000), as well as gross cell behavior (e.g. migration and proliferation) (Chen, Mrksich et al. 1997; Dike, Chen et al. 1999; Lo, Wang et al. 2000; Wang, Dembo et al. 2000; Nelson and Chen 2003; Guo, Frey et al. 2006; Guo and Wang 2007). Studies performed on groups of cells are more amenable to biochemical analysis and may be developed to mimic native physiological conditions of stress, such as fluid shear, mechanical stretch, and hydrostatic pressure that are commonly found *in vivo*. However, there are several advantages of studying individual cells: variability of the data can be preserved while obtaining the mean response; some techniques allow stresses to be focused on a specific region of the cell; and the experimental systems are less likely to be confounded with other possible stimuli.

1.8.a. Fluid shear stress, membrane stretch, and other forms of mechanical stimulation to groups of cells

Fluid shear stress is most often applied to a monolayer of endothelial cells to mimic typical lumen environments in blood vessels. Shear is applied either in a pressure driven flow chamber or a cone-and-plate flow chamber, each capable of generating different flow profiles. The use of transient flows can also generate a time-varying shear stress. The magnitude of shear stress typically ranges from 0.1-2 Pa for studying the proliferation (White, Haidekker et al. 2001), morphology (Ookawa, Sato et al. 1993; Zhao, Suciu et al. 1995), and alignment (Yoshigi, Hoffman et al. 2005) of endothelial cells (Huang, Kamm et al. 2004).

The effect of various types of strain can be determined with cells adhered to an elastic membrane substrate via different adhesive proteins conjugated to the surface. A fixed strain, typically >1% to <30% at rates of 0.1 to 10 Hz, is applied in either one or two dimensions, with either different or equivalent strains along the two directions. For equivalent strains in the two directions, a more uniform, "biaxial" strain field is typically imposed on the cells, although this also imposes a fluid shear stress that can be complex and difficult to predict.

To mimic hypertension, elevated hydrostatic pressure can be imposed on cells in several ways, such as compressed air or a column of fluid above cells, or transmembrane pressure applied through a porous membrane to generate an elevated pressure on the apical surface relative to the region beneath.

1.8.b. Force applied to single cells using optical and magnetic trapping

Precise forces can be applied to a specific receptor(s) through the use of ligand- or antibody-coated particles, typically 0.1 to 10 μm in diameter. Either fixed displacement (optical trapping) or fixed force (magnetic trapping) can be applied to the cell either locally (using few beads) or globally (many beads). The forces can be applied either steadily or dynamically. However, disadvantages of this system are numerous, including internalization of the particles by phagocytosis, non-uniform distribution of the beads across the cell surface, and non-uniformities of the coatings (Huang, Kamm et al. 2004).

Optical traps, also called optical tweezers or laser traps, control the position of one bead at a time through use of a laser (Pool 1988; Huang, Kamm et al. 2004). The force necessary to move the bead is generated by the difference in photon density from the center to the edge of the laser beam, combined with the refraction of the laser by the bead. The trapping force decreases with decreasing object volume, so very small objects do not trap well. Although optical traps are used typically for controlling the position, the applied force can be determined given high spatial resolution of the particle position. Optical traps generate forces on the order of tens to hundreds of piconewtons, suitable for probing local responses in various cell types, membrane and cell elasticity, as well as movements at the molecular scale.

Magnets can also be used to apply either linear forces (magnetic force) or twisting torques (magnetic twisting) to ligand-coated beads (Glogauer and Ferrier 1998; Bausch, Hellerer et al. 2001; Hu, Chen et al. 2003). A constant force can be applied, with the force dependent on the magnetic composition of the beads. Disadvantages of this system

are that many beads are simultaneously affected and the forces on each bead are not necessarily the same due to both variations in particle size and composition as well as non-uniformities of the field. Beads are also susceptible to magnetization with repeated use; paramagnetic beads are less susceptible but are limited to smaller forces. Forces of hundreds of piconewtons per bead can be generated (Huang, Kamm et al. 2004). In the case of magnetic twisting, the magnetic field is briefly pulsed to magnetize the bead with a specific orientation. The rotational force is then produced when a second field is generated in a different direction at a much higher magnitude.

1.8.c. Micropipette aspiration

Originally applied to nonadherent cells for measurement of viscous and elastic properties (Hochmuth 2000), micropipette aspiration has also been used to determine the peeling, or adhesion force of adherent cells (Engler, Griffin et al. 2004) and to look at cytoskeletal rearrangement as a result of applied force (Maniotis, Chen et al. 1997). A sub-atmospheric pressure is used to partially aspirate a cell, causing deformation of the cell membrane as a function of pressure differential across the micropipette.

1.8.d. Flexible substrata and traction force microscopy

Forces exerted by cells on their substrates were first estimated by Harris and coworkers from wrinkles on flexible silicone substrates (Harris, Wild et al. 1980), which provided the motivation to develop improved quantitative techniques of force measurement. The stiffness of most connective tissue cells range from as low as 1 kPa for fibroblasts to ~40 kPa for muscle (Janmey and McCulloch 2007), yet cells are

typically studied on plastic or glass materials with elastic moduli several orders of magnitude higher (GPa). Polyacrylamide gels developed by Pelham and Wang were among the first to allow detailed investigations into the role of substrate stiffness on cell behavior (Wang and Pelham Jr. 1998). These substrates may be created with a range of stiffness, by polymerizing varied amounts of acrylamide and the crosslinker, bis-acrylamide, atop activated glass coverslips (Alpin and Hughes 1981; Wang and Pelham Jr. 1998). Proteins, such as collagen and FN, are then conjugated to the otherwise inert surfaces of these thin, transparent gels in order to induce cell attachment and spreading (Wang and Pelham Jr. 1998; Beningo, Lo et al. 2002). Many other polymer materials and conjugation techniques have since been developed for the same purpose (Wong, Leach et al. 2004; Georges and Janmey 2005). Traction force microscopy is a technique that combines polyacrylamide substrates and the use of embedded beads whose displacement can be recorded during migration to determine the forces exerted by cells (Dembo and Wang 1999).

Several other techniques can be used in combination with these experimental systems. A microneedle can be used to push or pull flexible substrates near the cell to decrease or increase the effective tension applied to cells (Lo, Wang et al. 2000). However, stretching the substrate in this manner may also distort the cell (Wong, Leach et al. 2004).

1.8.e. Atomic force microscopy

To properly compare different studies on cellular responses to substrate stiffness, it is necessary to obtain accurate measurements of the mechanical properties of these substrates. Tensile-like testing was initially performed on these substrates (Wang and Pelham Jr. 1998), but these macro-scale measurements made on bulk samples are thought to be less relevant to the micro-scale properties that are likely sensed by cells on the thinner, hydrated samples. Initial indentation measurements were then performed using small microspheres (Lo, Wang et al. 2000). However, this method relies upon gravity for the force of indentation; this limits indentation and there is inherently high error with indentation methods at lower indentations.

Atomic force microscopy (AFM) has since become the standard means of measuring the mechanical properties of flexible substrates (Domke and Radmacher 1998; Dimitriadis, Horkay et al. 2002; Engler, Bacakova et al. 2004; Engler, Richert et al. 2004; Richert, Engler et al. 2004; Guo, Frey et al. 2006), as well as excised tissues (Engler, Richert et al. 2004; Engler, Griffin et al. 2004; Goffin, Pittet et al. 2006) and individual cells (Radmacher, Fritz et al. 1996; Rotsch, Jacobson et al. 1999; Collinsworth, Zhang et al. 2002; Engler, Griffin et al. 2004; Mahaffy, Park et al. 2004; Shoelson, Dimitriadis et al. 2004). Force-indentation measurements from induced deformation with a calibrated micro- or nano-probe are fit to theoretical models of contact to estimate the stiffness of the material (discussed in detail in Chapter 3). The method is well suited for the range of stiffness typically used in cell culture experiments (~1 kPa – 100 kPa), aside from the very soft substrates for neuronal cells (Flanagan, Ju et al. 2002).

Additionally, force-indentation data can be combined with the original purpose of the AFM, imaging, to obtain a stiffness map of the cell, providing additional information about cell architecture (Rotsch, Jacobson et al. 1999; Mahaffy, Park et al. 2004). A main advantage to using AFM is that location of the indentation can be chosen, allowing for mapping various areas of the cell. Although discrepancies exist between the values obtained using the different AFM devices and methods of data analysis (described later in Chapter 3), there is agreement that qualitative differences in stiffness can differentially affect cell behavior (Engler, Bacakova et al. 2004; Georges and Janmey 2005; Yeung, Georges et al. 2005; Guo, Frey et al. 2006).

In more recent years, AFM has become one of the most rapidly developed imaging techniques for materials, with a number of applications focused on cells, membranes, and single molecules (Reviewed by (Shahin and Barrera 2008)). AFM can be used in combination with other advanced imaging techniques, such as total internal reflectance fluorescence, fluorescence resonance energy transfer (FRET), confocal microscopy, and spectroscopic probes for cellular signals such as Ca^{2+}, to study forces more effectively at single-cell and subcellular levels (Hill, Sun et al. 2007). AFM has been used to apply localized forces to cells (Sun, Martinez-Lemus et al. 2008), to reveal sub-membranous structures (Braet, de Zanger et al. 2001), to measure drug-induced changes in the cytoskeleton (Rotsch and Radmacher 2000), to determine the strength of single receptor-ligand bonds (Hill, Sun et al. 2007), and to look at the forces required for protein unfolding (Rief, Gautel et al. 1997; Rief, Gautel et al. 2000).

1.8.f. Physical constraint of cells by micropatterning

Cells *in vivo* exist within a complex 3D architecture that includes contacts with other cells and with the ECM. Not only do these components have unique mechanical properties, their spatial arrangement also creates a physical constraint for cell migration. The spatial arrangement of ligand binding sites and other characteristic nano-features (e.g. collagen fibrils with 66-nm repeat bands) presents the cell with a complex array of additional spatial inputs that likely account for the striking differences between cells on 2D surfaces and in 3D matrices (spread and bipolar versus elongated and dendritic). Consistent with this notion, fibroblasts become elongated and show few large stress fibers when both dorsal and ventral surfaces are anchored (Beningo, Dembo et al. 2004).

The earliest study that described the effect of topography on cell behavior was reported by Weiss, who described cell alignment along grooves as "contact guidance" (Weiss 1941; Weiss 1945). Although this was first suggested well over 60 years ago, systematic studies into the responses to topographical features have only recently received significant attention in the new era of improved design of implantable materials.

In an effort to simulate the 3D *in vivo* environment, topographical features, such as grooves and channels (Weiss 1941; Weiss 1945; Clark, Connolly et al. 1990; Chesmel, Clark et al. 1995; den Braber, de Ruijter et al. 1998; van Kooten and von Recum 1999; Uttayarat, Toworfe et al. 2005; Justesen, Lorentzen et al. 2008), pillars/posts (Turner, Dowell et al. 2000; Dowell-Mesfin, Abdul-Karim et al. 2004; Dalby, Riehle et al. 2005; Justesen, Lorentzen et al. 2008), pits/cavities (Curtis, Casey et al. 2001; Berry, Campbell et al. 2004; Martines, McGhee et al. 2004; Zinger, Anselme et al. 2004), fibers (Lee, Shin

et al. 2005; Schindler, Ahmed et al. 2005) and microtextured surfaces (Meyle, Gultig et al. 1995) made from a variety of materials have been created by various processing techniques. Adhesive "islands" of specified shape, size, and position can also be created with various micropatterning techniques (Singhvi, Kumar et al. 1994; Chen, Mrksich et al. 1997; Dalby, Yarwood et al. 2002), such as contact printing (Curtis and Wilkinson 2001) or photolithography (Fan, Lu et al. 2000), for investigating the effect of specific geometrical constraints on cellular behavior. A potential caveat to some of these structures and/or techniques is that the features may cause varied protein absorption across the surfaces. Furthermore, high resolution imaging of molecules may be impossible due to the interference to optics by the material or surface features, while other microfabrication methods require costly equipment and clean rooms.

Advances in microfabrication techniques have led to the capability to create, in a simple and cost effective manner, surfaces with well-defined topographical features that are amenable to high-resolution imaging. One such method uses an electric field applied to a thin polymer film (electrohydrodynamic instability) to create a field of pillars (Tsai, Crosby et al. 2007). A polymer film is spin coated onto a conducting or semiconducting surface then placed in an electric field. The air gap over the polymer film contributes to a small gradient in the dielectric constant at the surface; this creates electrostatic pressure to pull the polymer film toward the electrode above it. This ultimately leads to the formation of pillars on the surface of the film (results on substrates made with this technique are described in Chapter 2).

1.8.g. Chemical disruption of internally generated tension

To investigate intracellular tension that responds to substrate rigidity (Solon, Levental et al. 2007), various drugs have been used to inhibit molecules involved in cytoskeletal contractility. The effects of inhibition on focal adhesion formation, maintenance, and/or remodeling can then be surveyed. Blebbistatin (1-phenyl-1,2,3,4-tetrahydro-4-hydroxy-pyrrolo[2,3,b]-7-methylquinolin-4-one) is a cell-permeant and selective inhibitor of myosin II ATPase (Straight, Cheung et al. 2003), making it a valuable tool to study the function(s) of myosin II-dependent forces in cell movement. Blebbistatin inhibits myosin II from moving actin filaments (Sakamoto, Limouze et al. 2005) by binding it in an actin-detached state (Kovacs, Toth et al. 2004). Actin and microtubules are often disrupted using cytochalasin D and nocodazole, respectively. Contractility can also be disrupted using a variety of inhibitors, including those against tyrosine phosphatases, such as phenylarsine oxide (Pelham and Wang 1997); tyrosine kinases, such as PP2 and genistein (Bershadsky, Chausovsky et al. 1996; Damianova, Stefanova et al. 2008); and Rho or ROCK (Wozniak and Keely 2005), such as Y-27632.

1.9. Cellular responses to mechanical cues

The early work using optical tweezers and magnetic bead cytometry showed that integrin-mediated adhesions between the cytoskeleton and the ECM are reinforced upon the application of force (Choquet, Felsenfeld et al. 1997). Both the size of focal adhesions (Bershadsky, Balaban et al. 2003) and the stiffness of the cytoskeleton increase in proportion to applied forces (Wang, Butler et al. 1993; Wang and Ingber 1994). Focal

adhesions could even be stimulated to grow in relaxed cells through forces applied through ECM-coated beads using laser tweezers (Riveline, Zamir et al. 2001; Galbraith, Yamada et al. 2002). Furthermore, mechanically sensitive genes are activated after twisting integrin receptors using magnetic forces (Chen, Fabry et al. 2001). However, in addition to various technical complications, forces from these methods could also strain the cell, activating stretch sensitive channels and/or induce other conformation changes that can complicate the effects on focal adhesion dynamics.

External forces can effectively be substituted with external resistance imposed by the rigidity of substrates; parallel comparisons of cells on substrates of different rigidity (stiff versus soft) can be made without the complicated effects of straining the cell externally. On increasingly stiffer substrates, 3T3 fibroblasts were initially shown to spread and proliferate more (Pelham and Wang 1997; Wang, Dembo et al. 2000) and apoptose less (Wang, Dembo et al. 2000), yet the stiffness of the substrate had no such effects on transformed cells (Wang, Dembo et al. 2000). Similar to the response to applied forces, increasingly stiffer substrates (or matrices) also cause cells to adhere more strongly (Engler, Griffin et al. 2004; Guo, Frey et al. 2006),

Substrate stiffness is likely probed by cells in part through traction forces on the nanoNewton-scale (Choquet, Felsenfeld et al. 1997). Measurements of traction forces show that cells pull harder on stiffer surfaces (Munevar, Wang et al. 2001), consistent with an increase in adhesion. Moreover, cells plated on pillars of different rigidities exert forces proportional to the spring constant, to generate similar deformations (~130+/- 20 nm) regardless of the rigidity of the pillars (Saez, Buguin et al. 2005).

When cells are plated on rigid surfaces or dense ECM, contractile forces cause the tension to build up without deforming or contracting the matrix (Wozniak, Desai et al. 2003). Therefore, the less deformable (stiffer) the substrate is, the more tension is generated within the cell (Solon, Levental et al. 2007). This is marked by an increasing amount of F-actin at the site of adhesion (cytoskeletal "reinforcement"). Indeed, fibroblasts on softer materials adopt a more spherical morphology with more diffuse F-actin (Georges and Janmey 2005), whereas they become more elongated with increased levels of F-actin on stiffer surfaces (Yeung, Georges et al. 2005). Remodeling of the actin cytoskeleton, which in some cases was reversible after removal of the stimuli, was also seen in chondrocytes exposed to static and cyclic compressive strain and hydrostatic pressure (Knight, Toyoda et al. 2005).

Traction forces are abolished by disrupting the actin cytoskeleton with cytochalasin D (Pelham and Wang 1999), further demonstrating the involvement of cytoskeletal structures. Myosin-II contractility is also required in the rigidity response, as blebbistatin induces rapid disassembly of focal adhesions (Geiger and Bershadsky 2001). Conversely, cells treated with a tyrosine phosphatase inhibitor, phenylarsine oxide, overcome the less spread phenotype on soft gels and regain focal adhesions (Pelham and Wang 1997). Microtubules likely do not contribute directly to traction forces, as administration of nocodazole, a microtubule destabilizer, had no immediate effect (Pelham and Wang 1999).

Substrate stiffness also affects cell migration, as speed was found to inversely correlate with substrata stiffness (Pelham and Wang 1997), likely related to enhanced

adhesion (Ghosh, Pan et al. 2007) as a result of increased integrin expression (Delcommenne and Streuli 1995, Flanagan, 2002 #112; Engler, Bacakova et al. 2004; Richert, Engler et al. 2004; Yeung, Georges et al. 2005) and/or affinity. Cells also migrate preferentially toward stiffer regions (Pelham and Wang 1997; Lo, Wang et al. 2000; Gray, Tien et al. 2003), a response termed "durotaxis".

Sensitivity to substrate stiffness has since been shown for various cell types, including fibroblasts, endothelial cells, myocytes, hepatocytes, and neurons (Georges and Janmey 2005). Cell proliferation and differentiation were also found to correlate directly with the number of adhesive bonds (measured by FRET) between preosteoblasts and myoblasts and an artificial ECM (Kong, Boontheekul et al. 2006). Differentiation appears to be affected by an optimum stiffness (Kong, Boontheekul et al. 2006) that matches that of the native tissue (Engler, Griffin et al. 2004; Engler, Sweeney et al. 2007).

Cells are also sensitive to the geometry of adhesions, as they switch from growth to apoptosis and show altered protein secretion (Singhvi, Kumar et al. 1994) when spreading is limited by decreasing the size of ECM coated adhesive islands (Chen, Mrksich et al. 1998). Cells adhered to fibers synthesize more collagen (Lee, Shin et al. 2005) and display a more *in vivo* like morphology (Lee, Shin et al. 2005, Schindler, 2005 #475) compared to those spread on the same materials in 2D.

Similar effects of contact guidance of many different cell types have been observed on various topographical features. Grooves, pillars and fibers have caused alignment of fibroblasts, endothelial cells, epithelial cells, neurons, and macrophages

(Weiss 1941; Weiss 1945; Clark, Connolly et al. 1990; Chesmel, Clark et al. 1995; Meyle, Gultig et al. 1995; Chen, Mrksich et al. 1997; den Braber, de Ruijter et al. 1998; van Kooten and von Recum 1999; Uttayarat, Toworfe et al. 2005). Cell behavior has been investigated extensively along grooves and ridges (Weiss 1941; Weiss 1945; Clark, Connolly et al. 1990; Chesmel, Clark et al. 1995; den Braber, de Ruijter et al. 1998; van Kooten and von Recum 1999; Uttayarat, Toworfe et al. 2005; Justesen, Lorentzen et al. 2008); both cause cells to elongate and to move at an increased speed (Wojciak-Stothard, Madeja et al. 1995; Justesen, Lorentzen et al. 2008). Cell alignment along these features appears to be affected by a complex set of parameters. For example, one study found that, depending on the groove depth, fibroblasts become highly elongated and crawl either inside or along the edge of grooves (Walboomers, Monaghan et al. 1999). While ridge width may be more effective than the groove width to induce alignment (den Braber, de Ruijter et al. 1998), depth appears to be a more important parameter (Clark, Connolly et al. 1987; Wojciak-Stothard, Madeja et al. 1995; Walboomers, Monaghan et al. 1999). Macrophages also become highly elongated, adherent, and persistent, with increased levels of F-actin when spread on shallow grooves (5 μm in depth) (Wojciak-Stothard, Madeja et al. 1995). In the case of deeper grooves, cells were aligned along the ridge, yet lost contact with the bottom of the grooves (Walboomers, Monaghan et al. 1999). Adhesion was concentrated at the groove-ridge transition, as reported in this and another study (Curtis, Casey et al. 2001).

Pillars elicit varied cell responses depending on their size and spacing, though the results are somewhat conflicting. There is very weak adhesion to nanopillars in one

instance (Curtis, Casey et al. 2001), yet upregulation of the expression of Rho, MMPs, and minor ECM constituents in another study (Dalby, Yarwood et al. 2002), suggesting increased adhesion. Changes in cell spreading on pillars may depend on the distance between the pillars (Justesen, Lorentzen et al. 2008), which correlated with changes in gene expression of actin and Rac (Dalby, Riehle et al. 2005). Scanning electron microscopy of cells on pillar arrays with an interpillar gap of 5.0 μm further demonstrated that cells made contact with the tops of the pillars but failed to reach down into the spaces between them (Turner, Dowell et al. 2000). However, the distribution of actin and vinculin were highly polarized on the top surface (Turner, Dowell et al. 2000).

There is less, and in some cases a lack of cell adhesion to nanopits than to flat surfaces (Curtis, Casey et al. 2001; Martines, McGhee et al. 2004). Cells are actually oblivious to 10 μm cavities and pits, yet take on the characteristic 3D shape in 30 μm pits (Zinger, Anselme et al. 2004). The differences in size may have differential effects on membrane curvature, thus sensing of the discontinuity or ridge (Clark, Connolly et al. 1987; Clark, Connolly et al. 1990).

Although collectively these studies highlight the phenomenon associated with cellular responses to topography, there is limited knowledge of how cells actually detect and respond to topographic features. Even more perplexing are the differences in behavior for cells on pillars versus pits. A potential explanation for this was proposed by Vogel and coworkers, who suggested that concave and convex membrane curvatures may be sensed by two different mechanisms (Vogel and Sheetz 2006). Cells would interact with grooves or pits through convex curvatures of the membrane, and with fibers, posts,

or pillars through concave curvatures (Vogel and Sheetz 2006). A concave membrane curvature may be recognized by BAR-domain (Bin, amphiphysin, Rvs domain) proteins (Habermann 2004; Zimmerberg and McLaughlin 2004), which can recruit small G-proteins. One member of the BAR-domain family of proteins is linked to the activation of Rac and WAVE (the Wiskott-Aldrich syndrome protein (WASP)-related protein) in regulating membrane ruffling (Miki, Yamaguchi et al. 2000). Other BAR-domain family proteins are implicated in motility (Vogel and Sheetz 2006). Also relevant is the possibility that discontinuities in topographical features may affect the spacing of molecular recognition sites. Regions with more concentrated adhesions may server as the primary sites for propelling cell migration.

Furthermore, differences in cortical stiffness, and thus the concavity of the membrane, between different cell types could account for the discrepancies in the effects of certain topographical features on different types of cells. The actin cell cortex of certain cells may be too stiff to reach into deep, narrow grooves or pillars with limited spacing, as suggested by Walboomers and coworkers (Walboomers, Monaghan et al. 1999). Thus, a balance of spacing, depth, and size may be critical for the responses to topographical features. These parameters, as well as the material of the surface, should be taken into account when designing experiments related to topographical responses.

1.10. Potential mechanism(s) of rigidity-based mechanotransduction

A possible mechanism for force and/or geometry sensing involves conformational changes in specific molecules upon internal or external force application (Tang, Mehta et

al. 1999; Bershadsky, Balaban et al. 2003), such that the relevant parameter may be deformation rather than forces per se. Focal adhesions form when a cell can exert large stresses against the ECM, with an increased size on substrates of increasing stiffness (Pelham and Wang 1997). The rigidity of the substrate provides resistance to force-induced displacements, thus conformational changes of signaling proteins may be regulated in a displacement-dependent manner. In fact, there appears to be a linear dependence of focal adhesion size in proportion to the forces transmitted through them (Bershadsky, Balaban et al. 2003). The typical stress, roughly 5.5 kPa, leads to a conservative estimate of a few piconewtons of forces for each integrin dimer (Huang, Kamm et al. 2004).

Protein molecules consist of a diverse set of structural motifs that change the topographic relationship (conformation) in response to mechanical forces (Kellermayer, Smith et al. 1997; Rief, Gautel et al. 1997). The force required to produce a conformational change around the FN-integrin bond is estimated to be in the range of 30-100 pN (Lehenkari and Horton 1999), whereas forces as low as 3-5 pN can unfold certain subdomains of FN (Erickson 1994). Consistent with the notion that active cellular contractions can induce signaling, the magnitude of forces that can be produced by a single myosin II molecule falls in a range that exceeds thermal fluctuations (3-4 pN) (Finer, Simmons et al. 1994).

Geometrical or topographical features may affect the density of adhesions and associated signals relative to the cell volume (Beningo, Dembo et al. 2004). The effects may be similar to that of compressive stress, which alters signaling by epidermal growth

factor (EGF) receptors by decreasing the space between receptors and enabling greater occupancy (Chu, Foley et al. 2005). Enhanced signaling is also noted at the corners of cells compared to other areas when plated on micropatterned squares (Guo and Wang 2007).

Due to the sheer number and diversity of proteins within the focal adhesion, it has been difficult to identify the precise pathway(s) for the transmission of force (Fig. 1). Within these structures, a number of signaling molecules have been found to be mechanosensitive, including Src, Rho, Rac, paxillin, members of the zyxin family, and FAK (Reviewed by (Ingber 2003).

1.10.a. Focal adhesion kinase (FAK)

FAK modulates various intracellular signaling pathways through associations with both activators and inhibitors of various small GTPases (Rho, Rac, cdc42, and Ras) (Mitra, Hanson et al. 2005). FAK complexes are responsible for downstream signaling pathways in the cytoplasm that regulate various cell functions including motility, growth, adhesion, proliferation, and apoptosis. Cells on/in increasingly rigid substrates exhibit increased integrin clustering, FAK phosphorylation, and proliferation. Overexpression of FAK has been linked to increased migration and growth, leading to tumor formation and cancer progression (Weiner, Liu et al. 1994; Owens, Xu et al. 1995; Tremblay, Hauck et al. 1996; Cance, Harris et al. 2000; Rovin, Frierson et al. 2002). Conversely, Y397FAK levels decrease (Ilic, Genbacev et al. 2001) in situations where invasive potential is compromised (e.g. preeclampsia *in vivo*).

Responses to FAK phosphorylation include organization of a fibrillar FN matrix (Ilic, Kovacic et al. 2004), stabilization of microtubules at the leading edge (Palazzo, Eng et al. 2004), spreading of cells, formation of focal adhesions, remodeling of the cytoskeleton, and changes in gene expression (Mansour, de Tombe et al. 2004). Therefore, FAK and pY397-FAK are likely key regulators in outside-in signaling.

Mouse embryos lacking FAK (FAK -/-) die at embryonic day 8.5 (George, Georges-Labouesse et al.), and FAK -/- fibroblasts have altered spreading (Ilic, Furuta et al. 1995), decreased random migration (Ilic, Furuta et al. 1995), and a deficient mechanosensing ability (Wang, Dembo et al. 2001). FAK -/- cells spread poorly on rigid FN matrices, yet inhibition of Rho-kinase in these cells restores normal spreading (Chen, Tzen et al. 2002). Focal adhesion formation is not impaired in FAK -/- cells, as they actually have larger, more stable focal adhesions (Ilic, Furuta et al. 1995). However, the turnover of focal adhesions appears to be inhibited in FAK -/- cells, resulting in slower detachment and altered motility (Ilic, Furuta et al. 1995). This could be due to the lack of Rho inhibition in FAK-/- cells, as Rho activity inversely correlates with focal adhesion turnover (Ren, Kiosses et al. 2000). The increased stability of focal adhesions in these cells may also be attributed to a loss of calpain, which cleaves several focal adhesion proteins and is targeted to focal adhesions through an interaction with FAK. Large, stable focal adhesions with reduced turnover of zyxin and vinculin are also seen after inhibition of calpain (Bhatt, Kaverina et al. 2002). FAK also plays a role in cell death mediated by loss of adhesion (Crouch, Fincham et al. 1996; Frisch, Vuori et al. 1996; Hungerford, Compton et al. 1996), as reduced FAK phosphorylation leads to a decrease

in focal adhesion formation and apoptosis (Carlson, Longaker et al. 2004; Xia, Nho et al.).

FAK appears to be the earliest marker in response to tension (Chen, Tan et al. 2004). FAK is phosphorylated more extensively on rigid substrates (Schlunck, Han et al. 2008) and upon application of mechanical strain in smooth muscle and endothelial cells (Yano, Geibel et al. 1996; Tang, Mehta et al. 1999). Thus, deficiencies in FAK -/- fibroblasts are likely caused by a lack of binding to other signaling molecules to elicit the mechanoresponses.

1.10.b. The SFK/FAK connection

Integrin-ligand binding and cytoskeletal reinforcement of integrins, or clustering, enhances the activation of FAK, particularly through autophosphorylation of its Y397 residue (pY397-FAK) (Kwong, Wozniak et al. 2003; Shi and Boettiger 2003). Tyrosine phosphorylation of FAK allows it to interact with other docking and adaptor proteins (Boudreau and Jones 1999) and is associated with the recruitment of Src and/or Fyn (Parsons 1996). Although binding to Src activates the kinase activity of FAK (Calalb, Polte et al. 1995), FAK likely acts more as a scaffold than a kinase, as kinase dead FAK retains most of its function (Schaller, Hildebrand et al. 1999). Binding of Src creates docking sites for other proteins that link FAK to activation of Ras and the mitogen-activated protein kinase (MAPK) pathway (Schlaepfer, Hanks et al. 1994; Calalb, Zhang et al. 1996; Schlaepfer, Jones et al. 1998) , which transduces proliferative signals.

Src family kinases include Src, Fyn, and Yes. Activation of Src family kinases (SFK), particularly Fyn, is required for the force-dependent formation of focal complexes and strengthening of the integrin-cytoskeleton connection during the initial phases of ECM contact (von Wichert, Jiang et al. 2003). Fyn-/- cells also show defects in focal contact formation during early phases of cell spreading (von Wichert, Jiang et al. 2003). In addition, increased spreading and growth correlate with the recruitment of Fyn to the leading edge (Kostic and Sheetz 2006).

A major substrate of the SFKs is the stretch sensitive docking protein p130Cas (Cary, Han et al. 1998), which is required for the rigidity response and is localized to the leading edge in close proximity to Fyn in a Fyn-dependent manner (Kostic and Sheetz 2006). A potential mechanism for the rigidity response involves force (thus displacement) dependent Fyn phosphorylation of p130Cas (Kostic and Sheetz 2006). Cytoskeletal stretch stimulates SFK-mediated phosphorylation of p130Cas (Tamada, Sheetz et al. 2004), likely induced by conformational changes in p130Cas and possibly other proteins such as FAK (Sawada and Sheetz 2002). P130Cas can simultaneously bind Src and FAK, facilitating Src activation of FAK (Fonseca, Shin et al. 2004). FAK and Src binding causes the exclusion of FAK from focal adhesions (Katz, Romer et al. 2003). Activated Src causes decreases of focal adhesion components and cell adhesion itself, leading to the turnover of focal adhesions and increased migration.

Receptor-like protein tyrosine phosphatase alpha (RPTPα) (von Wichert, Jiang et al. 2003) likely plays a role in mediating this matrix rigidity-based signal transduction. RPTPα and $\alpha_v\beta_3$ integrin are proposed to form a rigidity-responsive complex at the

leading edge on FN (Kostic and Sheetz 2006). RPTPα knockout cells spread equally on soft and stiff FN matrices (Jiang, Huang et al. 2006) and show defects in early spreading and focal contact formation (Su, Muranjan et al. 1999). In addition, RPTPα overexpression neoplastically transforms NIH 3T3 cells (Zheng, Resnick et al. 2000). RPTPα not only antagonizes the effects of SFK, but also activates SFK by dephosphorylation of a negative regulatory phosphotyrosine in their c-terminal domains (Zheng, Wang et al. 1992; Ponniah, Wang et al. 1999; Su, Muranjan et al. 1999; Zheng, Resnick et al. 2000; von Wichert, Jiang et al. 2003). However, its roles in mechanosensing may involve both positive and negative effects on tyrosine phosphorylation (Ponniah, Wang et al. 1999).

Together, these results demonstrate that responses to rigidity involve initial activation of SFKs, followed by conformational changes of proteins such as p130Cas that ultimately activate FAK (Cary, Han et al. 1998). These results also suggest that FAK/p130Cas complexes target downstream pathways in mediating FAK-promoted cell migration (Cary, Han et al. 1998).

1.11. Localization of mechanosensitive responses

How cell migration is regulated globally through adhesions is still a subject of heated debate. In the tug-of-war model (Fig. 1.4), migration occurs as a result of opposing forces generated between the leading edge and the cell body, with the region that generates the strongest traction forces determining the polarity (Bray 2001). Conversely, the frontal towing mechanism (Fig. 1.4) proposes a qualitative differentiation

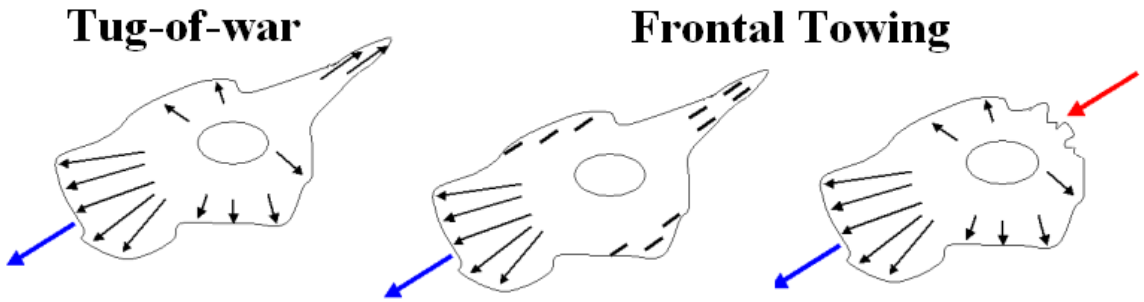

Figure 1.4. Models of cell migration

In the tug-of-war model of migration, all parts of the cell are trying to walk away from each other, with the strongest side determining polarity of migration. In the frontal towing model, traction forces are localized to the cell anterior and the adhesions in the cell posterior serve as passive anchors that are eventually overcome, resulting in random and spontaneous tail retraction.

between the front and rear ends of a migrating cell, with propulsive forces at the leading edge towing a passively anchored cell body to generate forward migration (Munevar, Wang et al. 2001). This mechanism is related to the model of elastic cells, where the forces exerted by the leading edge stretch the cell like a rubber band until they overcome the adhesions at the trailing edge, causing the rear end to spring forward (Chen 1981).

Important information can be gained by studying the distribution and nature of forces relative to cell migration and their effect on cell shape. In an attempt to distinguish between the above models, rear and frontal retractions were induced by releasing an RGD peptide through a microneedle (Munevar, Wang et al. 2001). Rear release results in a slight increase in frontal traction forces, whereas even partial frontal release causes immediate and global decreases in traction stress. These results are consistent with the frontal towing mechanism, where distinct mechanical interactions at the leading edge provide active forces for dragging a passive cell body along the substrate.

1.12. Unanswered questions on mechanosensing

Cell migration is critical during development, tissue homeostasis, wound healing, and cancer metastasis. The process is highly sensitive to the state of the ECM, including chemical, physical, and topographical features found under physiological conditions. These parameters also have profound effects on cellular adhesion and shape, yet little is known about how cells translate these external signals into intracellular signals. Although a number of the molecular components involved in these responses have been

identified, many more likely remain unknown. Equally important is their spatial and temporal dynamics within focal adhesions, at steady state and in response to various signals.

Questions persist regarding how cells regulate their migration through the assembly and disassembly of adhesion structures. Also unresolved is the role of cell morphology in these responses; they show dramatically different shapes in response to substrate rigidity and dimensionality of the ECM. The outcomes of these mechanotransductive responses will have profound impact on improving medical devices, engineered tissues, and biomimetic materials, as well as the therapeutic treatment of various fibroproliferative diseases. Simple, manipulatable experimental systems are essential tools for systematic investigations of these mechanisms.

This thesis involves two experimental systems to determine the effects of substrate topography as well as substrate stiffness on cell migration and morphology. The first experimental system is a substrate with pillar features, for investigating the effect of topography on cell migration and the role of FAK and myosin-II in cellular sensing of topographical features. The second system is a photo-modulatable material that softens upon UV illumination, useful for probing both global and local responses to changes in substrate rigidity.

CHAPTER 2. CELLULAR RESPONSES TO SUBSTRATE TOPOGRAPHY: ROLE OF MYOSIN II AND FOCAL ADHESION KINASE

2.1. Abstract

Although 2D cultures have been used extensively in cell biological research, most cells *in vivo* exist in a 3D environment with complex topographical features, which may account for at least some of the striking differences between cells grown *in vivo* and *in vitro*. To investigate how substrate topography affects cell shape and movement, I plated fibroblasts on chemically identical polystyrene substrates with either flat surfaces or micron-sized pillars. Compared to cells on flat surfaces, NIH 3T3 cells on pillar substrates showed a more branched shape, an increased linear speed of migration, and a decreased directional stability. These responses may be attributed to stabilization of cell adhesion on pillars coupled to myosin II-dependent contractions toward pillars. Moreover, using FAK-/- fibroblasts I found that FAK is essential for the responses to substrate topography. These observations suggest that increased surface contact localized to the topographic features guides cell migration by regulating the strength of focal adhesions and contractions, through a FAK-and myosin II-dependent mechanism.

2.2. Introduction

Cell migration is essential for tissue development and homeostasis, including the responses to wounds and inflammation. While cell migration on 2D surfaces in vitro has been investigated in detail, migration in vivo is known to occur predominantly in a 3D environment with complex physical, chemical, and topographical features. Compared to cells on 2D surfaces, cells in vivo or in model tissues show a drastically different morphology and behavior, including the lack of prominent stress fibers and focal adhesions (Bondy, Wilson et al. 1985; Cukierman, Pankov et al. 2002; Beningo, Dembo et al. 2004).

While most investigations have focused on chemical factors, accumulating evidence indicates that cells can respond to physical parameters such as substrate rigidity and mechanical stress, as well as topographic features such as grooves on the surface. Fibroblast migration may be directed toward increased substrate adhesivity (Carter 1967), stiffness (Lo, Wang et al. 2000), or tension (Lo, Wang et al. 2000). In addition, on substrates inscribed with grooves, fibroblasts become highly elongated and crawl either inside or along the edge of grooves (depending on the depth of the groove; (Walboomers, Monaghan et al. 1999)), as if they were seeking maximal topographical stimulation. This phenomenon has been referred to as contact guidance (Weiss 1941). Recent observations further indicate that the dorsal-ventral asymmetry of substrate adhesion in 2D cultures plays a major role in stimulating cell spreading and stress fiber assembly. When both dorsal and ventral surfaces are anchored on the ECM, fibroblasts become elongated and

show few large stress fibers, similar to what is found in connective tissues (Beningo, Dembo et al. 2004).

Despite the long awareness of contact guidance, there has been only limited knowledge of how cells detect and respond to topographic features. There are strong indications that integrins and focal adhesions play a major role in the responses to non-chemical stimuli. Focal adhesions, associated with the actin cytoskeleton on the cytoplasmic side and the ECM on the extracellular side, are the exertion points of cellular contractile forces on the substrate. The cytoplasmic face of the focal adhesion is also known to carry a complex battery of structural (e.g., vinculin, α-actinin and paxillin) and signaling proteins (e.g. focal adhesion kinase, or FAK, and src) (Geiger and Bershadsky 2001; Geiger, Bershadsky et al. 2001). Although the exact functions of these signaling molecules are unclear, they presumably play the important role of transmitting extracellular physical or topographic signals across the membrane and translating them into intracellular chemical or physical signals. Consistent with this idea, cells in some late-stage tumors show overexpression of FAK (Weiner, Liu et al. 1994; Owens, Xu et al. 1995; Tremblay, Hauck et al. 1996; Cance, Harris et al. 2000; Rovin, Frierson et al. 2002), while FAK-/- and myosin IIB -/- fibroblasts are also defective in their responses to mechanical stimulations (Wang, Dembo et al. 2001; Lo, Buxton et al. 2004).

Although grooved substrates have been used extensively for studying cellular responses to topographic signals (Clark, Connolly et al. 1990; Wojciak-Stothard, Madeja et al. 1995; Walboomers, Monaghan et al. 1999; Curtis, Casey et al. 2001), the exclusive localization of cells within the grooves and the extremely narrow width impede the

investigation into the migration responses and structural organization. I have therefore utilized polystyrene substrates that contain a field of semi-ordered, micron-sized pillars, such that migrating cells continuously encounter alternating flat and bumpy surfaces. Comparison with cells on flat polystyrene surfaces allowed me to determine unambiguously the responses to topographical features. This strategy has provided not only new insights into how normal fibroblasts respond to substrate topography, but also a powerful test for the requirements of specific proteins. The results suggest that substrate topography guides cell migration by enhancing the stability of adhesions at pillars coupled to myosin II-dependent contractions. In addition, FAK is essential for these responses.

2.3. Materials and Methods

2.3.a. Preparation and characterization of substrates

Pillar substrates were prepared by my collaborator Dr. Irene Tsai, Department of Polymer Sciences, University of Massachusetts. Briefly, polymethylmethacrylate was applied to a silicon oxide surface and subjected to a strong electric field (Schaffer, Thurn-Albrecht et al. 2000; Morariu, Voicu et al. 2003). Electrohydrodynamic instabilities caused the surface to form micron-sized pillars. PDMS was then poured over the pillars and cured overnight at 60ºC to serve as the template. The template was then pressed onto a 1 μm thick polystyrene film at 150ºC atop a coverslip and peeled off. This simple approach generated a semi-ordered array of pillars on the central part of the otherwise flat

polystyrene surface (Fig. 2.1). The surfaces were then made hydrophilic by reactive ion etching.

Topographical images of the substrate (Fig. 2.1) were obtained using an Autoprobe M4 atomic force microscope (AFM) (Veeco, Santa Barbara, CA) equipped with ProScan V1.51b software (Veeco). Images were acquired in contact mode with a standard tipped CSC12 cantilever of 0.03 N/m nominal stiffness (Veeco). Dimensions of the pillars were determined from AFM images collected on three different samples. All observations reported here were made in regions with a similar size, density and distribution of the pillars.

Typical pillars were 1.78 ± 0.02 μm in height, 10.30 ± 0.19 μm in diameter, and spaced 15.76 ± 0.26 μm center-to-center (mean ± s.e.m., n = 33 for each). Assuming a regular distribution of pillars on a grid, ~ 46% of the total surface was located on the top and side of pillars, and ~ 54% as flat surfaces between the pillars.

Coverslips carrying the polystyrene substrate were mounted onto 35 mm cell culture dishes (Falcon, Nowhere, NV), with a hole drilled at the center, using UV-cured optical adhesive (Type 71, Norland Products, Cranbury, NJ). Prior to use, culture dishes containing the substrates were sterilized by exposure to UV light inside a cell culture hood for 10 min.

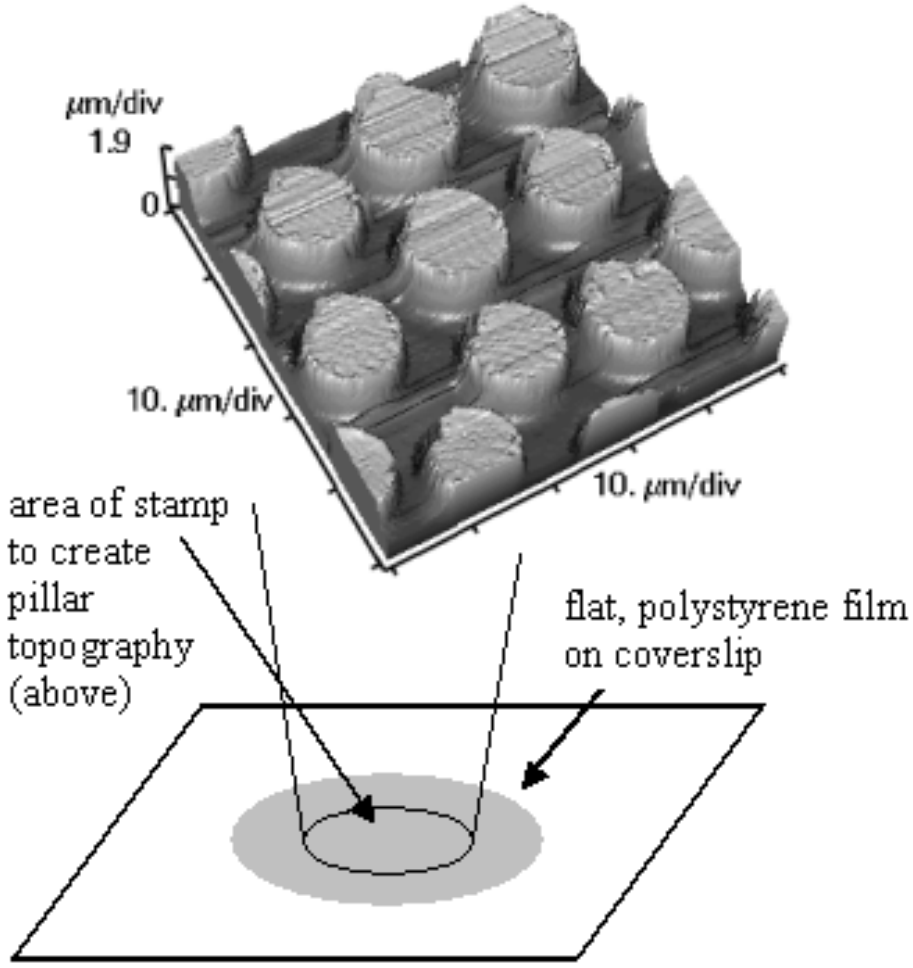

Figure 2.1. Topography of pillar substrate

A semi-ordered array of pillars (top) is created by pressing a PDMS mold with topographical features into an otherwise flat 1 μm thick polystyrene film. Reactive ion etching of the entire surface creates a hydrophobic cell culture substrate with both pillars (central) and flat regions (surrounding, exterior edges). Topographical images of pillar substrates (top) were taken by AFM in contact mode. A 50 μm x 50 μm region is shown as a projected three-dimensional image. Fine features on top of the pillars are likely an imaging artifact.

2.3.b. Cell culture and transfection

All cells were maintained in a standard incubator with 5% CO_2. Experiments were performed within three days of plating. NIH 3T3 fibroblasts were obtained from Dr. Ann Chambers (Bondy, Wilson et al. 1985; Hill, Wilson et al. 1988) and were cultured in Dulbecco's modified Eagle medium (Sigma, St. Louis, MO) containing 10% donor calf serum (Hyclone, Logan, UT) supplemented with 10,000 units/ml penicillin, 10,000 μg/ml streptomycin, and 29.2 mg/ml L-glutamine for up to 20 passages. FAK-/- fibroblasts re-expressing FAK under Tet-off control were obtained from Dr. Steve Hanks (Owen, Ruest et al. 1999). The cells were cultured in Dulbecco's modified Eagle medium (Sigma) containing 10% fetal bovine serum (Atlanta Biologicals, Norcross, GA) supplemented with 10,000 units/ml penicillin, 10,000 μg/ml streptomycin, 29.2 mg/ml L-glutamine, and 1% nonessential amino acids (GIBCO/BRL, Grand Island, NY). Tetracycline (Calbiochem, San Diego, CA) was added during each change of media at a concentration of 1 μg/ml to prevent expression of the FAK protein in FAK -/- experiments. To induce FAK expression, the same FAK -/- cells were transferred to media lacking tetracycline for 36 to 48 hr prior to experiments (Owen, Ruest et al. 1999). To image focal adhesions, cells were transfected with plasmids carrying enhanced green fluorescent protein (EGFP) tagged paxillin (Rottner, Krause et al. 2001), using the Amaxa nucleofector and kit R following the protocol recommended by the manufacturer (Amaxa, Gaithersburg, MD). Cells were plated onto the substrates at a low density to minimize cell-cell contacts.

Blebbistatin (Toronto Research Chemicals Inc., Ontario, Canada), an inhibitor of non-muscle myosin II ATPase (Straight, Cheung et al. 2003; Allingham, Smith et al. 2005), was applied by replacing the culture medium with medium containing 100 μM blebbistatin as described previously (Guha, Zhou et al. 2005). To allow time for the drug to take effect, experiments were performed after 2 hr of incubation. Since blebbistatin is sensitive to blue light (Kolega 2004; Sakamoto, Limouze et al. 2005), a red filter was placed in the transmission illumination light path during image acquisition, and the total period of data acquisition was limited to within 8 hr (after which the effects of the drug appeared to be diminished).

2.3.c. Video microscopy and measurements of cell motility

Cell-plated substrates were loaded into a stage incubator on a Zeiss IM35 microscope equipped with a Neo-Fluar 25x N.A. 0.8 oil phase objective lens (Ziess, Thornwood, NY). Images were acquired with a video rate surveillance CCD camera (Mintron 12V1E-EX, Santa Clara, CA) or with a Roper NTE/CCD-512-EBFT camera (Roper Scientific, Trenton, NJ). Time-lapse images were recorded every 2 to 4 min for a period of at least 2 hr and analyzed with custom software. Cells selected for analysis were spread, motile, separated from neighboring cells, and were neither exiting nor entering mitosis. Additionally, all the quantitative analyses were performed in regions of similar pillar size and density. Coordinates of the nuclear centroid were determined automatically using a pattern recognition algorithm. Since double-reciprocal analysis as applied previously did not generate straight lines for cells on pillar substrates (Dunn

1983; Wang, Dembo et al. 2001), linear speed (S, in μm/min) was calculated by simply dividing the integrated travel distance with the total time, *T* (Eq. 1, where x_i and y_i are coordinates at frame *i*).

$$S = \frac{\sum \sqrt{(x_i - x_{i-1})^2 + (y_i - y_{i-1})^2}}{T} \quad (1)$$

Note that this approach is unaffected by the turning behavior whereas the previous approach based on mean squared displacements is sensitive to migration pattern (Wang, Dembo et al. 2001). Average acceleration of velocity (*A*, in μm/min^2, Eq. 2) was calculated based on changes in the distance of travel along x- and y-directions between three consecutive frames.

$$A = \frac{\sum \sqrt{\left((x_i - x_{i-1}) - (x_{i-1} - x_{i-2})\right)^2 + \left((y_i - y_{i-1}) - (y_{i-1} - y_{i-2})\right)^2}}{T^2} \quad (2)$$

A turn was defined as a change in direction of at least 30o between two consecutive intervals of recording with a distance of at least 2.0 μm in the interval following the change in direction. The total number of turns for each series was then divided by the recording time to yield average turns per hour. Unpaired student's t-tests were performed using GraphPad© software and all data represented as mean ± standard error of the mean (s.e.m.) unless otherwise indicated. Average lifespan of focal adhesions was determined using cells transfected with EGFP-paxillin, as the length of time between the appearance and disappearance of dot-like to elongated structures (Horwitz and Parsons 1999). The average was calculated from 27 focal adhesions in 4 cells in each group.

2.3.d. Fixation and staining of cells

Cells were rinsed twice with 37°C phosphate buffered saline (PBS), and fixed with 4% paraformaldehyde (Electron Microscopy Sciences, Fort Washington, VA) and 0.2% Triton x-100 (Sigma) in PBS for 10 min. After rinsing twice in PBS with 1% bovine serum albumin (Sigma) for 10 min each, focal adhesions were stained with a monoclonal anti-vinculin antibody (1:100 dilution; Sigma), and Alexa-546 goat anti-mouse secondary IgG (1:100 dilution, Molecular Probes, Eugene, OR). Cells were counter-stained with Alexa-488 phalloidin (Molecular Probes, Eugene, OR) to visualize actin filaments, following manufacturer's instructions.

Fluorescent images were obtained using a Zeiss Axiovert-10 microscope with a Roper Scientific NTE/CCD-512-EBFT camera. A Zeiss Fluar 100x N.A. 1.30 phase objective lens was used to acquire fluorescence images as optical slices at a distance interval of 0.25 μm. Images were deconvolved with a constrained iterative algorithm using custom software. In addition, low-magnification fluorescence images, along with phase contrast images, were collected with a Neo-Fluar 40x N.A. 0.75 lens for morphometry. Cellular processes, defined as non-overlapping, vinculin plaque-containing regions of the cell boundary where the distance from cell center is longer than both neighboring regions, were determined from phalloidin and vinculin images. The perimeter, p, of each cell was traced by hand on phalloidin-stained images and the spread area, A, computed based on the number of pixels within the perimeter. Form factor, a measure of the degree of branching in cell shape, was then calculated as $4\pi A / p^2$. Cells

with a spread area between 485 and 1725 μm^2 were included in the analysis of cellular processes and form factor, to exclude rounded or abnormally large cells.

2.3.e. Fibronectin adsorption and characterization

To determine if fibronectin (FN) in the media was adsorbed uniformly over the surface of pillar substrates, FN was fluorescently labeled and the relative intensities on top and in between pillars were compared. Substrates were incubated overnight in the medium used for 3T3 cells, rinsed and incubated twice with 37°C phosphate buffer saline (PBS) with 1% bovine serum albumin (Sigma) for 10 min each, and then labeled sequentially with a monoclonal anti-FN antibody (1:100 dilution; Sigma), and Alexa-488 goat anti-mouse secondary IgG (1:100 dilution, Molecular Probes, Eugene, OR) for 45 and 30 min respectively. Fluorescent images were acquired as described above with a Zeiss Fluar 100x N.A. 1.30 phase objective lens. Intensities measured on top and in between pillars (n = 50 for each from two substrates) were corrected by subtracting average background fluorescence measured on similar substrates prepared without the primary antibody.

2.4. Results

2.4.a. Pillar topography induces branched morphology and erratic movement of 3T3 fibroblasts

To create substrates with topographic features, coverslips were coated with polystyrene and pillar features were cast on part of the surface using

polydimethylsiloxane (PDMS) molding (see Materials and Methods). The topographic feature consisted of cylindrical pillars that were on average 1.78 μm in height, 10.30 μm in diameter, and 15.76 μm in center-center spacing as determined by atomic force microscopy (Fig. 2.1). The entire substrate was then modified by reactive ion etching to promote cell adhesion. The resulting surfaces were chemically similar to that of conventional polystyrene tissue culture dishes. Flat and pillar regions shared identical chemical properties and differed only in topographical features. Quantitative immunofluorescence indicated that the surface was coated similarly with FN on top of the pillars and in the flat region between pillars (relative intensities of 49.9 ± 2.4 on top of pillars and 48.1 ± 1.6 in between pillars, *p*-value = 0.592).

NIH 3T3 fibroblasts on pillar substrates were able to follow the topography and form focal adhesions on the top and sides of the pillars, and in the flat regions between pillars (Fig. 2.2). Compared to those on the flat substrates, focal adhesions on pillar substrates appeared smaller in size (Fig. 2.2). In addition, cells on pillars appeared to be more branched in shape (Fig. 2.3, A, B, and C), as confirmed by measuring the form factor (defined as 4π area / perimeter2; more convoluted shapes show a longer perimeter relative to the area, thus a smaller form factor). I obtained a value of 0.161 ± 0.010 for cells on pillar substrate and 0.230 ± 0.014 for cells on the flat region (*p*-value = 0.0001, Fig. 2.3 D), confirming that cells on pillar substrates have a more complex shape.

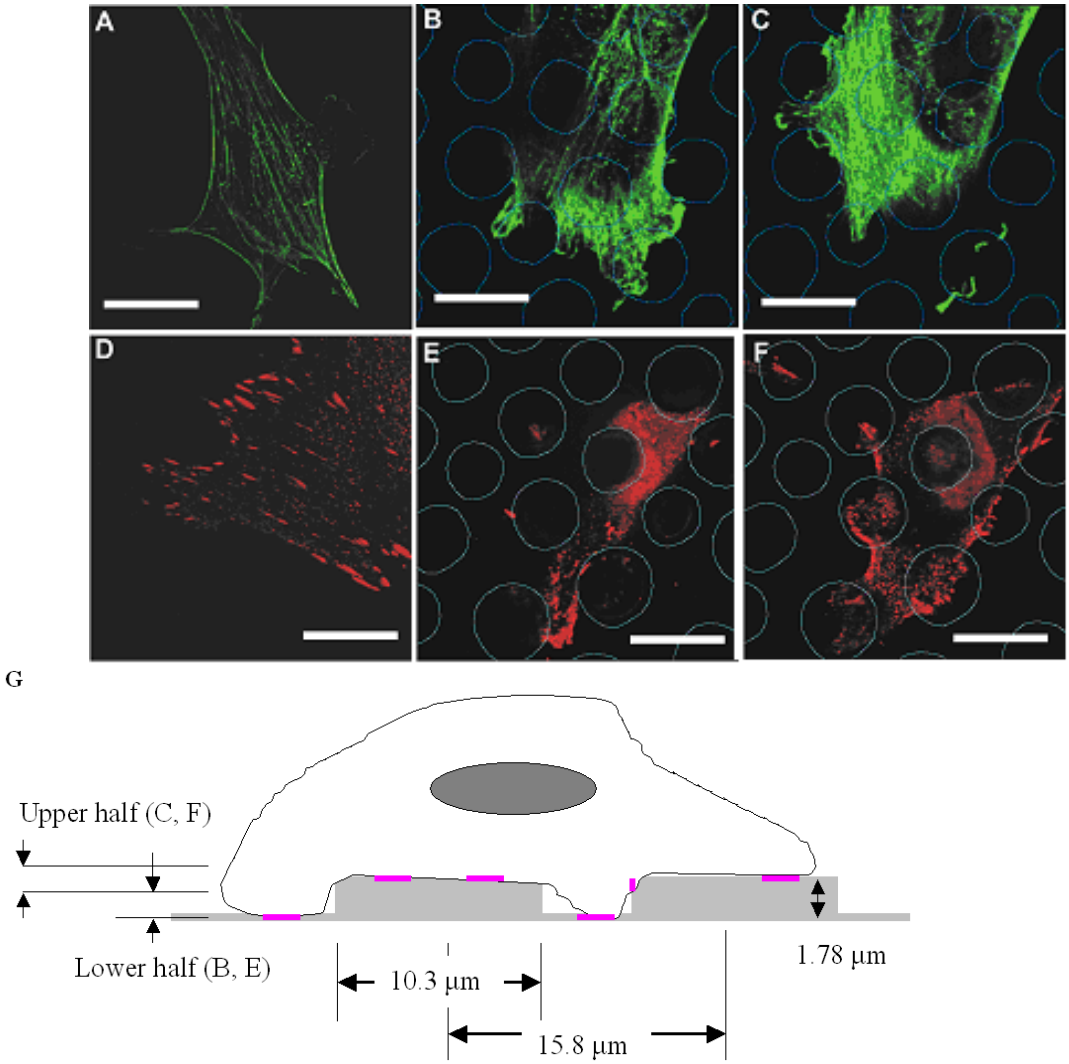

Figure 2.2. Focal adhesions and stress fibers in NIH 3T3 cells on pillar and flat substrates.

NIH 3T3 cells on flat (A, D), or pillar (B and C, E and F) substrates were fixed and stained for actin filaments (A, B, and C), or vinculin (D, E, and F). Optical sections were deconvolved and partially reconstructed to show structures of the cell in the upper (C, F), or lower half (B, E), of the pillar (schematic, G). Pillars were indicated as circles. On pillar substrates, focal adhesions form both on pillars and on the flat surface between pillars. In addition, cells appeared to form more prominent focal adhesions on flat substrates than on pillar substrates. Bar, 20 µm.

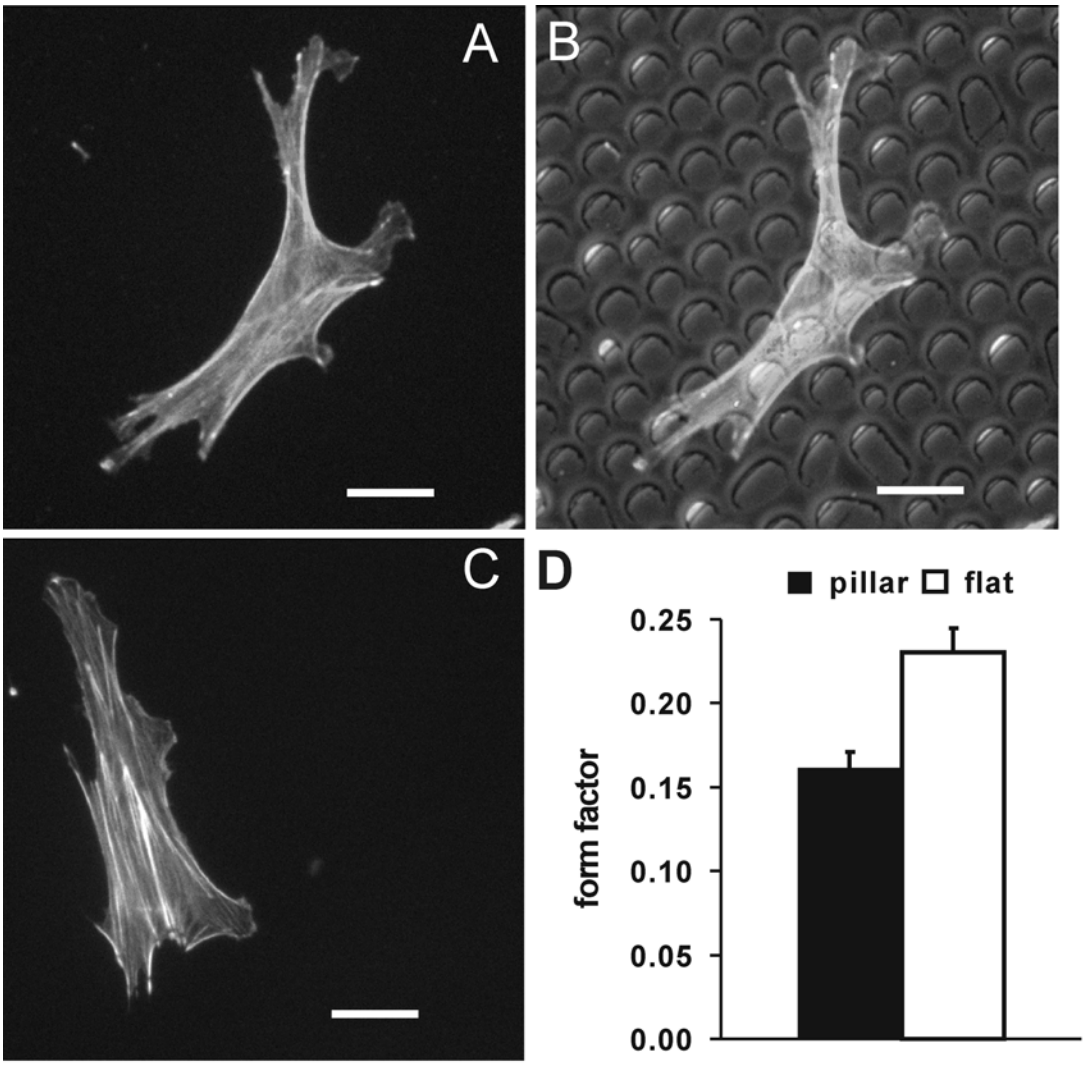

Figure 2.3. Morphology of NIH 3T3 cells on pillar and flat substrates

Phalloidin staining shows a more branched morphology for cells on pillar substrate (A, B), than cells on flat substrate (C). Images of phalloidin and vinculin were merged (A, C), then merged with phase contrast image to show the location of pillars (B). Bar, 20 μm. Shape complexity is quantified by calculating the form factor (D); more branched shape yields a smaller form factor. Bars represent mean ± s.e.m. for 33 cells under each condition.

I noticed that branches of the cell appeared to associate preferentially with pillars (Fig. 2.3 B). Quantitative analysis of fluorescently stained cells confirmed that vinculin-containing cellular processes were twice as likely to terminate at pillars as in the region between pillars (66.9% verses 33.1% from 25 cells), even though pillars account for only ~ 46% of the total surface area. These observations may be explained if pillars promote stable cell adhesion.

The branched morphology and the preferential association of cellular processes with pillars suggest that pillar topography may affect cell migration. I found that cells on pillar substrates moved in a zigzag fashion, as if they were dragged from pillar to pillar by the anchored extensions (Fig. 2.4 A). Quantification of the frequency of turns confirmed this observation (3.74 ± 0.43 turns/hr vs. 1.17 ± 0.39 turns/hr for pillar and flat substrates respectively, *p*-value = 0.0006, Fig. 2.4 B). Measurements of cell movement indicated that cells on pillar substrates moved at a significantly higher linear speed than those on flat regions (0.692 ± 0.051 μm/min vs. 0.459 ± 0.077 μm/min, respectively, *p*-value = 0.0246; Fig. 2.4 C). The irregular movement was further supported by measuring the vectorial acceleration, which decreased from 0.153 ± 0.011 μm/min2 on pillars to 0.094 ± 0.015 μm/min2 on flat substrates (*p*-value = 0.0071; Fig. 2.4 D) due to less frequent changes in direction on flat substrates (Fig. 2.4 A and B).

2.4.b. Responses to pillar topography involve stabilization of focal adhesions and myosin II-dependent contractility

The preferential association of cellular processes with pillars and the erratic pattern of cell movement suggest that the pillar topography promotes stable cell adhesion.

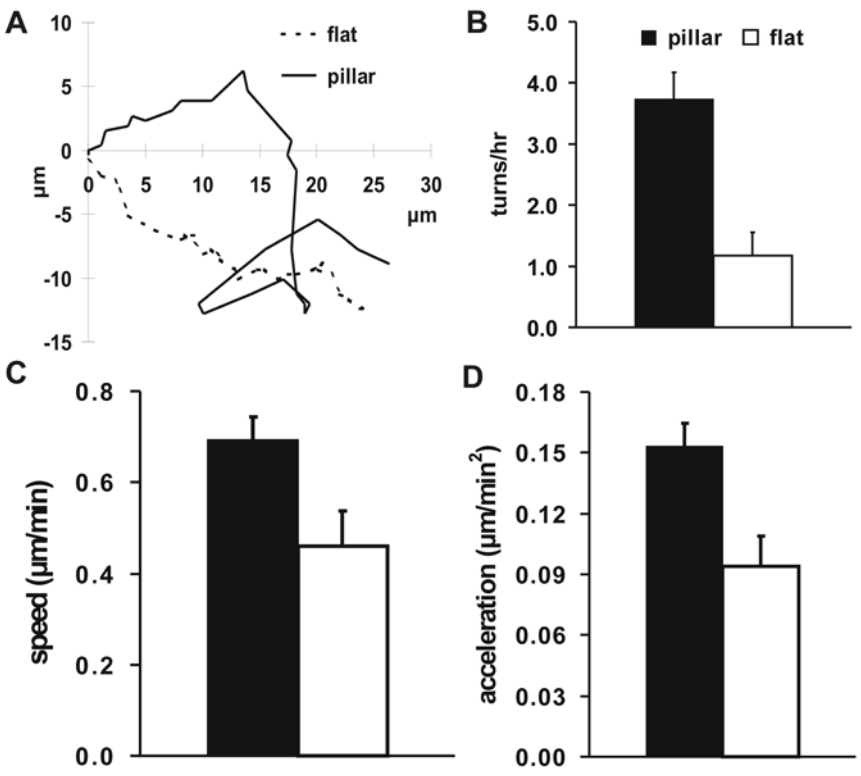

Figure 2.4. Migration characteristics of NIH 3T3 cells on pillar and flat substrates

Representative paths of cell migration, as determined by tracing the nuclear centroid over a period of 2 hr, show a longer, more zigzag path on the pillar substrate (A, solid line), than on the flat substrate (A, dotted line). The differences are quantified by measuring the turning frequency (B), the linear speed (C), and vectorial acceleration (D). Compared to cells on flat substrates, those on pillar substrates show a significantly higher turning frequency (B, filled bar), linear speed (C, filled bar), and vectorial acceleration due to frequent changes in direction (D, filled bar). Bars represent mean ± s.e.m. for 8 cells (B, C, D).

To address this possibility, I measured the turnover of focal adhesions on pillar and flat surfaces, using NIH 3T3 cells transfected with EGFP-paxillin to label focal adhesions (Rottner, Krause et al. 2001). The average lifespan of focal adhesions (time of appearance to disappearance of dot-like structures) on pillars was 40.74 ± 4.01 min, compared to 21.11 ± 0.98 min for those on flat surfaces between pillars (*p*-value < 0.0001, Fig. 2.5), indicating that topographic features increase focal adhesion stability.

The zigzag migration pattern on pillar substrates further suggests that contractile forces may play a role, by dragging cells from pillar to pillar. To determine if myosin II is involved in this process, I treated cells with blebbistatin, a potent inhibitor of non-muscle myosin II ATPases (Straight, Cheung et al. 2003). Blebbistatin treated cells showed a highly elongated, irregular morphology independent of substrate topography (Fig. 2.6 A and B). Although the cells remained motile, neither the linear speed (0.384 ± 0.028 vs. 0.408 ± 0.052 for pillar and flat respectively, p-value = 0.6943; Fig. 2.6 C), nor the vectorial acceleration (0.111 ± 0.008 vs. 0.099 ± 0.012 for pillar and flat respectively, p-value = 0.3523; Fig. 2.6 D), responded to the pillar topography. These results suggest that myosin II provides the driving forces for the detection and/or responses of 3T3 cells to substrate topography.

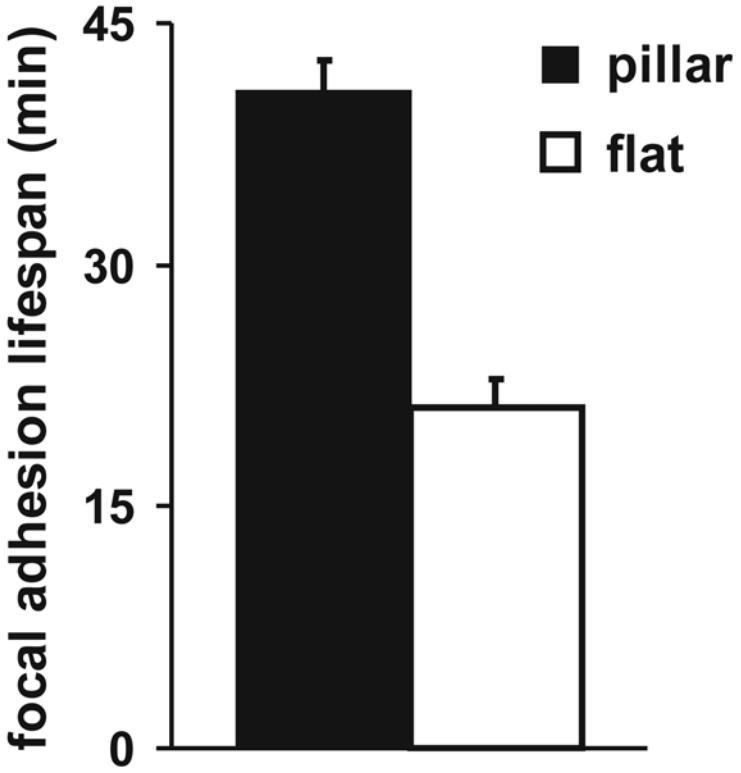

Figure 2.5. Stability of focal adhesions on pillar and flat substrates

Average life span of focal adhesions, determined using NIH 3T3 cells expressing EGFP-paxillin, indicates a high stability for focal adhesions on pillars than those on the flat surface between pillars. Bars represent mean ± s.e.m. for 20-30 focal adhesions in 4 cells under each condition.

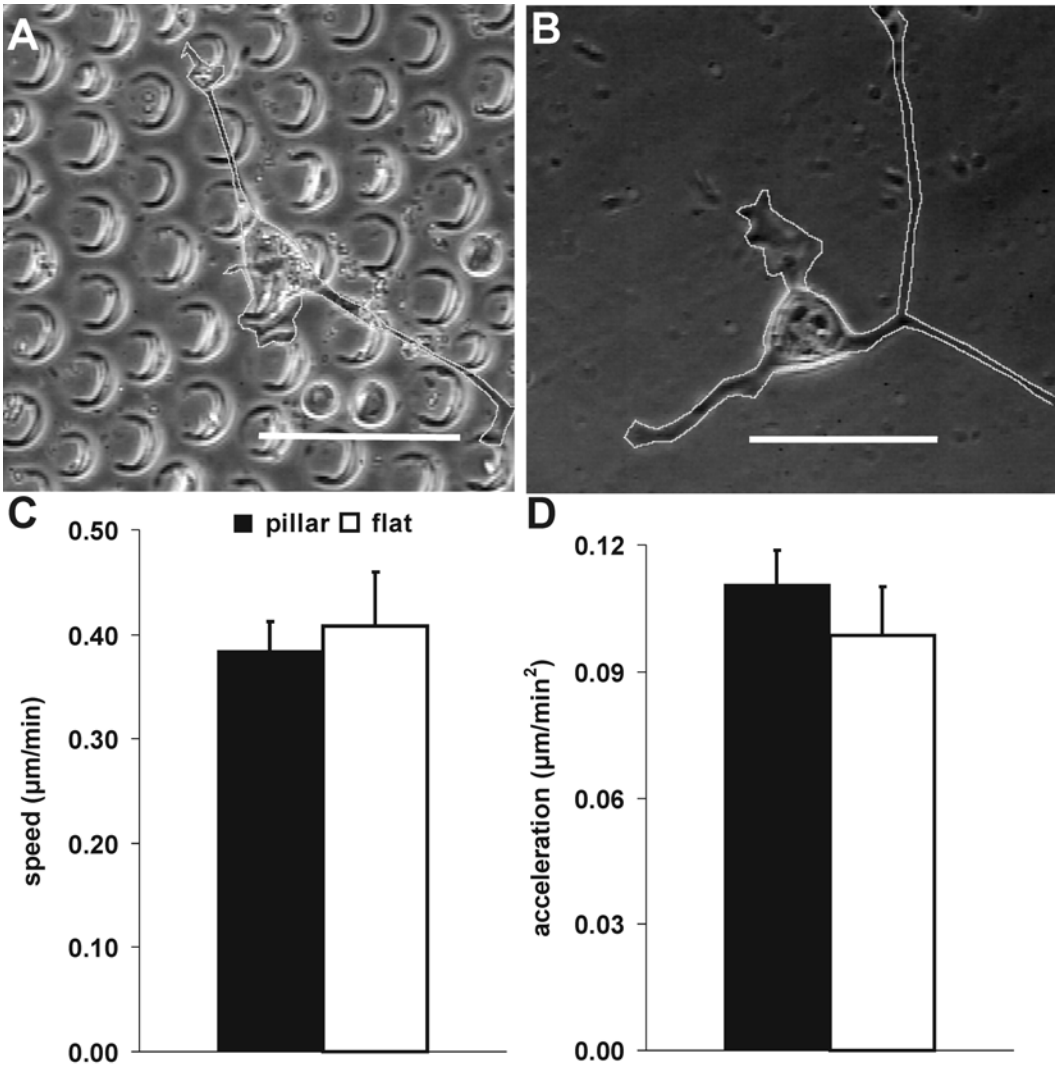

Figure 2.6. Effect of myosin inhibitor on NIH 3T3 cells plated on pillar and flat substrates

Cells are treated with 100 μM blebbistatin for at least 2 hr prior to imaging. Approximate boundaries, drawn for clarity due to poor contrast relative to pillars, show a similar elongated and irregular shape on pillar (A) and flat (B) substrates. Bar, 50 μm. Linear speed (C) and vectorial acceleration (D), calculated as for Figure 4, also show statistically similar values. Bars represent mean ± s.e.m. calculated for 8 cells under each condition.

2.4.c. Responses to substrate topography require FAK

Previous experiments demonstrated that FAK is required for cellular responses to mechanical stimulation (Wang, Dembo et al. 2001). To determine if FAK is required for the responses to substrate topography, I analyzed time-lapse images of FAK -/- fibroblasts re-expressing FAK under the control of a Tet-off system. FAK expression was inhibited when cells were cultured in the presence of tetracycline. Removal of tetracycline for 36– 48 hours induced re-expression of FAK (Owen, Ruest et al. 1999). Rescued cells responded to the pillar topography in a similar manner as did NIH 3T3 cells. The extensions showed a preferential association to pillars, as 61.1% of processes terminated on pillars versus 38.9% in between pillars (data from 24 cells, Fig. 2.7 A), and an increased frequency of turns on pillar substrates (5.14 ± 0.43 turns/hr vs. 2.34 ± 0.28 turns/hr for pillar and flat substrates respectively, *p*-value = 0.0001; Fig. 2.8, A, B, and E). As for 3T3 cells, rescued cells showed a lower form factor (0.155 ± 0.008 vs. 0.188 ± 0.010, *p*-value = 0.0094; Fig. 2.7 C), higher linear speed (0.870 ± 0.109 μm/min vs. 0.394 ± 0.024 μm/min, *p*-value = 0.0008; Fig. 2.8 C), and higher vectorial acceleration (0.263 ± 0.032 μm/min2 vs. 0.102 ± 0.005 μm/min2, *p*-value = 0.0002; Fig. 2.8 D), on pillar than on flat substrates. In addition, compared to rescued cells on flat substrates, those on pillars displayed a greater number of extensions, most of which terminated at a small ruffling region on a pillar (Fig. 2.7 A).

In contrast to rescued cells, FAK-/- cells showed no detectable response to the pillar topography (Fig. 2.7 A). Comparisons of migration paths indicated a similar pattern on the pillar and flat substrates (Fig. 2.8, A and F), confirmed by the similar

turning frequency (2.44 ± 0.34 turns/hr vs. 2.04 ± 0.31 turns/hr for pillar and flat substrates respectively, *p*-value = 0.4017, Fig. 2.8 B). In addition, cellular processes showed a reduced tendency to terminate at pillars (48.9% vs. 51.1% for pillar and between pillars from 25 cells). The form factor (0.219 ± 0.013 vs. 0.235 ± 0.013, *p*-value = 0.3834; Fig. 2.7 C), linear speed (0.427 ± 0.044 μm/min vs. 0.471 ± 0.028 μm/min, *p*-value = 0.4248; Fig. 2.8 C), and vectorial acceleration (0.137 ± 0.017 μm/min2 vs. 0.108 ± 0.008 μm/min2, *p*-value = 0.1479; Fig. 2.8 D) all remained similar on pillar and flat substrates. The linear speed of FAK-/- cells was similar to that for FAK rescued cells on flat substrates (0.394 ± 0.024 μm/min vs. 0.471 ± 0.028 μm/min, *p*-value = 0.0553, Fig. 2.8 C; to be distinguished from root mean squared displacement based speed (Wang, Dembo et al. 2001), see Materials and Methods) (Tilghman, Slack-Davis et al. 2005; Braren, Hu et al. 2006). FAK -/- cells also showed a less convoluted shape and lower ruffling activities than rescued cells on flat surfaces (form factor of 0.235 ± 0.013 vs. 0.188 ± 0.010, *p*-value = 0.0052; Fig. 2.7, A and C).

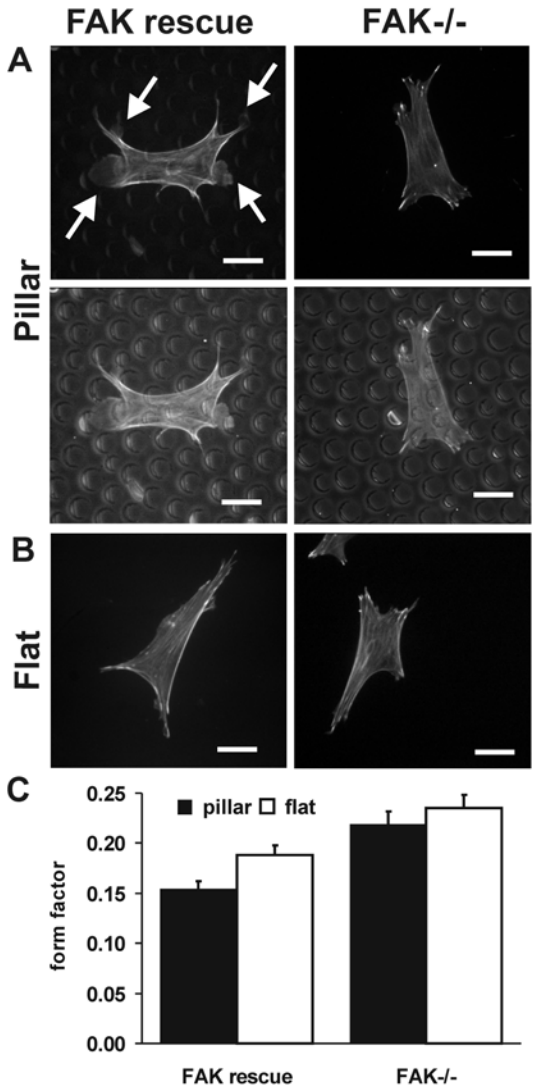

Figure 2.7. Morphology of FAK-/- and rescued cells on pillar and flat substrates

Phalloidin staining shows a more convoluted shape for rescued cells on pillar substrate (A), than on flat substrate (B), while FAK -/- cells show a similar simple shape on both substrates. In addition, FAK -/- cells show reduced ruffling activities on either pillar or flat substrate compared to FAK-expressing cells (A, arrows). Distribution of the pillars is shown in the merged fluorescence and phase contrast images (A, bottom row). Bar, 20 μm. Shape complexity, quantified by the form factor (C), indicates that FAK -/- cells fail to respond to the pillars while rescued cells show statistically significant responses similar to NIH 3T3 cells. Bars represent mean ± s.e.m. for 33 cells under each condition.

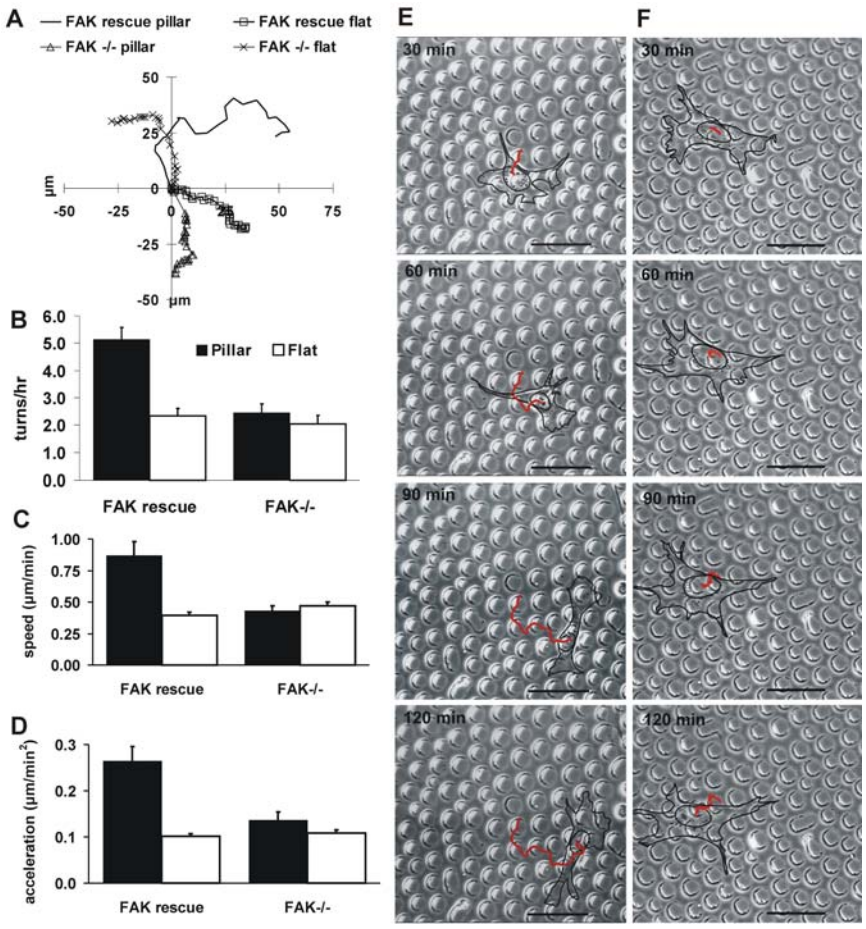

Figure 2.8. Migration characteristics of FAK-/- and rescued cells on flat and pillar substrates

Migration patterns of representative cells (chosen based on linear speed) indicate that rescued cells move in a more zigzag pattern on pillar substrates than on flat substrates, unlike the similar migration patterns of FAK -/- cells on pillar and flat substrates. Quantification of turns confirms these observations (B). In addition, linear speed (C) and vectorial acceleration (D) of FAK -/- cells fail to respond to the pillars, while those of rescued cells respond in a way similar to 3T3 cells. Linear speed and vectorial acceleration for FAK -/- and rescued cells were analyzed as for 3T3 cells shown in Figure 4. Bars represent mean ± s.e.m. for 8 cells under each condition. Representative sequences of phase contrast images for rescued (E), and FAK -/- cells (F), on pillar substrates also show a lack of turning responses to pillars for FAK -/- cells. Due to low contrast on pillar substrates, approximate cell boundaries are traced in black and migration paths indicated in red. Bar, 50 μm.

2.5. Discussion

Although the phenomenon of contact guidance has been known for decades (Weiss 1941), the mechanism of cellular responses to substrate topography remains poorly understood. Pillar substrates allow migrating cells to continuously encounter localized topographic stimuli, and facilitate direct comparison of cell behavior on surfaces with or without topographic features. Compared to cells on flat surfaces, 3T3 cells on pillar substrates showed a more branched shape, increased linear speed, and decreased directional stability. The pillars appeared to serve as preferred sites for ruffling activities and anchorage, as extensions of 3T3 fibroblasts were more than twice as likely to terminate at a pillar than in between pillars at a given time, even though the pillar surface area accounted for less than one-half of the total surface area.

Observations of focal adhesions and blebbistatin treatment provided mechanistic insights into the responses to topographic signals. Stable association at pillars was likely caused by localized stabilization of focal adhesions, as shown by the decrease in the turnover rate of focal adhesions on pillars from that on flat regions between pillars. Anchorage to pillars was typically followed by contractions of the cell extension, causing acceleration toward the pillars and abrupt changes in direction. This enhanced contraction may account for the increase in linear speed despite the increased stability of focal adhesions. In addition, inhibition of the responses to surface topography by blebbistatin suggests that myosin II-dependent contraction plays a role in the process, possibly by providing forces for the cell to surge toward stabilized adhesions at pillars.

Similar combinations of localized enhancement of adhesions and contractions would readily explain cellular responses to other topographic features, including the alignment with grooves in classic contact guidance.

The response to surface topography may involve responses to surface curvature or to increased substrate contact area. However, since grooves and ridges, and pits and pillars, were previously found to induce similar responses (Clark, Connolly et al. 1990; Wojciak-Stothard, Madeja et al. 1995; Walboomers, Monaghan et al. 1999; Curtis, Casey et al. 2001; Berry, Campbell et al. 2004), the sign of the curvature does not appear to play an important role. Instead, it is probably the density of anchored surface receptors relative to cell volume that is responsible for the stimulation. Interestingly, large pits and/or spacing were reported to inhibit cell migration (Berry, Campbell et al. 2004). This may be explained if cells were unable to straddle multiple pillars or pits under these conditions, such that strong anchorage to single topographic features may limit the ability of cells to migrate onto the surrounding flat surface.

The responses to surface topography appear very similar to the responses to substrate rigidity. Previous studies have shown that fibroblasts exert stronger traction forces on stiff substrates than on soft substrates (Lo, Wang et al. 2000). Moreover, cells also adhere more tightly to stiff substrates than to soft substrates, as shown by a centrifugation assay and by a microsphere peeling assay (Griffin, Engler et al. 2004; Guo, Frey et al. 2006). Similar increases in cellular spreading, migration speed, and traction forces were reported in response to increases in collagen surface density (Gaudet, Marganski et al. 2003). Thus, mechanical and topographic signals may elicit similar

responses, causing cells to steer toward maximal stimulation through enhancements of anchorage and contraction.

While detailed mechanism for the transduction of such topographic or physical signals is unclear, one possibility is that mechanical forces transmitted through integrins may cause an associated sensing protein on the cytoplasmic side to change its conformation and enzyme/substrate activities. Mechanical forces are also known to cause calcium entry through ubiquitous stretch-sensitive channels, and activate a number of potential downstream effectors including calmodulin and myosin II (Lee, Wong et al. 1999#52). Topographic features may induce similar responses, by increasing the density of local contacts and associated signals relative to the cell volume.

Although FAK has been recognized as a key enzyme in regulating cell migration (Parsons 2003), its functional role remains poorly defined. I showed that cellular responses to surface topography require FAK. The cell shape, linear speed, and migration pattern for FAK-/- cells were similar on flat and pillar substrates, as if FAK -/- cells were blind to the presence of pillars. Consistent with this idea, FAK-/- cells lacked the response to substrate stiffness (Wang, Dembo et al. 2001). Furthermore, I observed limited lamellipodia formation in FAK -/- cells on both flat and pillar substrates, while FAK-expressing cells showed localized enhancement of ruffling activities on pillars. Cells treated with siRNA against FAK showed a similar reduction in ruffling activities, suggesting that FAK is required for the activation of membrane protrusion and cell polarity (Tilghman, Slack-Davis et al. 2005). These observations indicated that FAK is

involved in the detection of adhesion-mediated physical signals, possibly by amplifying the cytoplasmic chemical responses.

The physiological role of micron-scaled topographic signals remains largely unexplored *in vivo*. These signals may be created by aggregation or fibrillar assembly of ECM proteins. In addition, topographic signals may arise as a result of cell shape changes or cell-cell interactions. As demonstrated in the present and previous studies with FAK -/- cells (Wang, Dembo et al. 2001), defects in responses to mechanical or topographic signals may lead to relatively minor phenotypes when cells were examined under conventional culture conditions, but severe consequences under conditions where these signals play a major role such as during embryonic development or wound healing. Given the profound effects on cell shape, adhesion, and migration, topographic features also represent an important factor in the engineering of artificial tissues and prosthetic devices.

CHAPTER 3. MICROSCOPIC METHODS FOR MEASURING THE ELASTICITY OF GEL SUBSTRATES FOR CELL CULTURE: ATOMIC FORCE MICROSCOPY AND MICROINDENTATION

3.1. Abstract

In conjunction with surface chemistry, mechanical properties of cell culture substrates provide important biological cues that affect cell behavior including growth, differentiation, spreading, and migration. The phenomenon has led to the increased use of biological and synthetic polymer-based flexible substrates in cell culture studies. However, widely used methods for measuring the Young's modulus have proven difficult for the characterization of these materials, as they tend to be relatively thin, soft, hydrated, and tethered to glass substrates. Described here are two methods that have been applied successfully to probe the flexibility of soft culture substrates. Although the first method, atomic force microscopy (AFM), is well described in the literature, the analysis of the data proves difficult. I have optimized AFM for soft samples using a standard means of analysis as well as a new method to reduce subjectivity and improve reliability. In addition I describe a novel microsphere indentation method, designed to address the need to quickly assess the stiffness and measure *in situ* changes in stiffness on a standard fluorescence microscope.

3.2. Introduction

Studies performed on soft substrates have highlighted the important influence of substrate mechanics on cell adhesion, cell structure, and cell mechanics (Engler, Bacakova et al. 2004; Guo, Frey et al. 2006; Radmacher 2007; Solon, Levental et al. 2007). These studies rely upon reliable measurements of Young's modulus of culture substrates (Janmey, Georges et al. 2007). However, classical methods for measuring material elasticity and other mechanical properties generally require macroscopic samples, often of a specific geometry, while gels intended for cell culture are generally formed as a thin layer adhered to the culture dish. Reliable measurements of such gels must be performed *in situ*, because (i) gels can be so soft that macroscopic samples are difficult to handle, (ii) gels are hydrated and sometimes temperature sensitive, thus small, thin samples are more homogeneous and easier to control, (iii) gels are often tethered to the underlying cover glass, which may affect the expansion or compression of gels, and (iv) with cells adhering to the gel surfaces, measuring the elasticity of the adjacent gel surface instead of the bulk should provide values more relevant to cell behavior.

The purpose of this chapter is to describe two microscopic methods suitable for measuring the elasticity of gel substrates *in situ*. While both are based on Hertz contact mechanics (Hertz 1882), namely the indentation in response to forces exerted with a probe of known geometry, they differ substantially in cost, simplicity and resolution. The first is AFM. Since this approach has been described in the literature, the description

here will be limited to several key aspects critical to gel measurements and a new analytical technique and algorithm to improve the reliability. The second method is microsphere indentation, which was developed as both a qualitative and quantitative tool for probing substrates on the stage of a fluorescence microscope.

3.3. Materials and methods

With both methods, the measurements should be performed on fully acclimated substrates since hydrogel substrates are often sensitive to buffer conditions and temperature. In addition, the thickness of the testing sample should be close to that used for actual experiments. This is particularly important for polyacrylamide gels, since the surface rigidity decreases progressively with increasing thickness due to the covalent bonding of the gel to the coverslip to limit gel swelling and prevent detachment (Kandow, Georges et al. 2007).

3.3.a. Preparation of polyacrylamide gels

Polyacrylamide substrates were prepared as described previously (Wang and Pelham Jr. 1998). The substrates contained 5% total acrylamide and 0.012% (referred to as soft substrates) or 0.1% bis-acrylamide (referred to as stiff substrates). Young's moduli of the substrates were determined by AFM. A volume of 30 μl was plated onto 45 mm diameter glutaraldehyde activated glass coverslips (Laboroptik GmBH, Germany) (Alpin and Hughes 1981), covered with a 22 mm coverslip and allowed to polymerize for 30 minutes. The substrate was then immersed in phosphate buffer solution (PBS), the top coverslip removed, and stored at 4˚C until testing in PBS no more than three days later.

To create a hydrated chamber for testing, holes were drilled into the base of 50 x 9 mm Petri dishes (Becton Dickinson Labware, Franklin Lakes, NJ) using a cup saw on a drill press. The bottom surface was then layered with vacuum grease and pressed down onto the circular coverslips carrying the substrates.

3.3.b. Measuring gel rigidity with atomic force microscopy

The measurements were performed using an Autoprobe M4 AFM (Veeco; Santa Barbara, CA) equipped with ProScan V1.51b software (Veeco; Santa Barbara, CA) and a MicroCell Kit (APMC-0001, Veeco; Santa Barbara, CA) for hydrated samples. Measurements were performed with the following probes for AFM. The first was a Particle Tip - Contact Mode probe (BioForce Nanosciences, Inc., Ames, IA) with a 5 μm spherical borosilicate tip on a cantilever with a nominal spring constant of 0.06 nN/nm. The second was constructed by gluing 20 μm polystyrene beads (Polysciences; Warrington, PA) onto CSC12 tipless cantilevers (MikroMasch; Wilsonville, OR) with nominal spring constants of either 0.05 and 0.03 nN/nm, using Optical Adhesive #71 (Norland Products, Inc; Cranbury, NJ) cured for 30 minutes under ultraviolet light.

The stiffness of each cantilever was more accurately determined using a thermal calibration method before measurements were made on the substrates (Burnham, Chen et al. 2003). The geometry of both spherical and conical tips was determined accurately by imaging a TGZ03 step grating (MikroMasch; Wilsonville, OR). The spherical cap portion of the resulting profile was fit to a spherical model to yield the tip radius (Thoreson and Burnham 2004). Similar tip imaging using a TGZ01 step grating was

used to verify the half-open angle of conical tips. Force-indentation profiles were obtained at a rate of 1 Hz. Reported rigidity of the gel substrates were the average +/- uncertainty, obtained from either 16 or 10 force curves (n = 15 and 13 taken at various locations on 3 and 4 samples for the stiff and soft samples, respectively).

For validation of the algorithm (described later), testing was conducted on 5% acrylamide and 0.1% bis-acrylamide gels. Measurements were performed with CSC12 cantilevers with a pyramidal tip of 35˚ half open angle and nominal radius of 20 nm (MikroMasch; Wilsonville, OR) with nominal spring constants, *k*, of either 0.05 or 0.03 nN/nm. Force-indentation profiles were obtained at a rate of 1 Hz on multiple samples at various locations.

3.3.c. Preparation of polyacrylamide gels and measuring their rigidity with the microsphere indentation technique

Polyacrylamide substrates were prepared as above using a volume of 30 μl of 5% total acrylamide and 0.025%, 0.06%, and 0.1% bis-acrylamide, as well as 8% total acrylamide and 0.08% bis-acrylamide. Young's moduli of the substrates were determined by the microsphere indentation technique described in detail later. The substrates were tested within three days using probes of radii between 29.7 and 32.9 μm and spring constants between 0.10 to 0.14 nN/nm.

3.3.d. Thickness measurements of gel samples

Thickness measurements were obtained to ensure that thin film corrections were unnecessary (i.e. thickness greater than strain depth). Average sample thickness, ~50 μm,

was determined by epifluoresence microscopy. Samples were prepared and stored as above but with the addition of 1% 0.1 μm fluorescent beads (#16662; Polysciences, Warrington, PA) during polymerization, then sprinkled with 1.0 μm fluorescent beads (Molecular Probes, Eugene, OR) as surface markers. Optical sections were taken on the gels and the sample thickness estimated as the displacement between the focal plane of the lowest embedded beads and that of the surface beads.

3.4. Atomic force microscopy

While the applications of AFM for imaging are relatively well known (Bennig, Quate et al. 1986), AFM can also be used in the 'force mode' to obtain the mechanical properties of materials at nano-scale resolution (Burnham and Colton 1989; Weisenhorn, Hansma et al. 1989). In force mode, the flexible cantilever of AFM is used as a nano-indenter to obtain force-indentation profiles of a sample. The data are then fit to contact models specific for the geometry to obtain the material stiffness.

Cantilevers can be purchased individually or as wafers, with a pre-calibrated spring constant and radii that are more precisely measured prior to use with a thermal calibration method (Burnham, Chen et al. 2003) and tip imaging (Thoreson and Burnham 2004). After calibration for stiffness, the probe is loaded into a moveable scanner (or a fixed scanner with a movable base). The probe tip is aligned using a position-sensitive photodetector, which detects a laser beam deflected off the surface of the cantilever (Fig. 3.1). The deflection is first calibrated on an infinitely stiff surface, whereby the scanner's piezo-driven displacement, z, is equivalent to the measured indentation of the

cantilever, d ($d = z$). Starting from the contact point and moving down into the sample, the change in the tip's angular position is generated by its actual deflection by the material. On a soft sample, the cantilever will indent the sample by a small amount (δ), which must be subtracted from the indentation ($d = z - \delta$). The loading force, F, can then be determined from the measured deflection and the calibrated spring constant of the cantilever, k, using Hooke's Law (Eq. 3):

$$F = kd \quad = k\,(z - \delta) \qquad (3)$$

Plots of force verses indentation, known as force-indentation profiles or force curves, are then fit to the appropriate theoretical model of contact (Eq. 3, plotted as shown in the upper inset of Fig. 3.1), based on the probe geometry (Eq. 4 or 5), to estimate the Young's modulus of the sample.

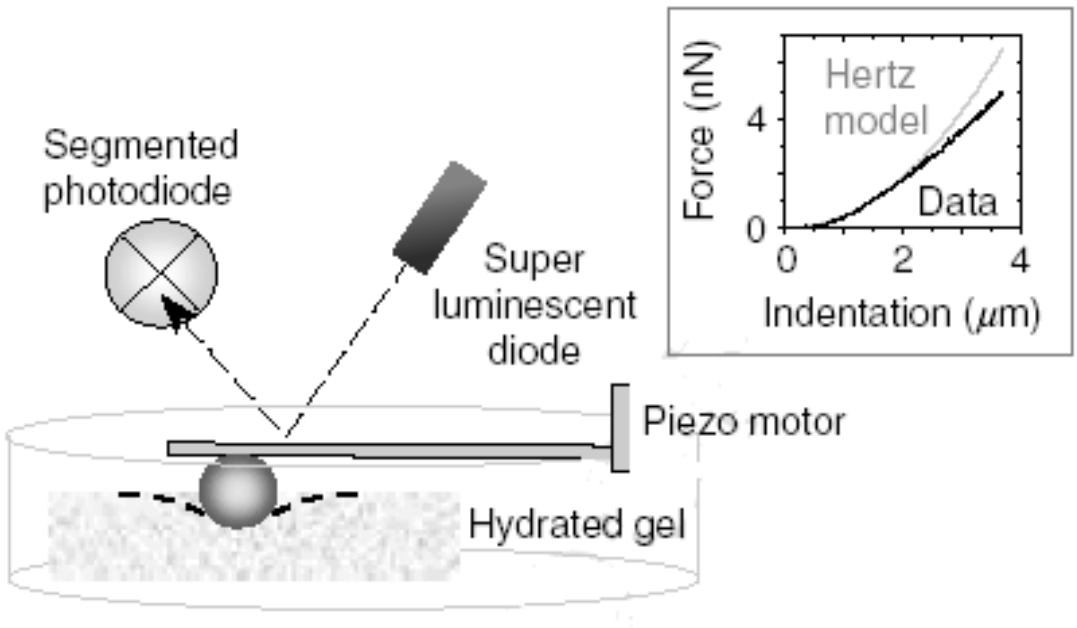

Figure 3.1. Application of AFM for probing the rigidity of gel substrates

Light from a super-intensified diode (or laser) is reflected off the end of a cantilever onto a segmented photodiode that detects small tip deflections with a high sensitivity. Upon pressing the tip into the sample, indentation can be determined as the difference between the tip deflection and the cantilever position and then plotted against the force (black curve, inset), which may then be fit with a Hertz type model (grey curve, inset). (Figure and legend adapted from work contributed by Adam Engler to (Frey, 2007))

3.4.a. Hertz contact mechanics and atomic force microscopy

To obtain the Young's modulus, *E*, of the material, the force-indentation profile is fit to the theoretical model of contact as dictated by the tip geometry, e.g. pyramidal (of shape ∨) with different angles or spherical with different radii, as each probe type imparts a specific deformation pattern and as such, each has an associated mechanical model. The force, *F*, was first related to indentation depth, δ, according to the Hertz equations that describe the deformation of two contacting elastic bodies (Hertz 1882). The theoretical indentation of a planar sample with a spherical indenter of radius, *R*, is also related to the Poisson ratio, ν, and Young's modulus, *E*, of the sample (Eq. 4).

$$F_{sphere} = \frac{4}{3}\frac{E}{(1-\nu^2)}R^{1/2}\delta^{3/2} \tag{4}$$

Sneddon later derived a similar equation for a conical indenter in contact with a flat plane, where θ is the opening angle of the pyramid tip (i.e. – how tapered the tip is; other symbols are the same as defined before) (Eq. 5) (Sneddon 1965).

$$F_{cone} = \frac{2}{\pi}\tan\theta\frac{E}{(1-\nu^2)}\delta^2 \tag{5}$$

For cases where the contact is not ideal, e.g. the material surface is not entirely flat or material has collected on the tip surface, the data may approximate a flat punch for a portion of the indentation. If the stiffness is known or calculated from the equation(s) above, the punch radius, R_p, may be estimated as follows (Eq. 6).

$$F_{punch} = 2R_p \frac{E}{(1-\nu^2)}\delta \qquad (6)$$

3.4.b. Considerations for AFM testing

The spring constant (*k*), shape, and tip size of cantilevers are the main considerations in AFM testing. Cantilever spring constants range from relatively rigid (*k* = 100 – 1000 pN/nm) to soft (5-100 pN/nm). The latter yields larger deflections and a better signal-to-noise ratio when performing measurements on soft gel samples. The tip shape is important when considering the deformation of the sample. Blunted tips (larger contact angles) distribute the deformation over a larger contact area, thus the strain and potential damage to the sample are minimized compared to sharper tips. The indentation of spherical tips scales less strongly with deformation than pyramidal tips (as $\delta^{3/2}$ rather than δ^2), resulting in lower strains of the sample that allows proper corrections for soft, thin films below 20 μm (discussed later) (Dimitriadis, Horkay et al. 2002; Engler, Bacakova et al. 2004; Engler, Richert et al. 2004). Larger spherical tips are also advantageous for testing slightly inhomogeneous materials, as they are less likely to probe within sample irregularities or defects. The expected stiffness and type of material, as well as its geometry should dictate probe selection.

Attention should also be paid to instrument parameters including indentation velocity, indentation distance, and data sampling rate. To probe elastic rather than viscoelastic properties of hydrogels, a modest rate of cantilever displacement 0.2 - 2.0 μm/sec (= *dz/dt*) should be used (Mahaffy, Shih et al. 2000).

3.4.c. Considerations for AFM data analysis

A number of qualifications and conditions apply to the analysis of AFM data. The first step in the determination of *E* by AFM is to select between the tip approach and retraction data for analysis. Analysis of the retraction, or unloading curve, accounts solely for the elastic behavior of the material, unlike the approach, or loading curve, which also contains a component of plastic deformation of the gel (Burnham and Colton 1989; Field and Swain 1993; Jacot, Dianis et al. 2006). Yet analysis of the approach data is common (Engler, Richert et al. 2004; Richert, Engler et al. 2004). I suspect that the reason others use the approach data is that it often lacks the significant adhesion that can occur in the retraction data; a lack of adhesion is a fundamental assumption of the Hertz contact model and its presence would then require the use of more complicated models.

Prior to determining *E*, it is necessary to determine the contact point, or the point at which the tip first makes contact with the substrate. The contact point for soft materials can be less obvious than for harder materials, but a formula from Domke and Radmacher (Domke and Radmacher 1998) can be used to estimate it. It utilizes the deflection (*d*) – position (*z*) plot, in which the intercept with the x-axis is calculated by fitting the curve near two extremes of the region where the curve is to be used for rigidity analysis (Eq. 7).

$$\text{contact point} = \frac{(z_2 - d_2) - (z_1 - d_1) - \left(\frac{d_2}{d_1}\right)^a}{1 - \left(\frac{d_2}{d_1}\right)^a} \qquad (7)$$

The exponent $a = ½$ for a cone (approximating a pyramidal tip) and $a = 2/3$ for a sphere.

However, small inaccuracy in the estimation of the contact point can lead to significant errors in calculating E. The Hertz model assumes a spherical tip in contact with a flat surface, an assumption easily violated due to surface irregularities or material buildup on the tip with repeated use. Adhesive forces between the tip and sample can further obscure determination of the true contact point. Testing hydrated samples using a wet-cell system is thought to eliminate much adhesion, but the contact point can still be difficult to establish for softer samples. While the contact point of data taken with some devices can be estimated directly from a change in slope, interpolation is required for data from many devices (Domke and Radmacher 1998). Even small errors in contact point can lead to significant error in the estimation of Young's modulus (Dimitriadis, Horkay et al. 2002), complicating comparisons of values published in the literature. This is further complicated by subtle differences in the testing equipment, tips and calibration techniques, which data are analyzed (i.e. the approach or retraction curve or the average of the two), the range of analysis (Domke and Radmacher 1998), and the particular mathematical method used to fit the data to the model (explained later).

The values of E typically do not depend on indentation depth for thick films, but the measurements typically fit the Hertz model only at small indentations for thin films (Domke and Radmacher 1998). Analysis of force-indentation profiles obtained on thin gels may require correction with a thin-film approximation (Dimitriadis, Horkay et al.

2002; Engler, Richert et al. 2004). Therefore, the range of analysis should be chosen according to the application.

3.4.d. Error analysis

The estimated uncertainty of the value for E (Eq. 8) is mainly affected by the uncertainty of the value for ν (Taylor 1997); values between 0.3 and 0.5 have been used, though I chose a value of 0.45 in these estimates (Engler, Griffin et al. 2004).

$$\frac{\partial E}{E} = \sqrt{2\left(\frac{\partial \nu}{\nu}\right)^2 + \left(\frac{\partial k}{k}\right)^2 + \left(\frac{\partial d}{d}\right)^2 + \frac{1}{2}\left(\frac{\partial R}{R}\right)^2 + \frac{3}{2}\left(\frac{\partial \delta}{\delta}\right)^2} \qquad (8)$$

Assuming uncertainties of 0.10, 0.02, 0.09, and 0.04 for $\partial k/k$, $\partial d/d$, $\partial R/R$, and $\partial \delta/\delta$, respectively for AFM measurements (Burnham, Chen et al. 2003; Thoreson and Burnham 2004), the uncertainty of E was calculated to be 37%.

3.4.e. Limitations of AFM

The main drawback of AFM is the setup cost, and the limited longevity of the probe due to contamination, which require replacement and calibration of new probes. Measurements of soft hydrogels can also be affected by adhesive interactions between the tip and the gel (Zhao, Shi et al. 2003), which can bias the estimate of contact point. Additionally, unless the AFM is built on top of a high quality light microscope, it will be necessary to move the sample between two different instruments to conduct corresponding microscopic cellular studies and stiffness measurements of the gel. A third instrument may also be necessary to confirm gel thickness, as a thin film correction is required for thin gels (Richert, Engler et al. 2004).

3.5. Reducing subjectivity in AFM data analysis

A major limitation to interpreting and comparing AFM data, particularly for soft samples, is estimating the true contact point. To overcome this difficulty, data can be better analyzed using log-log plots of the force-indentation data. Conversion of non-linear force-indentation data to their logarithmic (linear) forms allows for direct visual confirmation of the transition points for determining the contact position. Thus data may be fit based on actual contact regimes as opposed to adjusting to one estimated contact point and fitting to one simplified model. This can be especially important for conical probes, which have a small spherical tip at the end, and for probing samples under non-ideal contact either from irregularies of the material surface or from materials built up on the tip with repeated use. The use of log-log plots also simplifies the analysis, as it can be performed using simple linear methods, eliminating the need for complicated non-linear mathematical fitting algorithms. These advantages lead to more accurate estimates for the values of E of soft polymer gels. An algorithm programmed in Matlab is developed to further increase the efficiency of this analysis and to automatically determine and optimize the range of analysis (the range over which the data fit well to the model; methodology in Fig. 3.2, Appendices 1-4).

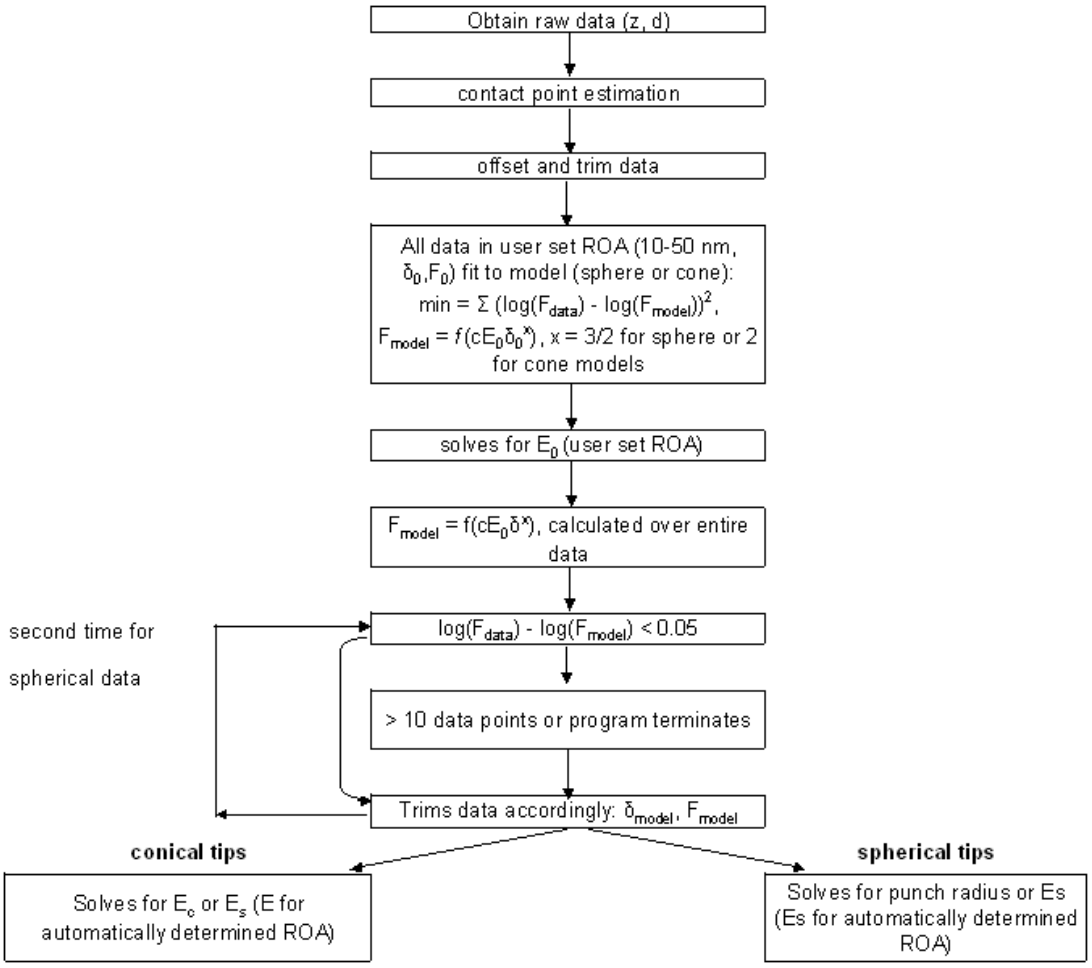

Figure 3.2. Flow diagram for Matlab algorithm

See section 3.5 in text for details.

3.5.a. Estimation of contact point

After initial calibration of the cantilever on glass, force-indentation profiles of the approach and retraction can be obtained (Fig. 3.3, top). With the Autoprobe AFM, the *z-d* (or *F-d*) curves are obtained directly (with the subtraction performed automatically). However, the values must be offset to reflect the actual contact point, as with data obtained with any AFM device. The retraction portion of the force-indentation profiles is used in this analysis to more closely follow the purely elastic Hertz theory (Fig. 3.3, bottom) (Burnham and Colton 1989; Field and Swain 1993; Jacot, Dianis et al. 2006). The contact point can easily be determined as the first point in the *z-d* curve of the retraction data to change slope, which is then used to offset the data (Fig. 3.3, bottom).

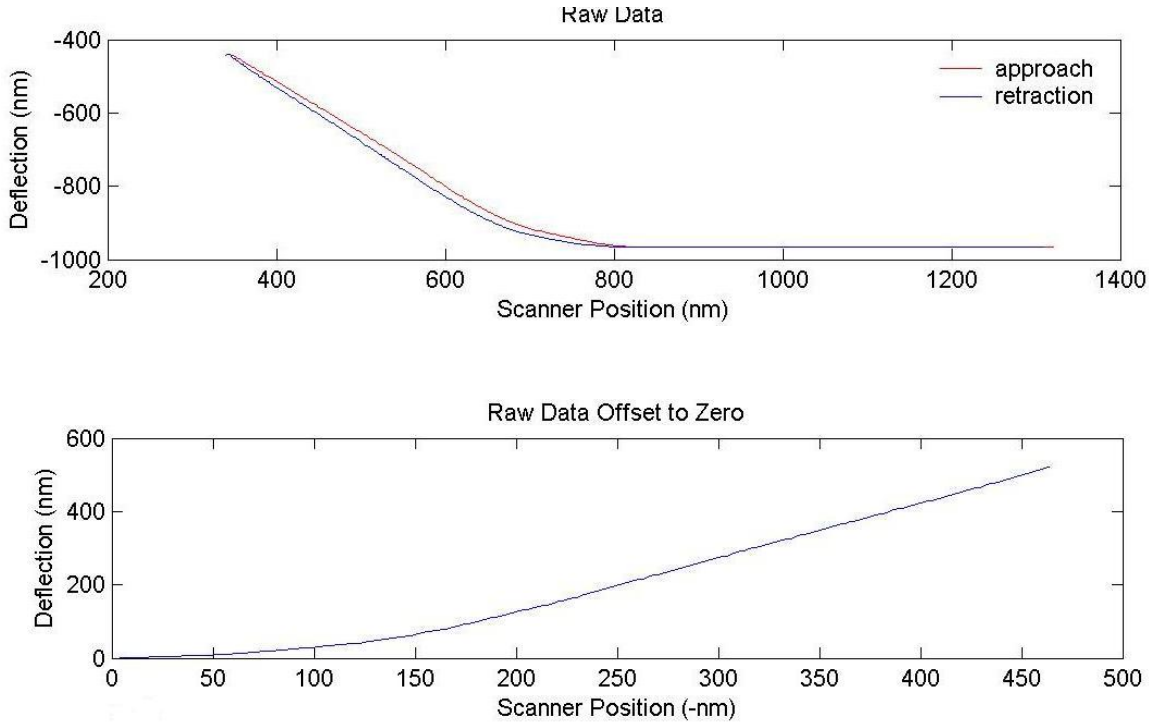

Figure 3.3. Contact point estimation using Matlab algorithm

The contact point is determined from the raw data of deflection versus scanner position as described in the text (top), and offset from the scanner position (bottom, note the sign reversal for scanner position to generate a positive slope).

3.5.b. Initial estimation of elastic modulus based on logarithmic data fitting

Generally, the range of data for which force-indentation profiles are analyzed, or the range of analysis (ROA), is selected by visually truncating the data near the contact point and at higher indentations (i.e. higher strain) (Dimitriadis, Horkay et al. 2002). At lower indentations near the contact point, there is considerable variability in the individual values for E (see Fig. 3.4) (Dimitriadis, Horkay et al. 2002; Richert, Engler et al. 2004), likely due to an underestimation of the contact area by the Hertz model at very small indentation (Fessler and Ollerton 1957; Johnson 1985). There is also a high level of noise at small indentations, likely due to surface interactions between the material and tip and surface irregularities such that contact is not according to the ideal geometry of the model. At higher indentations, the Hertz model may not be appropriate due to behavior other than linear elasticity or to stress stiffening effects of the underlying substrate for thin samples. Therefore, analysis of data for indentations in the range of 10-50 nm is common in the literature.

Once the z-d data are offset, analysis is focused on the portion showing positive, non-linear responses (Fig. 3.3, bottom). For the initial estimation of E in the algorithm, an ROA of 10-50 nm is used (this can be changed within the algorithm). After converting the data to logarithmic values that show linear responses, the data are fit to the logarithmic values of the respective model (Eq. 4 or 5) using the method of minimization of least square error to obtain initial estimates of E (Fig. 3.5 and 3.4). Note that Fig. 3.4 shows data taken with conical tips because the transitions of the tip geometry profiles are

distinct. However, this data cannot be used quantitatively, as the initial cantilever displacement calibration was performed incorrectly, resulting in values that were off by orders of magnitude. The algorithm was, however, validated using spherical data and compared with the other method (discussed later).

3.5.c. Automatic determination of the range of analysis for more accurate estimation of elastic modulus

The initial value for E based on the set ROA is then used as the initial estimate for automatic determination of the optimal ROA for each contact region. In the case of conical tips, the algorithm finds the range of data where the logarithmic values of the model and data differ by 5% or less, and assigns those data to the conical model. For data at lower indentation values and for data taken with spherical tips, it finds the range that fits similarly to the spherical model. Any data at lower indentation values is then assigned to the punch model to solve for the effective punch radius, R_p. The algorithm then fits data using the method of minimization of least square error between the model and data to solve for the respective value of E. The accuracy of the algorithm can be verified visually (Fig. 3.5).

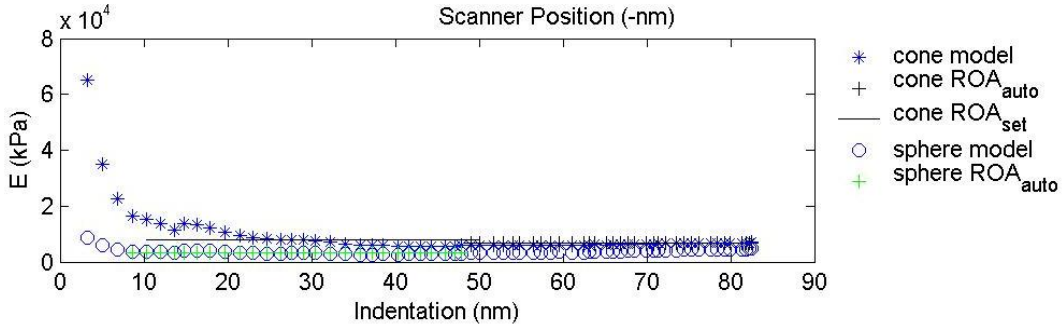

Figure 3.4. Dependence of *E* on indentation, measured with AFM and calculated with the Matlab algorithm

The graph shows discretely calculated values for *E* at each indentation. An increasing trend of *E* is evident at lower indentations, for both the set and automatically determined ROA (ROA_{set} and ROA_{auto}, respectively). The increase is less prominent when analyzed with the spherical model. NOTE: The values of this data are off due to improper calibration, but are shown to illustrate the trend and proof of concept.

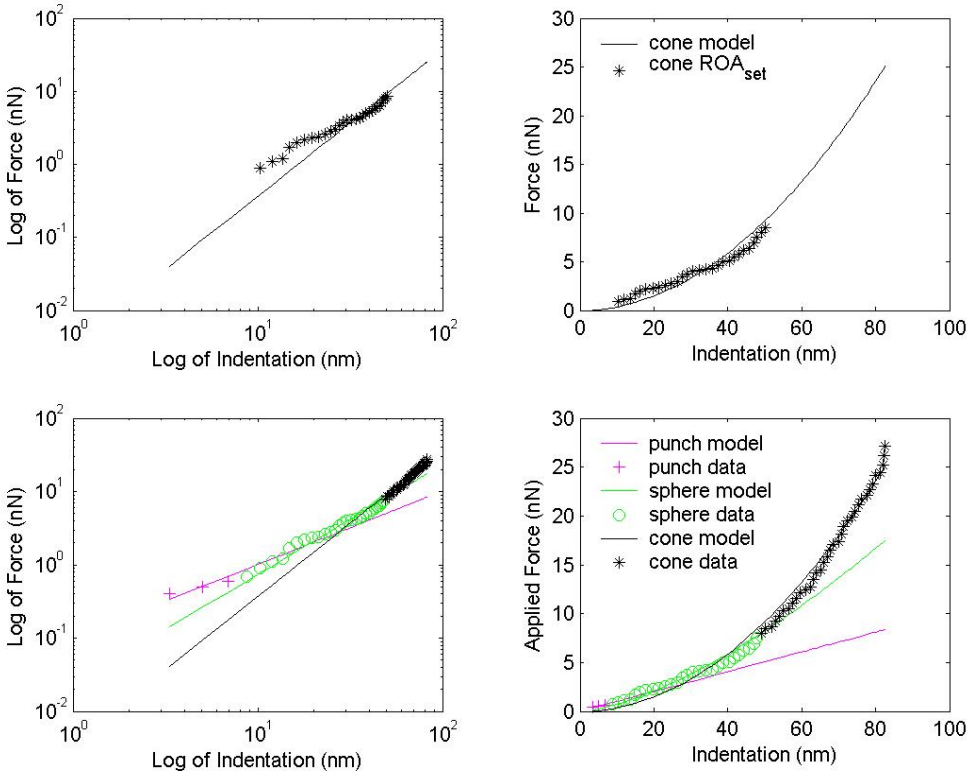

Figure 3.5. Log-log plots of AFM force-indentation profiles fit to conical model by using Matlab algorithm

The upper two plots show the fit using a standard ROA (10-50 nm) while the lower plots show the data from automatically determined ROA, which uses a wider range. The right panels are the force-indentation data and the left panels are the same data in log-log plot. The change in slope, which reflects changes in the probe geometry as a function of indentation, is evident (lower left). Different colors and symbols represent different regimes of probe geometry. NOTE: The values of this data are off due to improper calibration, but are shown to illustrate the trend and proof of concept.

3.6. Probing with spherically-tipped glass microindenters

To address some of the limitations of AFM, a new approach was developed that uses a flexible glass microneedle with a spherical tip to probe the gel. The method is identical to AFM in principle, measuring the indentation of the gel in response to calibrated forces exerted at a spherical tip. However, the position of the probe and the indentation of the material are measured through an optical microscope with a calibrated focusing mechanism in conjunction with a micromanipulator. This allows both qualitative and quantitative measurements to be performed *in situ* on the microscope stage. The method may be viewed as an extension of an approach described by Lee and coworkers (Lee, Leonard et al. 1994), modified to incorporate Hertz contact physics for more reliable measurements. In addition, the method is closely related to the nanoNewton force apparatus described by Davidson and Keller (Davidson and Keller 2007) and to the microindenter method described by Jacot et al. (Jacot, Dianis et al. 2006).

The measurement is performed on a light microscope with a coupled imaging device. It is essential that the focusing mechanism move the objective lens, rather than the stage. For an inverted microscope, the objective lens should have a sufficient working distance to image the surface of the hydrogel, and as high a numerical aperture as possible to give a shallow depth of field. Optimally the microscope should be equipped with a motorized focusing mechanism and fluorescence optics. In addition, the method requires a micropipette puller, a microforge to shape the tip, and a micromanipulator with a fine, precise vertical control. Although specific instrument models are given in the description below, a range of designs by different manufacturers,

in addition to simpler custom-built devices, may be acceptable. The results may be analyzed manually, or using algorithms written in Matlab (Appendix 5).

3.6.a. Preparation and calibration of the spherically-tipped microindenter

A borosilicate glass capillary tube, 1.2 mm OD X 0.9 mm ID (Frederick Haer & Co., Bowdoinham, ME), is first pulled into a thin fiber with a micropipette puller (Vertical Pipette Puller, Model 720, David Kopf Instruments, Tujunga, CA). The heating and pulling settings on the puller are adjusted to create a long taper, about 15-20 mm from the beginning of the taper to the tip. A microforge (MF-900, Narishige Co, Ltd., Tokyo, Japan) is then used to melt the tip into a semi-spherical shape ~40-65 μm in diameter (Figs. 3.6a and 3.6c). Heat is also applied to the region ~150 μm from the tip to create a bend of ~45° (Figs. 3.6b and 3.6c). The spring constant of the microindenter may be varied over a wide range by experimenting with different glass materials, capillary sizes, and taper lengths.

3.6.b. Calibration of the microscope and micromanipulator

The magnification factor of the optical system should be calibrated with a micron standard to obtain the dimension imaged by each pixel, in μm per detector pixel. Vertical movement of the microscope focusing mechanism and the micromanipulator must be calibrated with a precision better than 0.5 μm. Calibration of the microscope focusing knob may be performed by directly measuring a sample of known thickness. Once the

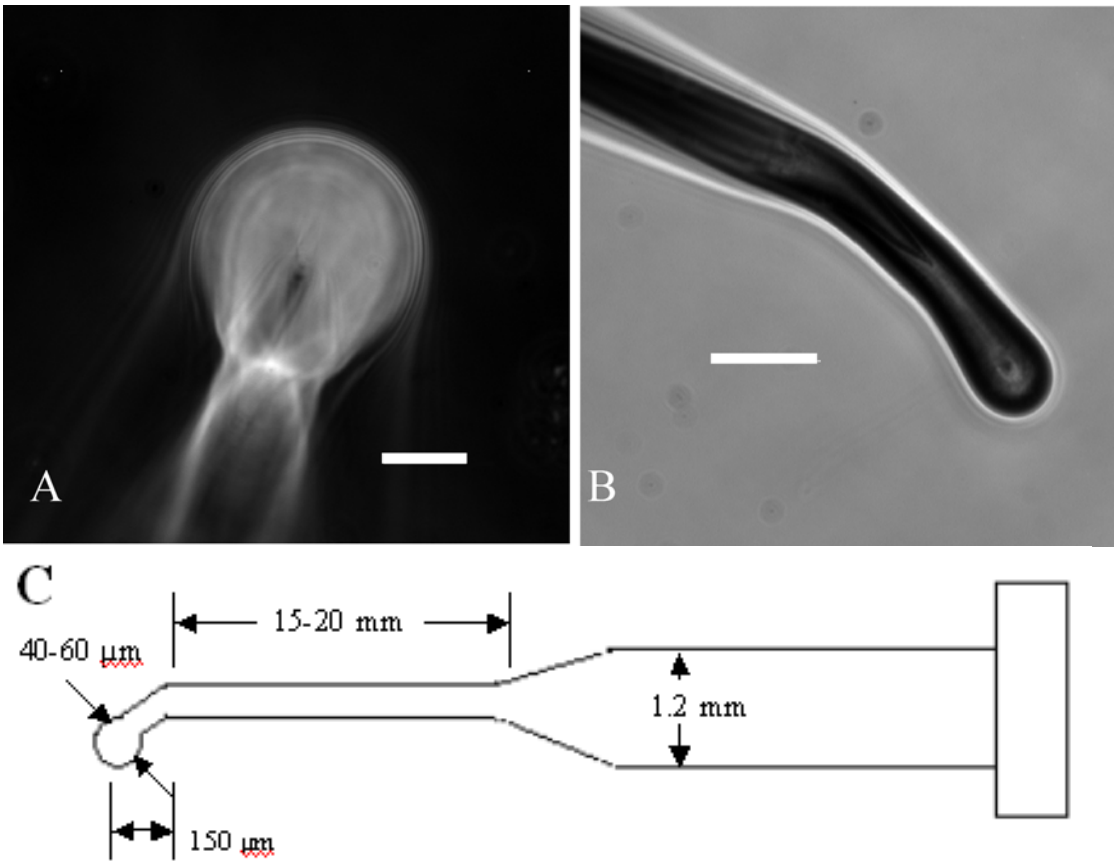

Figure 3.6. Microsphere indenter with a spherical tip

Spherical tip, focused near the bending region (A, scale bar, 25 µm) or from the side (B, scale bar, 100 µm). Dimensions of the indenter (C, not to scale).

focusing knob is calibrated, the movement of the micromanipulator (a Leitz mechanical micromanipulator in this case) may be calibrated as follows. The microscope is first focused on a needle mounted on the micromanipulator. The needle is then moved up by a known number of increments (e.g. 10 divisions on the micromanipulator knob or 45 degree turn), and the image of the needle is brought back into focus, using the calibrated focusing mechanism and while keeping track of the position. These positions on the microscope are converted into the distance per micromanipulator increment.

3.6.c. Characterization and calibration of the microindenter

The first step in microindenter calibration is to obtain the radius, *r*, of the spherical tip, by taking an image and converting the radius in pixels into microns using the magnification factor obtained above. The next step is to collect a reference image of the microindenter, which is the phase-contrast image of the probe as the microscope is focused precisely on the bottom surface of the spherical tip.

The reference image is collected by touching the microindenter against a glass surface sprinkled with 1 μm diameter fluorescent beads (FluoSpheres, Molecular Probes, Eugene, OR). The spherically-tipped microindenter is mounted on the micromanipulator, at the tilting angle to be used for probing the gel and with the tip pointing down (see below), and is lowered slowly until the spherical tip just starts to thrust forward. This is the position where its bottom surface makes initial contact with the glass surface. Under the same magnification and optical conditions as will be used for probing the hydrogel (e.g. with an objective lens of 40x, 0.75 N.A.), the beads on the

glass surface are brought to sharp focus in fluorescence optics. Note that the use of fluorescence optics allows more precise focusing, although the beads can be readily visualized in phase contrast optics. A phase-contrast image of the probe is then recorded. This image must be replaced each time the microindenter is removed and remounted on the micromanipulator, due to possible changes in the approaching angle.

The spring constant of the microindenter is determined by measuring the bending after hanging a number of known weights near the tip. Basically, the microindenter is rotated such that the tip is pointing up, in order to hang a series of weights near the tip. The deflection (d) of the microindenter is measured using the focusing mechanism of the microscope (Fig. 3.7) and the spring constant (k) is determined from Hooke's Law, $f = kd$ (Fig. 3.7), where f is the gravitational force of the weight. The detailed protocol is given below.

1. Prepare a series of weights from thin electric wires of several different sizes, for example by untwisting and separating individual conductors from thin telephone wires. Cut a piece 5-10 cm in length, measure the exact weight, and calculate the weight per mm. To match the stiffness of the microindenter, the linear density of the wire should generally be < 0.1 mg/mm. Cut short pieces ~5 mm in length, and calculate the exact weight forces (f in nN=9.81 x length in mm x density in mg/mm x 1000). Bend the wire into a V shape and bend one of the legs forward to facilitate handling.

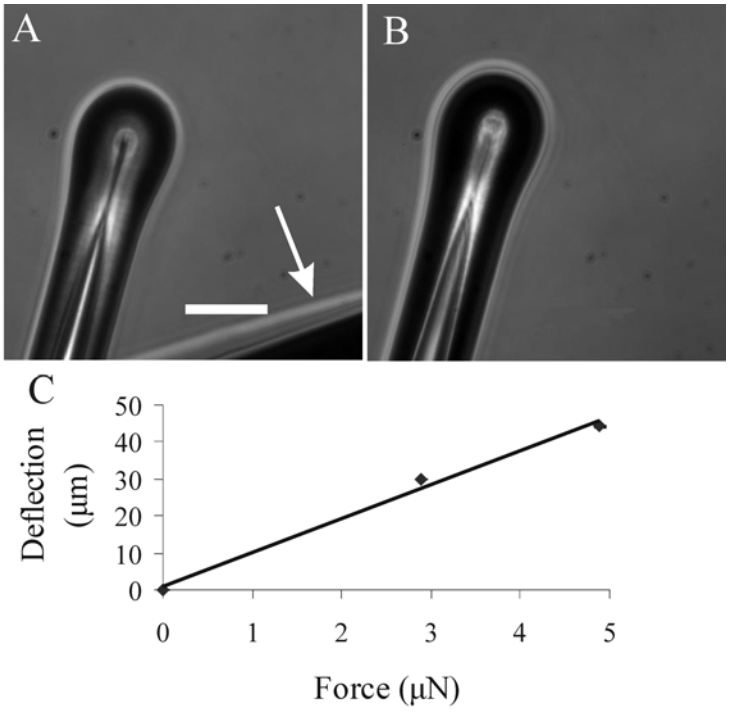

Figure 3.7. Determination of the spring constant of the microsphere indenter.

The probe is deflected under the applied weight (A, arrow), and becomes out of focus upon removal of the weight (B). Scale bar, 50 μm. The amount of deflection is determined from the change in focal plane and is plotted against the applied forces (C, average +/- s.e.m., n = 3 each).

2. Mount the microindenter on the micromanipulator at exactly the angle to be used for measuring the gel. As the sample typically sits on the bottom of a chamber, the angle of the microindenter will be limited by the accessibility to the sample. Therefore, even though this calibration does not require a sample chamber, it would be helpful to place one underneath the microindenter, both to monitor the approaching angle and to catch the calibrating weight that is blown off the microindenter during the calibration.

3. Rotate the microindenter and make sure that its bent tip is pointing up, which should be obvious by focusing the microscope up and down. In addition, no kink should be visible from its lateral profile under the microscope (compare Figs. 3.6A and 3.6B).

4. Center and focus at the tip of the microindenter using low magnification, e.g. 10x.

5. Hang a wire weight on the microindenter with a pair of fine forceps, somewhere not too far from the tip. Gently tap the micromanipulator until the weight slips near the tip and gets caught at the bend. Make sure it does not touch the sample chamber. Monitor the last part of tapping under the microscope.

6. Switch to the magnification to be used for measuring the gel, or as high as the working distance of the lens allows (the tip of the microindenter is several mm above the objective lens, due to the upward bend and to the dangling calibration weight). Bring the tip to focus and record an image (Fig. 3.7A).

7. Tap or blow the weight off the tip of the needle. The tip of the microindenter becomes out of focus (Fig. 3.7B).

8. Adjust the microscope focus to restore the sharp image of the tip of the microindenter (image to match Fig. 3.7A). This step is best performed by collecting a stack of optical sections with a motorized focusing mechanism, and searching for the image in the stack that best matches the weighted image. Using the calibrated focusing knob, determine the distance of vertical movement, *d*.

9. Repeat the measurement with different weights.

10. Plot *d* as a function of *f*. Stiffness, *k*, is determined from the slope of the *f-d* curve (Fig. 3.7C).

3.6.d. Measurement of the indentations of hydrogels in response to forces of the microindenter

Qualitative monitoring of changes in material properties may be carried out simply by imaging the tip of a stationary microindenter, which becomes out of focus when the flexibility changes. This is an excellent tool for developing modulatable materials (Chapter 4), as one can easily visualize the change in stiffness. For quantitative measurement, *E* of the gel is calculated from its indentation as a function of forces exerted by the microindenter using the Hertz equation. To minimize error (discussed later) and to yield results relevant to actual experimental conditions, the sample thickness should be close to that used for plating cells but at least ~50 μm. The following procedure is designed to facilitate consistent measurement of the position of the microindenter, the point of contact with the gel, and the resulting gel indentation.

1. Sprinkle 1 μm fluorescent polystyrene beads (Molecular Probes) on the surface of the gel to be measured to mark the surface for focusing. A low density of beads is

preferred (~2 beads / 100 μm^2 see Fig. 3.9E), as too high a density could interfere with the observation of the tip of the microindenter.

2. Set the microindenter to the angle it was calibrated. Rotate the microindenter such that the tip is pointing down. This is again confirmed by focusing the microscope up and down and by making sure that the lateral profile of the microindenter shows no kinks.

3. Estimate the thickness of the sample to make sure that it is at least 100 μm, which is required for reliable measurements of Young's modulus. This is done by using the calibrated focusing mechanism of the microscope, to focus from scratches or debris on the glass surface to the sprinkled fluorescent beads on the surface of the gel.

4. Use the micromanipulator to lower the microindenter until the tip starts to thrust forward, indicating that the tip is experiencing counter forces as it enters and exerts forces on the gel (Fig. 3.8).

5. Bring the tip further down until the indentation, δ, is ~0.8r where r is the radius of the tip. The indentation may be estimated using the microscope focusing mechanism. Focus the microscope until the phase contrast image of the spherical tip (Fig. 3.9B) matches the reference image collected in section 3.6.c. (Fig. 3.9A). This focuses the microscope on the bottom surface of the spherical tip. This step may best be accomplished by taking serial image sections at < 0.5 μm separation, searching for the best match within the image stack (note the two phase-light dots near the tip), then moving the focal plane to the position where the best match with the reference image is found. The position is referred to as position A_1 (Fig. 3.8).

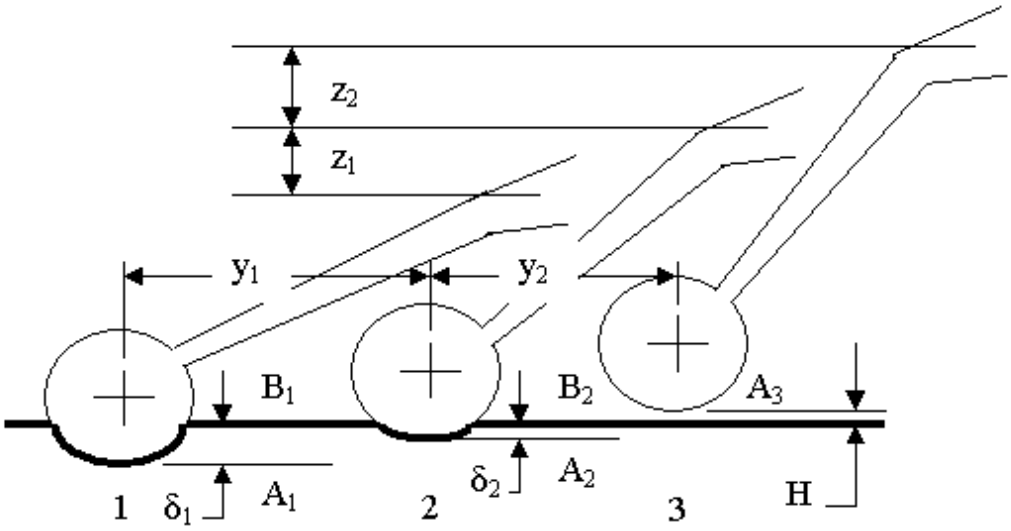

Figure 3.8. Schematic of gel flexibility measurement using microsphere indentation

See text for the definition of various positions marked by letters.

Record a phase contrast image of the spherical tip.

6. Raise the microindenter slightly, such that it is still indenting the sample but at a shallower depth, > 0.3r (Fig. 3.8 and Fig. 3.9C). This position is referred to as position A_2. Record the distance of vertical movement of the micromanipulator (z_1). Do not change the focus of the microscope.

7. Collect the first stack of optical sections, from position A_1 upward to somewhere above the surface of the gel (above the position in Fig. 3.9E), then return the microscope focus to the position A_1. If available, use a combination of transmitted and epi-illumination such that phase contrast and fluorescence are recorded as superimposed images.

8. Raise the tip of the microindenter such that it is above but not too far from the surface of the sample (Fig. 3.8 and Fig. 3.9F). This position is referred to as the off position or position A_3. Record the distance of vertical movement of the micromanipulator, z_2.

9. Collect a second stack of optical sections, from position A_1 upward to somewhere above the spherical tip. If available, use a combination of transmitted and epi-illumination such that phase contrast and fluorescence are recorded as superimposed images.

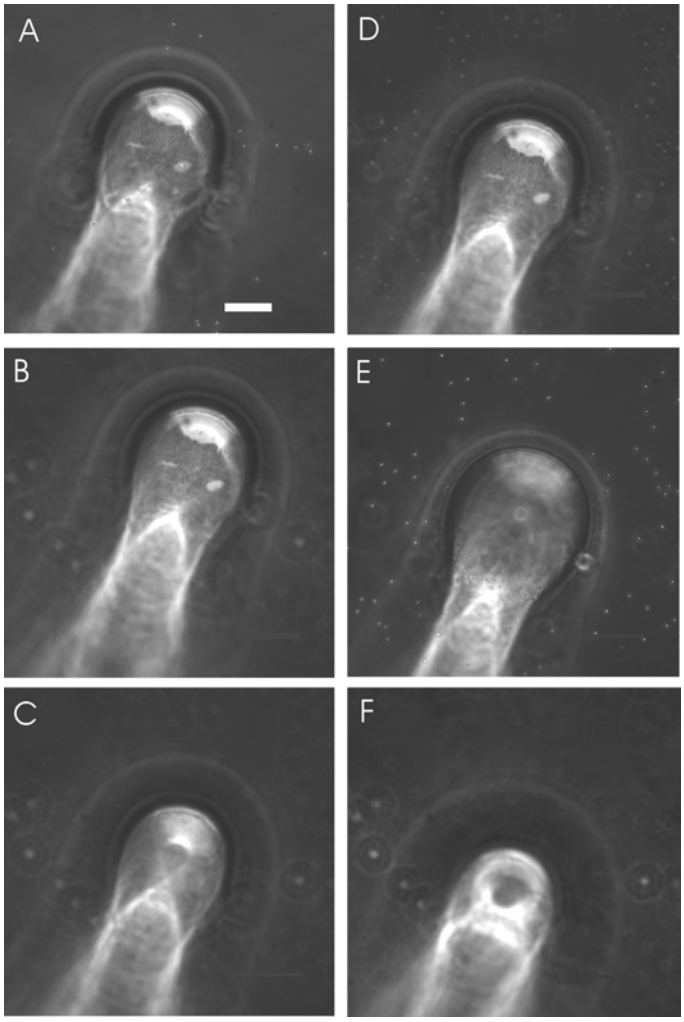

Figure 3.9. Example images obtained during microsphere indentation

Upon initial indentation into a polyacrylamide gel, the image of the tip (B) is matched with the reference image (A), to make sure that the microscope is focusing on the bottom surface of the tip. The microindenter is then raised to a slightly higher position while remaining in contact with the sample (C). The new position of the tip and the gel surface are determined by serial optical sectioning and looking for an image that matches the reference image (D), and an image that shows sharply focused surface beads (E), respectively. The microscope focus is then returned to the point of initial indentation while the probe is raised off the sample surface (F). Serial optical sectioning is again performed to determine the position of the gel surface and the spherical tip off the surface. Scale bar, 25 μm.

10. In both stacks of optical sections, look for the section where the beads on the surface in the periphery of the image (i.e. away from the point of indentation) are in sharp focus (Fig. 3.9E). Calculate the corresponding position, which is referred to as the surface position or positions B_1 and B_2 respectively (which theoretically should be at the same position, though B_2 is slightly more reliable due to the lack of indentation).

11. Search for the optical section in the first stack where the image of the tip matches the reference image (Fig. 3.9A). This marks the position of A_2. Distances B_1 - A_1 and B_2 - A_2 are the corresponding sample indentations, δ_1 and δ_2 (Fig. 3.8).

12. Search for the optical section in the second stack where the image of the tip matches the reference image. This marks the position of A_3, where the spherical tip is above the gel by a distance of H.

13. According to Fig. 3.8, the difference between $z_1 + z_2 - H$ and δ_1 is the net vertical deflection d_1 of the microindenter at position A_1, and the difference between $z_2 - H$ and δ_2 is the net vertical deflection d_2 of the microindenter at position A_2. However, direct measurement of H is prone to error due to surface interactions between the needle and the gel. A more reproducible approach is to plot the net deformation of the tip against the height of the micromanipulator, ($z_1 + z_2$, $((A_3 - A_1)^2 + y_1^2)^{1/2}$) and ($z_2$, $(A_3 - A_2)^2 + y_2^2)^{1/2}$), where y is any lateral deflection of the microindenter tip (Fig. 3.8). If $H = 0$, the line connecting these two points should pass through the origin. Therefore, its x-intercept is used as the estimate of H (Fig. 3.10). It is important that the final position of the tip be very close to, but not touching, the surface. This

position should yield a nearly linear relationship between net tip deformation and applied force, which is a condition required for the analysis.

14. Using the value of k obtained from the calibration curve obtained in section 3.6.c., convert d_1 and d_2 to forces f_1 and f_2. This generates two pairs of force-indentation relationships, f_1 and f_2, and the corresponding indentations δ_1 and δ_2.

15. Repeat the measurements at several different locations of the gel.

16. The microindenter may be stored and used many times. Accumulated beads on the surface of the tip should be removed as much as possible by gentle sonication in a detergent solution, since they interfere with phase contrast imaging of the tip.

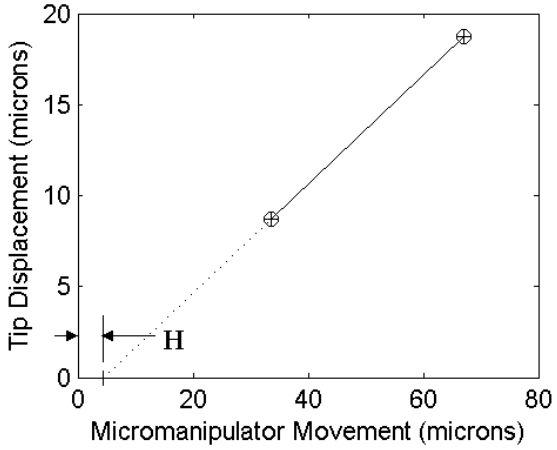

Figure 3.10. Contact point estimation in microsphere indentation

Data are taken on a polyacrylamide gel with 8% acrylamide and 0.08% bis-acrylamide.

3.6.e. Data analysis to calculate Young's modulus

Each set of f_1, δ_1 and f_2, δ_2 is first checked for consistency. The Young's modulus, E, is calculated for each pair of f, δ using the Hertz equation for a rigid sphere (Eq. 4, Fig. 3.11), assuming a Poisson's ratio of 0.45 for polyacrylamide (Engler, Bacakova et al. 2004). The resulting two values of E should agree with each other. A threshold difference is set as 20%, and data exceeding this criterion are removed. Inconsistency is typically due to one of the indentations being too deep or shallow (discussed in following section).

Use of Hertz contact mechanics assumes an infinitely thick sample. In addition, to avoid stress stiffening from the underlying glass substrate, the sample thickness should be substantially greater than the vertical strain induced by indentation, which is verified experimentally (Dimitriadis, Horkay et al. 2002). Note that strain, ε is a function of contact radius, a (Eq. 8), which may in turn be expressed as a function of the indenting force and the property of the sample, after incorporating Hertz equation for spherical probes (Eq. 9):

$$\varepsilon = \frac{2}{\pi}\frac{a}{R}\frac{1}{(1-\nu)} \tag{8}$$

$$a = \left[\frac{3FR}{4}\frac{\left(1-\nu^2\right)}{E}\right]^{1/3} \tag{9}.$$

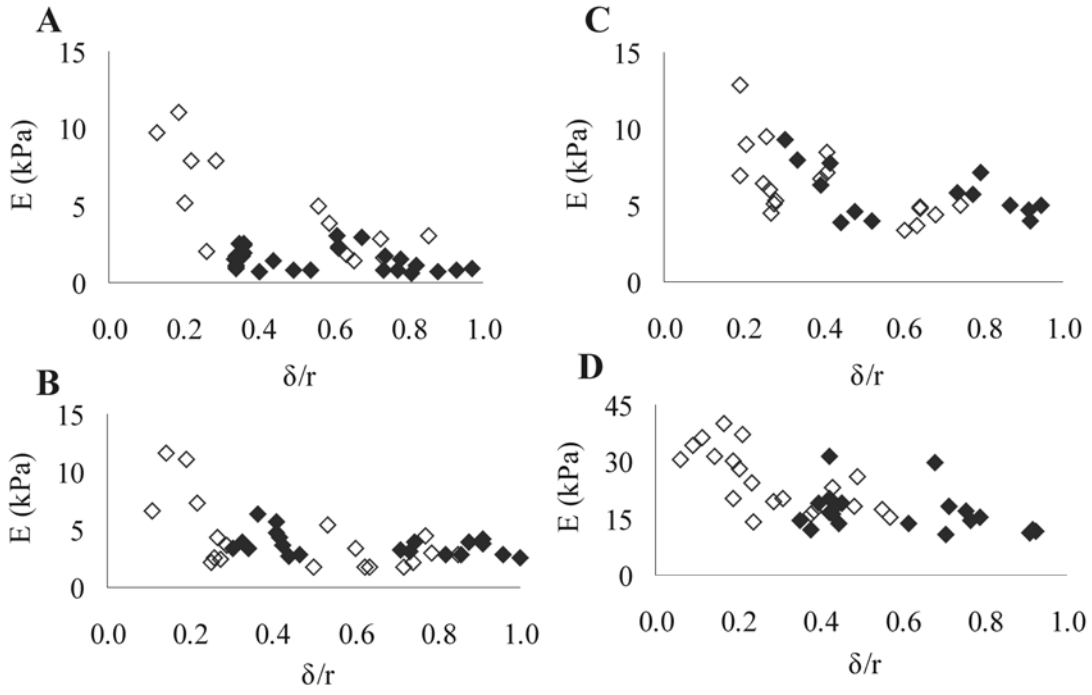

Figure 3.11. Young's moduli of polyacrylamide samples calculated from discrete force-indentation data obtained with microsphere indentation

The points that meet the selection criteria as described in the text are indicated by filled dots and those rejected by open dots (two dots per probed location representing the two discretely calculated values of *E*). Before selection the data show an upward trend of *E* at lower indentations. The polyacrylamide gels are made from 5% and 0.025% (A), 5% and 0.06% (B), 5% and 0.1% (C), and 8% and 0.08% (D) acrylamide and bis-acrylamide respectively.

3.6.f. Sources of uncertainty and error with microsphere indentation

As with any method, there are several sources of uncertainty. Values for Poisson's ratio of polyacrylamide gels commonly seen in the literature range between 0.3 and 0.5 and thus contribute the largest relative uncertainty. I chose to use a value of 0.45, as this value yields the best fit between E values obtained with macroscopic and microscopic testing (Engler, Bacakova et al. 2004).

At small indentations, significant systematic error occurs. For example, experimental measurements indicated larger measured contact areas than those predicted by the model at low indentations (Fessler and Ollerton 1957; Johnson 1985), which leads to a value of E that is several times higher than those measured at higher indentations. There may be additional sources of error at small δ, e.g., from surface interactions between the probe and the sample. An upward trend in E at low δ is indeed observed in both the present measurement (Fig. 3.11), and in several studies with AFM (Fig. 3.4) (Dimitriadis, Horkay et al. 2002; Richert, Engler et al. 2004), where the values at low indentation depths were found to be 2-3 times higher than those at higher indentation depths. This systematic error may also explain the higher values of E obtained with the bead indentation measurement (Lo, Wang et al. 2000; Frey, Engler et al. 2007), particularly for stiff gels where the indentation may be very small compared with the radius of the bead.

A second significant source of error is associated with the measurement of microindenter vertical position based on visual inspection of images. Although the field

depth for a dry lens is typically several microns, the vertical position of the microindenter may be determined to an accuracy better than 1.0 μm using a stack of optical sections collected at ~0.25 μm per slice. However, visual accuracy is limited and this can lead to greater error at low indentations. The accuracy may be improved by replacing visual comparison with a cross-correlation-based algorithm for matching images.

Other sources of error include mechanical movements and the calibration of microscope focusing mechanism and the micromanipulator (dial reading), the weight of the calibration wire, and the deviation of the tip from a perfect spherical shape. The relative uncertainties for the measurement of microindenter spring constant, deflection, gel indentation, and radius are estimated to be around 13%, 11%, 6%, and 1%, respectively, as calculated previously (see section 3.4.d). The net relative uncertainty for E is approximately 41% (18% contributed by the method itself), which is within 5% of the estimate of the uncertainty for AFM measurements (Guo, Frey et al. 2006).

Finally, there are also two assumptions that could lead to errors. The method is based on the assumption that the spherical tip glides freely (slips) on the gel surface as it applies forces, as obstruction in axial movements affects the bending behavior of the probe. Judging from the vertical and lateral distribution of beads on the surface, this obstruction appears to occur with very soft gels (< 1 kPa), where the surface undergoes complex shape changes as the tip digs into the gel. A similar problem may affect AFM. Another assumption of this method is that all measurements are static since the time required for measurements is such that stress relaxation, if the material is viscoelastic, has likely already occurred.

3.7. Results

The retraction portion of the AFM force-indentation profiles obtained on stiff and soft PA gels was used for analysis (Burnham and Colton 1989). These data were converted to logarithmic form, then fit using a manually determined contact point and a linear least squares method in Excel Solver to yield values for E. Analysis using a standard ROA of 10-50 nm yielded values of E of 7.69 +/- 2.85 kPa for stiff substrates with 0.1% bis-acrylamide and 2.68 +/- 0.99 kPa for soft substrates, where the range of values represents the estimated uncertainty.

The Matlab algorithm was validated as follows. The algorithm, which determines the contact point automatically, yielded a 10% reduction in E compared with the value obtained above, both using a fixed ROA of 10-50 nm (Table 2.1), while a reduction of 17% was obtained using all the values in the data set (including those previously removed as visual "poor fits", Table 2.1). The results did not vary much using fixed or automatic ROAs for data taken with spherical tips, but varied by up to 15% for data taken with conical tips (Fig. 3.4).

The values obtained with the microsphere indentation technique were comparable to those obtained with AFM (Table 2.1 and Fig. 12). To reduce the error associated with the overestimation of E at lower indentations (see Fig. 3.11), the calculation of E for microsphere indentation was performed with $\delta_1 < r$ and $\delta_2 > 0.3r$. Moreover, the sample should be thick enough to avoid potential stiffening artifacts from proximity to the underlying glass substrate. Although $\delta < 0.1t$ where t is sample thickness is typical, the maximal tolerable strain in relation to thickness may be determined experimentally

particularly with large spheres. For each measurement, the vertical strain did not exceed ~60% of the material thickness (with ~40% or less the typical value) and therefore, no thin film corrections were required. The values of *E* turned out to be relatively consistent over a wide range of indentations (Fig. 3.11), and were averaged to obtain the final value (Fig. 3.12). The results with several polyacrylamide gels of different stiffness, as controlled by the concentrations of acrylamide/bis-acrylamide, are shown in Figure 3.12. Using three different probes with tip radii between 29.7 and 32.9 μm, spring constants between 0.10 and 0.14 nN/nm, and gels ~150 μm in thickness, the values of *E* were in excellent agreement with those obtained with AFM as reported in the literature (Engler, Bacakova et al. 2004; Jacot, Dianis et al. 2006) and as measured independently (Fig. 12 and Table 2.1) (Guo et al., 2006).

Table 2.1. Comparison of stiffness values obtained with AFM and microsphere indentation

Values obtained with AFM using a standard range of analysis (ROA) of 10-50 nm (Excel column, (Guo, Frey et al. 2006)) are comparable to those obtained with the Matlab algorithm for both the standard ROA (10-50 nm) and for an ROA that is generated automatically (automatic). Data was obtained on gels made from 5% total acrylamide and 0.1% bis-acrylamide. Similar results were obtained using the microsphere indentation method (MSI).

ROA	AFM (Excel)	AFM (Matlab Algorithm)	MSI
10-50 nm	7.69+/-1.72	6.39+/-1.26	-
Automatic	-	6.29+/-1.55	-
-	-	-	5.79+/-0.56
n	15	18	7

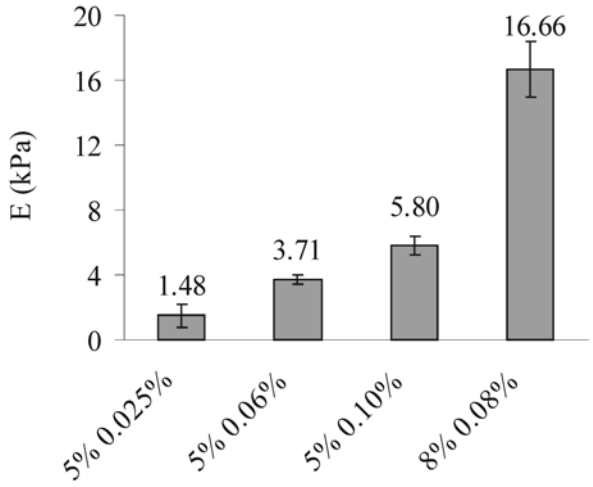

Figure 3.12. Young's moduli for various polyacrylamide gels obtained with the microsphere indentation technique

Values are average +/- s.e.m., n = 10, 7, 10, and 13 taken at different locations on multiple gels, respectively, including all the values that meet the selection criteria. All unpaired t-test *p*-values between adjacent values are < 0.002. Numbers on the x-axis indicate the concentrations (w/v) of acrylamide and bis-acrylamide.

3.8. Discussion

With the realization of the importance of mechanical signals, cell biological studies are increasingly performed on polymer-based substrates in an effort to control the rigidity and to elucidate the mechanisms that regulate the complex cell behavior. The quality of these studies is directly affected by proper characterization of the mechanical properties of these substrates. Optimal choice of the method should take into consideration the requirements of the application, the acceptable uncertainty, as well as practical factors such as cost and equipment availability.

While AFM represents a highly reliable and versatile approach, it is also costly and the analysis complicated. This chapter shows that the analysis of AFM data may be performed with a much simpler approach, using the linear log-log relationship to fit the data to the respective models. The use of log-log plots can be used to more accurately determine the contact point for the individual contact regimes of both spherical and conical tips, as well as the optimal range for fitting the data to the model. Use of the Matlab algorithm provides a much more efficient and objective means of obtaining the material properties of samples. Although the values obtained using automatically determined ROA did not vary substantially from those obtained using fixed ROA, this becomes more important with conical probes that have more a complicated geometry.

Indentation with microspheres is easier and cheaper than AFM, yet reliable and versatile. It may be further improved by incorporating precise (e.g. piezo-electric) and automated positioning of the tip. The use of large indentations, however, may be called

into questions, as the use of the Hertz model is generally considered valid only for small indentations, due to behavior other than linear elasticity at greater indentation depths. However, macroscopic testing of polyacrylamide gels indicated that this limit may be overly conservative (Engler, Richert et al. 2004). AFM data with spherical tips also found good agreement with the Hertz model at indentations up to r (Engler, Richert et al. 2004). A similar conclusion was reached using conical tips, which involve higher strains that exceed this limit even at very low forces (Dimitriadis, Horkay et al. 2002; Engler, Bacakova et al. 2004). Most notably, Yoffe found that the Hertz model is valid to within 1% error for large indentations at least up to a/r~0.8, where $a^2 = \delta r$ and a is the radius of the contact area, or δ~0.64r for materials with a high Poisson's ratio (0.40; (Yoffe 1984). For the present measurements, Yoffe's correction for a material of $\nu = 0.40$ amounts to a difference of less than 2% in the value of E. These results suggest that indentations up to the radius of the microindenter may be applied in the present approach in conjunction with an uncorrected Hertz model for thick elastic materials that are nearly incompressible (high ν, e.g. > 0.4).

There are many advantages to the microsphere indentation method. It is straightforward and the analysis is simple. The materials and equipment are inexpensive compared to AFM, and are often available for other purposes. Once calibrated and if handled carefully, the microsphere indenter can be used repeatedly, in contrast to the much shorter longevity of expensive AFM probes because of cantilever damage or corrosion of the reflective coating. Although the build-up of beads on the surface after repeated use can impair visualization of the tip necessary for accurate measurements, the

life of a microsphere indenter can be extended greatly by cleaning after each use. This method also appears to be less sensitive to environmental factors than the AFM, as air currents and minimal amounts of vibration do not seem to significantly affect the outcome. This method can also test sticky samples that could otherwise not be amenable with AFM due to its limited vertical scanner range necessary to pull the tip free from adhesive samples.

One of the most significant advantages of this method is its ability to test substrates on a microscope, possibly in conjunction with the observations of cells. This is particularly useful for testing non-homogenous substrates, and modulatable substrates that stiffen or soften in response to local manipulations (discussed in the next chapter). Even when used without quantification, it provides a convenient tool for assessing the mechanical properties of substrates during material development.

CHAPTER 4. A PHOTO-MODULATABLE MATERIAL FOR PROBING CELLULAR RESPONSES TO SUBSTRATE RIGIDITY

4.1. Abstract

Recent studies indicate that extracellular mechanical properties, including rigidity, profoundly affect cellular morphology, growth, migration, and differentiation (Choquet, Felsenfeld et al. 1997; Pelham and Wang 1997; Lo, Wang et al. 2000; Wang, Dembo et al. 2000; Gray, Tien et al. 2003; Engler, Griffin et al. 2004; Discher, Janmey et al. 2005; Georges and Janmey 2005). However, most studies involving rigidity sensing compare cells on separate substrates of fixed stiffness. To allow spatial or temporal manipulation of mechanical properties, I developed a modulatable hydrogel by reacting linear polyacrylamide (PA) with a photosensitive crosslinker. This material allows UV-mediated control of rigidity, softening by 20-30% upon irradiation at a dose tolerated by live cells. Global UV irradiation induces an immediate recoiling of cultured fibroblasts and a reduced spread area at steady state. Furthermore, localized softening of the posterior substratum causes no apparent effect, while softening of the anterior substratum elicits pronounced retraction, indicating that rigidity sensing is localized to the frontal region. This type of material allows precise spatial and temporal control of mechanical signals for both basic research and regenerative medicine.

4.2. Introduction

Mechanosensing is believed to affect cancerous invasion, wound healing, stem cell differentiation, and many other physiological and pathological processes (Lo, Wang et al. 2000; Wozniak, Desai et al. 2003; Huang and Ingber 2005; Paszek, Zahir et al. 2005; Georges, Miller et al. 2006; Guo, Frey et al. 2006; Engler, Sweeney et al. 2007; Kass, Erler et al. 2007). The rigidity of adhesive substrates plays a particularly important role in cell regulation (Wang, Dembo et al. 2000; Discher, Janmey et al. 2005; Ingber 2008). Due to their favorable optical and tunable elastic properties, polyacrylamide (PA) gels have been used widely as adhesive substrates for manipulating mechanical cues (Pelham and Wang 1997). For example, stiff PA gels promote spreading and scattering of adherent cells (Engler, Bacakova et al. 2004; Georges and Janmey 2005; Guo, Frey et al. 2006), while soft PA gels promote soft tissue differentiation and tissue-like cell-cell associations (Engler, Bacakova et al. 2004; Georges and Janmey 2005; Paszek, Zahir et al. 2005; Georges, Miller et al. 2006; Guo, Frey et al. 2006; Kass, Erler et al. 2007). In addition, adherent cells migrate preferentially toward stiffer regions (Lo, Wang et al. 2000; Gray, Tien et al. 2003), a process known as durotaxis that may play a role in guiding cell migration in conjunction with chemical signals.

Most applications of PA gels in cell mechanics have involved substrates of constant rigidity (Pelham and Wang 1997), which limits the ability to study dynamic cellular responses. The large variability among cells further adds to the difficulty. These limitations provide the motivation to create gels with a rigidity that can be modulated under conditions compatible with live cells. In particular, light-induced modulation

allows a high degree of versatility while avoiding direct mechanical perturbations or cellular displacements that may confound the effects.

While gels that stiffen upon UV illumination have been reported (Bourke, Al-Khalili et al. 2003), the typical use of photo-activated free radical generators raises serious concerns of toxic side effects to live cells. Therefore, I chose to develop a substratum that softens upon UV illumination, by crosslinking polymers with a photocleavable cross-linking reagent. Application of this material led to the discovery that cellular mechanosensing of stiffness is localized to the anterior region.

4.3. Methods

Unless otherwise specified, all chemicals were purchased from Sigma.

4.3.a. Preparation of UV-softening substrates and control PA gels

Linear polyacrylamide (MW 600,000-1,000,000, 10% in water; Polysciences, Warrington, PA) was dried in a Savant DNA 110 Speed Vac (Global Medical Instrumentation, Inc.; Ramsey, MN) and resuspended in hydrazine hydrate (24-26%) at a concentration of 26.4 mg/ml (Freeman 1987). Following incubation for 3 hr at 50ºC with frequent vortexing, the solution was cooled on ice and mixed with 3 volumes of cold methanol to precipitate the PA, which was collected by centrifugation. After several rinses with methanol, the pellet of polyacrylamide acyl hydrazide (PAAH) was dried with nitrogen and stored desiccated at 4°C.

4-bromomethyl-3-nitrobenzoic acid (BNBA) was handled under reduced illumination throughout the procedure. A fresh solution of 20% (w/v) BNBA in dimethyl

sulfoxide was added to 45 mg/ml of PAAH in 10 mM boric acid (pH 12.5), at a volume ratio of 0.072 (Marriott and Ottl 1998). After stirring for 2 hr at room temperature, the solution was mixed with an equal volume of 100 mM 2-(N morpholino) ethane sulfonic acid (MES, pH 6.0; Research Organics, Cleveland, OH), and additional dry PAAH at a weight of 0.5 relative to the initial weight. The solution was degassed for 20 min to avoid the formation of bubbles in subsequent steps, then mixed with 0.42 M 1-ethyl-3-(3-dimethylaminopropyl) carbodiimide HCl (EDC) at a volume ratio of 21:4. The mixture was immediately plated onto glutaraldehyde activated coverslips (Alpin and Hughes 1981), and weighted with a 7/8" diameter x 1" stainless steel cylinder atop a 7/8" diameter thin Teflon disk. The crosslinking reaction was allowed to proceed for 30 min at room temperature to form a thin sheet. The gel was then soaked in 4-(2-hydroxyethyl)-1-piperazineethanesulfonic acid (HEPES; pH 8.5) for 10 min and the stainless steel cylinder and Teflon sheet carefully removed. The gel was then washed extensively with phosphate buffer solution (PBS). The surface of the gel was then covered with a thin cell-adhesive layer of PA gel (Rajagopalan, Marganski et al. 2004). First, 200 µl acrylamide (40%; BioRad, Hercules, CA), 20 µl bis-acrylamide (2%, BioRad), 100 µl 10X PBS, 2 µl 1,2-di-(dimethylamino)ethane (TEMED; EMD, Gibbstown, NJ), and 455 µl distilled water were mixed and pH adjusted to 7.2-7.6. After addition of 50 µg FN (1 mg/ml), 1 µl of acrylic acid N-hydroxy succinimide ester (10 mg/ml), and 10 µl fluorescent beads (0.5 µm diameter; Polysciences, 19507), the volume was adjusted to 995 µl with distilled water. The solution was degassed for 20 min, and the polymerization initiated by adding 5 µl of ammonium persulfate (BioRad) at 100 mg/ml.

The solution was layered immediately atop the UV-sensitive gel (10 µl /substratum of 7/8" diameter), and covered as before using the Teflon disk and weight.

Substrates may be stored in the dark at 4°C in PBS for up to two weeks. Prior to experiments, the substrates were incubated with complete media for 45 min. Control PA substrates were prepared by placing 42 µl of the polymerizing solution for the top layer directly onto activated coverslips, as for the photosensitive solution, omitting the bottom UV-sensitive layer.

4.3.b. Measurement of crosslinking density

The extent of modification of PAAH by BNBA, in mmol BNBA/g PAAH, was determined by spectrophotometry (Ultrospec 2100 Pro, Biochrom Ltd., Cambridge, UK). Following the 2 hr reaction of BNBA with PAAH and neutralization with MES as described above, solutions were dialyzed extensively against 10 mM boric acid, pH 12.5, then measured for absorbance at 350 nm in triplicates. The average of these values were then compared against a standard curve obtained from measuring known concentrations of BNBA in the same buffer (n = 9 from 3 preparations).

4.3.c. UV light source and power measurement

To perform proof of principle experiments regarding softening, pre-illuminated substrates were exposed for 3 min at a distance of 2-1/4 in from two 15 W UVB bulbs. Substrates were irradiated using a 105W mercury arc lamp (HBO 105; Carl Zeiss, Thornwood, NY) filtered with a 365 nm interference filter and a BG38 heat filter. The illumination power was measured with a power meter (LaserMate-Q A/D, Coherent, Inc.)

at the output of the objective lens (originally 0.122 mW for whole cell illumination experiments). The area of global illumination (with the diaphragm completely open) could not be measured directly, and instead, was estimated from the area of illumination for localized exposure (diaphragm closed) assuming a constant energy density. First, the power was measured with the diaphragm open and then closed (see Table 4.1). The area could also be determined by measuring the diameter of the field with the diaphragm closed on an image taken of a fluorescent solution. Using a constant exposure time and assuming a constant energy density (Eq. 10) under the two conditions, the area of global illumination was then estimated. This area was used to calculate the energy density used in the experiments (2.3 J/cm^2).

$$EnergyDensity = \frac{(Power)(Time)}{Area} \qquad (10)$$

A constant energy density of 2.3 J/cm^2 was maintained by adusting the exposure time (originally 15 sec) for each experiment. For the sequential illumination experiment to determine the dose responsiveness of the substrate, the substrates were irradiated using one-third of the maximum illumination in three successive increments.

Measured Values	40 X	
diaphragm condition	closed	open
Power (mW)	0.004	0.101
Diameter (pixels)	198	-
Diameter (microns)	63.0	-
Area (sq microns)	3112	-

Calculated Values	40 X	
diaphragm condition	closed	open
Area (sq microns)	-	78581
Diameter (microns)	-	316.4

40 X, open	
Power (mW)	0.122
Time (s)	15
Area (sq microns)	78581
Energy density (J/cm^2)	2.3

Table 4.1. Power measurements and calculations

Measurements made the diaphragm closed at 40x magnification were used to determine equivalent area of exposure for conditions when diaphragm was completely open (and could not be accurately measured) assuming a constant energy density (and time of exposure). The estimated area of exposure was then used to calculate the energy density for illumination in the experiments.

4.3.d. Measurements of gel and observations of cell responses

The initial rigidity of the gel was measured with a calibrated glass microsphere indenter (Chapter 3) (Jacot, Dianis et al. 2006; Frey, Engler et al. 2007). To measure the change in rigidity after successive exposure, the probe was repositioned such that a defined force (where $F_1 = F_2$) was applied on the gel surface. Then the substrate was then exposed in successive pulses of UV as described above, and the change in indentation was measured after each exposure in 1 min intervals for 3 min. The relative change in stiffness was then calculated from substitution into the Hertz equation (Eq. 4), with $F_1 = F_2$ (Eq. 11)

$$\frac{E_2}{E_1} = \left(\frac{\delta_1}{\delta_2} \right)^{3/2} \qquad (11).$$

NIH 3T3 fibroblasts were cultured in DMEM (Invitrogen, Carlsbad, CA) containing 10% donor calf serum (Hyclone, Logan, UT) and 100 units/ml penicillin, 100 µg/ml streptomycin and 4 mM supplemental glutamine (Invitrogen) for 12-36 hr before experiments. Cellular responses to substrate softening were studied by irradiating cells plated on UV-softening gels and compared to those on control PA. Cells were imaged with phase contrast optics under red illumination (to avoid pre-exposure using multi-wavelength light) on an inverted microscope with a custom stage incubator (Axiovert-S100, Zeiss, Thornwood, NY) using a 10x (Achromat, N.A. 0.25) or 40x (Plan-NeoFluar, N.A. 0.75) objective lens for either 2 hr or 20 min before UV illumination (for global and localized irradiation, respectively). All experiments were performed with motile

interphase cells that were well separated from one another. To distinguish illumination-induced retraction from spontaneous retraction and to eliminate mitotic cells, cells showing a decreasing trend in area prior to UV illumination were rejected (in cells on both UV-softening gels and control PA gels). After UV illumination, the cells were imaged for 2 hr. The spread area was computed, normalized, and averaged in 8 min intervals to suppress noise, using custom software.

4.3.e. Statistical analysis

Values before and after illumination (area, n = 24 from 8 cells; speed and persistence, n = 8) were compared using paired student's t-tests performed with GraphPad© software after normality was verified using the Lillifors test. All data are represented as mean +/- s.e.m.

4.4. Results

4.4.a. Preparation of a UV-modulatable substrate

A gel was formed by crosslinking functionalized PA with a UV-cleavable agent. Linear PA was first activated with hydrazine hydrate to create polyacrylamide acryl hydrate (PAAH) with reactive amine groups (Fig. 4.1a) (Freeman 1987). The linear polymers were then crosslinked with BNBA (Marriott and Ottl 1998). The bromomethyl group of BNBA undergoes nucleophilic reaction with the reactive amines on PAAH at elevated pH. The carboxyl group on BNBA was then linked with the remaining amines using EDC, creating a gel (Fig. 4.1a). By systematically varying the concentrations of

reactants, I created gels with an initial rigidity of ~7 kPa, where adherent fibroblasts were found to be highly sensitive to changes in substrate rigidity (Solon, Levental et al. 2007). This material contained on average ~ 0.08 mmol nitrobenzyl group /g PAAH.

4.4.b. Coating with fibronectin for cell adhesion

Since crosslinked PAAH, like PA, is poorly adhesive for cells (Fig. 4.1a), its surface was further coated with a thin layer of FN-conjugated PA, prepared by copolymerizing acrylamide, bis-acrylamide, and an NHS-ester derivative of acrylamide in the presence of FN (Fig. 4.1b) (Rajagopalan, Marganski et al. 2004). This versatile coating process allows adhesions and mechanosensing to be targeted at specific matrix proteins, independent of the underlying UV-sensitive gel. In addition, it separates the cells from any byproducts of photolysis.

4.4.c. Softening of substrate upon UV irradiation

The nitrobenzyl group of BNBA is prone to efficient photolysis with 365 nm UV light. To probe the changes in rigidity upon irradiation, a microsphere microindenter mounted on a micromanipulator was used (Jacot, Dianis et al. 2006; Frey, Engler et al. 2007) (Figs. 4.1c and 4.1d). Softening of the gel caused the probe to sink into the gel and beads embedded in the gel to jump out of focus (Fig. 4.1c). Control PA gels, prepared with only the photo-insensitive FN-containing gel, were insensitive to UV exposure (E = 11.1 +/- 1.0 kPa, n = 10).

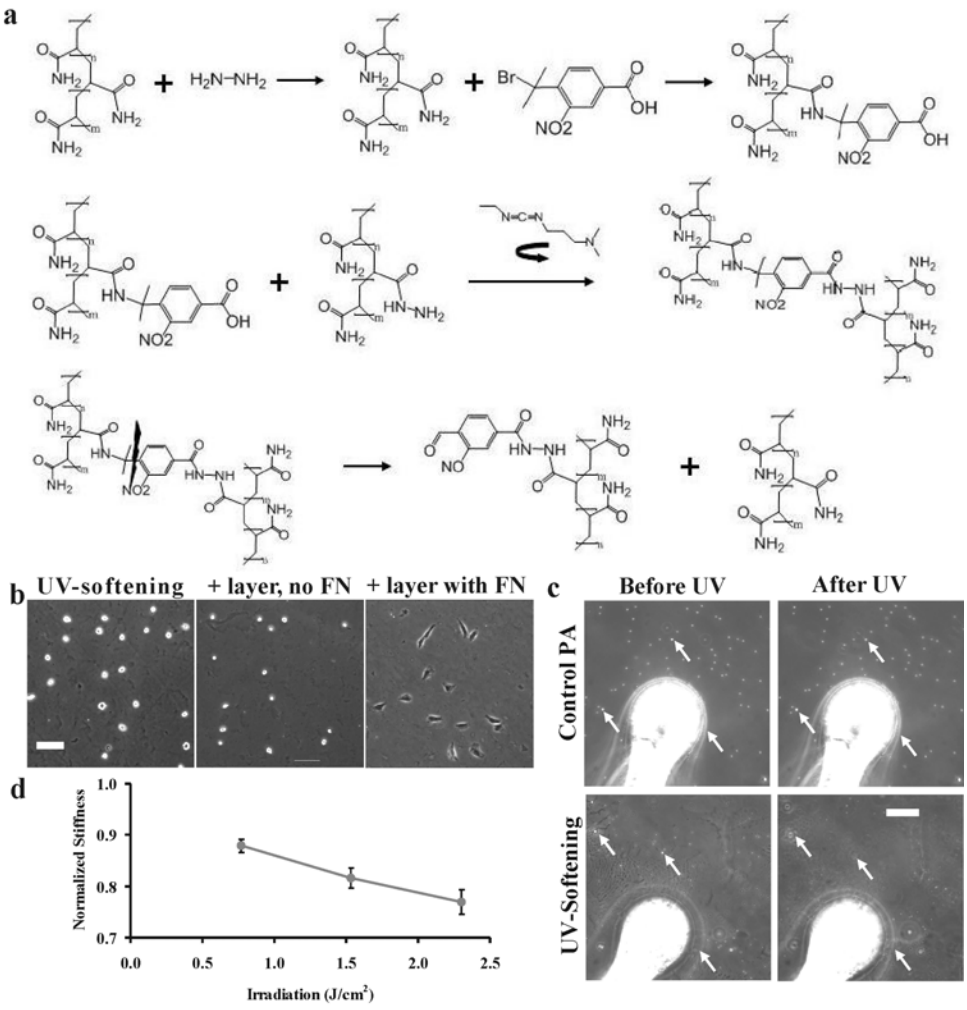

Figure 4.1. The strategy to create a UV-softening, cell adhesive gels

Linear polyacrylamide is functionalized with hydrazine hydrate followed by a UV-cleavable reagent BNBA (**a**, upper reactions). Subsequent crosslinking of the polymers with EDC creates a gel (**a**, middle reaction). UV exposure cleaves near the nitrophenyl group and causes the gel to soften (**a**, lower reaction). While the gel is non-adhesive to cells (**b**, left panel), coating with a thin layer of PA gel with conjugated fibronectin allows cell adhesion (**b**, right panel). UV irradiation softens the gel, as indicated by an increase in probe indentation that is reflected in the embedded beads going out of focus in the UV-softening gel only (**c**, arrows) that is not seen on light-insensitive control PA gels. Softening is dose-dependent (**d**, mean +/- s.e.m., n = 10 from multiple gels). Scale bar, 100 μm.

4.4.d. Cellular responses to global illumination of substrates

NIH 3T3 fibroblasts plated on un-illuminated and globally pre-illuminated UV-sensitive gels showed similar differences in morphology as cells on photo-insensitive stiff and soft PA gels (Pelham and Wang 1997; Rajagopalan, Marganski et al. 2004) (Fig. 4.2a). By controlling the total energy of illumination, I was able to soften the gels ~ 22% (Fig. 4.1d) from 7.2 +/- 0.8 kPa to 5.5 +/- 0.1 kPa (n = 10). Equivalent illumination, when applied to cells on control PA gels or on FN-coated coverslips, caused no detectable response in spread area or protrusive activities (Fig. 4.2b), nor were there significant changes in migration speed (0.29 +/- 0.03 and 0.25 +/- 0.03 μm/min calculated over 2 hrs before and after UV, respectively, n = 8 each, *p*-value = 0.1126) or persistence (Frey, Tsai et al. 2006) (0.59 +/- 0.10 and 0.66 +/- 0.08 before and after UV, respectively, n = 8 each, *p*-value = 0.4890). Additionally, cell division proceeded normally (n = 6; Fig. 4.2c). The density of the illumination power was estimated to be 0.16 watt/cm^2, which was much lower than that reported to cause radiation damage (Besaratinia, Kim et al. 2007).

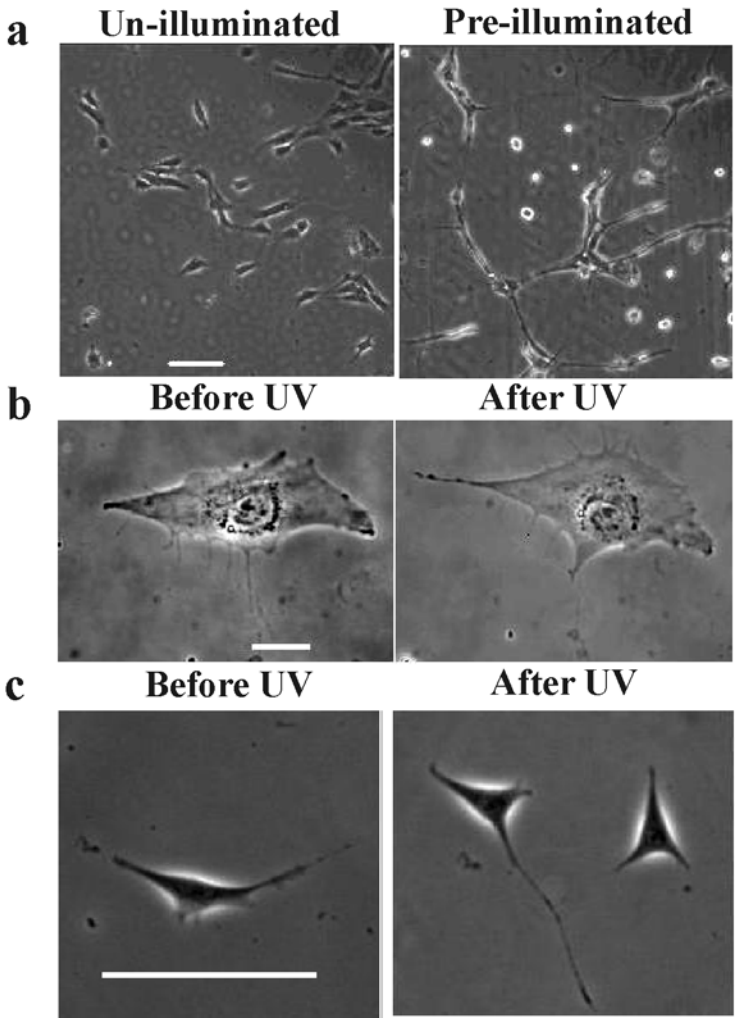

Figure 4.2. Irradiation affects morphology of cells on UV-softening gels but not on control PA gels.

Bulk irradiation of the gel surface inhibits spreading of NIH 3T3 cells on UV-softening substrates (**a**, right), as compared to cells on substrata without irradiation (**a**, left; scale bar, 100 μm). Cells on control PA gel also appears unaffected by the irradiation, showing similar morphology just before and 2 hr after UV exposure (**b**; scale bar, 20 μm). An irradiated cell on an FN-coated coverslip went through normal mitosis, creating two daughter cells (**c**, right panel; scale bar, 100 μm).

I examined the behavior of NIH 3T3 cells on UV-softening substrates before and after global UV exposure. The spread area of cells decreased substantially upon whole-cell exposure to UV (Figs. 4.3a and 4.3b). The response showed a rapid retraction (6 +/- 1% reduction in area immediately after UV exposure, *p*-value <0.0001) followed by a gradual, further decline in spread area to reach a steady state (12 +/- 1% reduction in area compared to just before UV, *p*-value <0.0001, n = 8, Fig. 4.3a and 4.3b). The initial retraction may reflect in part recoiling as a result of lowered substrate resistance against cellular traction forces, as indicated by the inward movements of fluorescent beads embedded in the substrata (i.e., increase in strain) (see illustration, Fig. 4.4). The beads were released subsequently, consistent with a decrease of traction forces and release of focal adhesions as cells reached a steady state on the softened substrata (Lo, Wang et al. 2000).

The cells appeared to actively probing the substrate following the initial retraction. However, the retraction (and the subsequent probing) occurred at slightly different times following illumination and inversely correlated with cell size. Therefore, I aligned the response data at the point of minimal area following irradiation. The results show a more tri-phasic response to softening (Fig. 4.5).

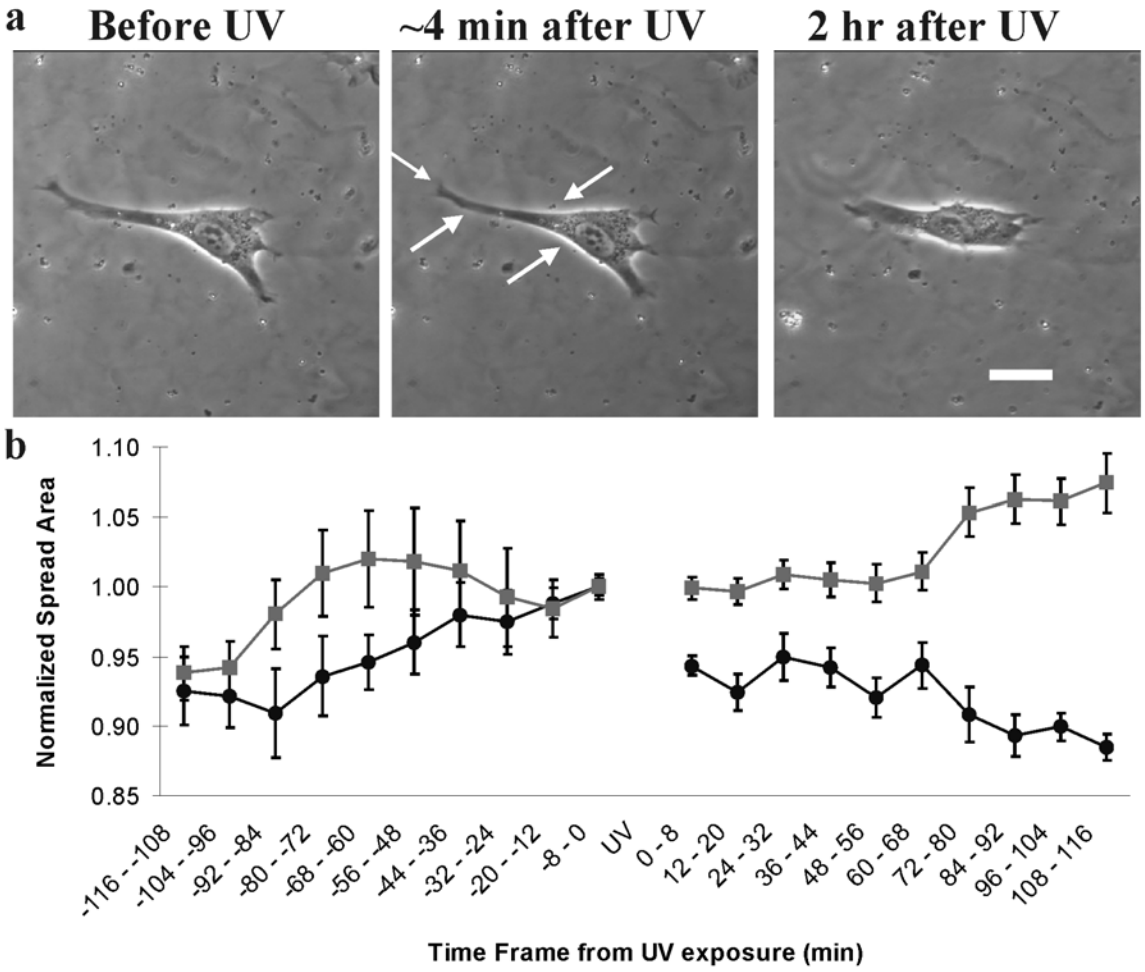

Figure 4.3. Responses of cells on UV-softening substrata to irradiation-induced substrate softening

Response to substrate softening includes an initial rapid retraction (**a**, middle) and a slower phase of reduction in spread area (**a**, right; scale bar, 20 μm). Measurements of cell area before and after irradiation at t = 0 shows the time course of retraction upon substrate softening (**b**, ●), while cells on control gels show no such response (**b**, ■). Spread area was normalized to the area just before UV and values are mean +/- s.e.m. (n = 8).

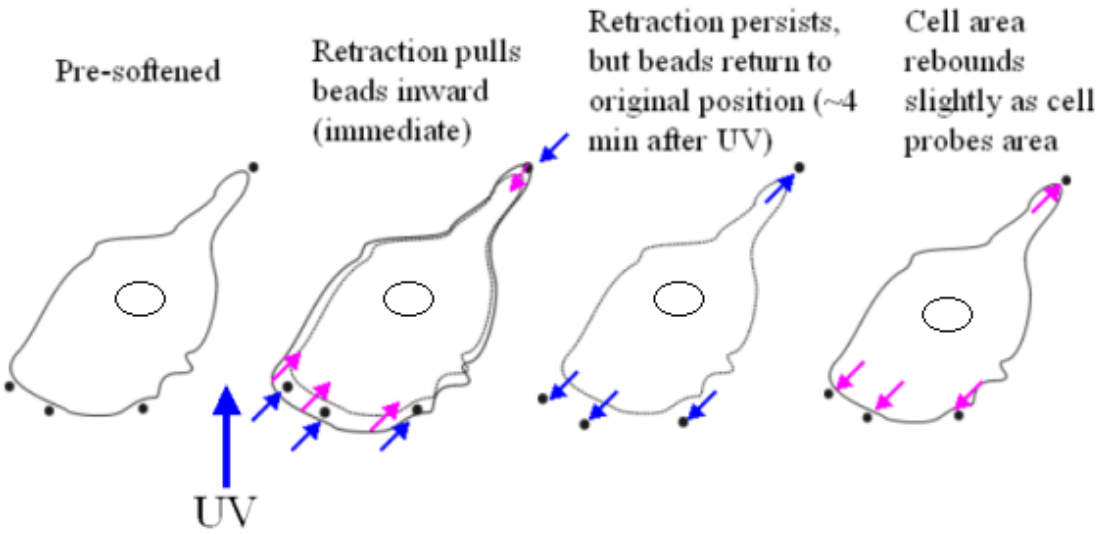

Figure 4.4. Illustration of intial retraction

Following irradiation-induced softening of the substrate, cells retract inward and pull the substrate inward, indicated from the movement of imbedded beads. This indicates that intracellular tension is generated to match the external tension imposed by the substrate. Since the beads are also pulled inward, the retraction is from tension rather than focal adhesion release. The softening reduces the external tension, causing the cell, suddenly of higher tension, to retract. Shortly thereafter (~4 min), the beads return to their original position while the cell remains retracted. This indicates that focal adhesions are released at a later time point. The spread area recovers somewhat as the cell probes the area some time later.

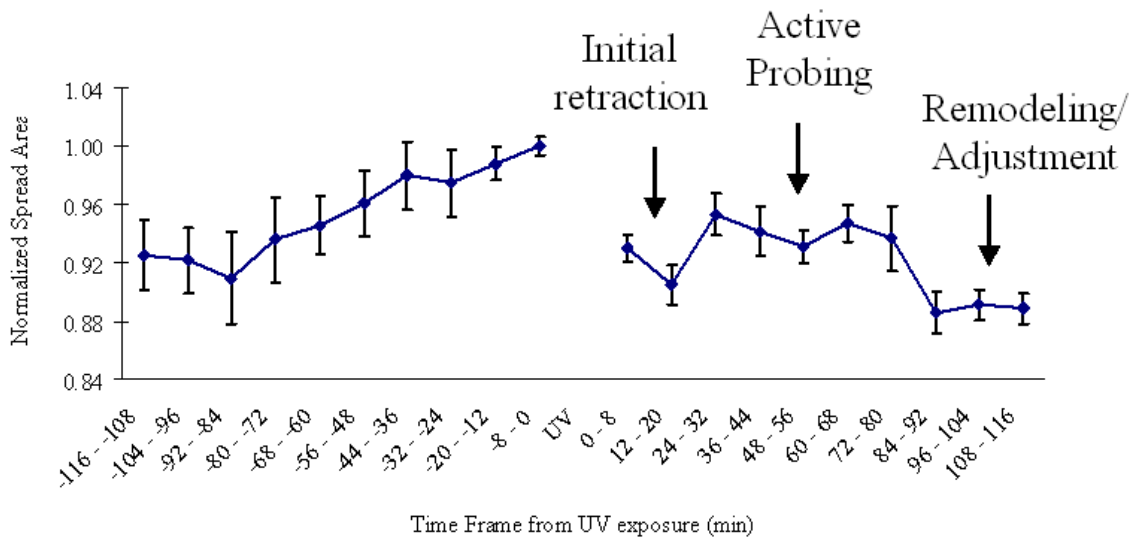

Figure 4.5. Response to global illumination

Alignment of the post-illumination data (n = 8) at the point of minimum retraction and averaging the values (8 min intervals) show a more pronounced triphasic response. Following the initial retraction, the cells probe the area in which the spread area increases slightly. The response is concluded with an adjustment in spread area to match the reduced stiffness of substrate.

4.4.e. Cellular responses to localized softening in posterior or anterior regions

By closing down the illumination field diaphragm to generate a UV beam ~50 μm in diameter, I compared the sensitivity of different regions of the cell to changes in substrate rigidity. Highly polarized cells with well defined tail regions (posterior) and frontal regions (anterior) were chosen and illuminated over either portion of the cell such that less than 50% of the nucleus was exposed in either case. Illumination of regions posterior to the nucleus caused no detectable response (Fig. 4.6), nor did illuminations of cells on control PA gels in either the anterior or posterior region (not shown). The cell area increased by 3 +/- 9% upon posterior illumination (n = 8). Slight increases in area were also observed following the illumination of cells on control PA gels (13 +/- 3% and 9 +/- 2% 2 hr following frontal and rear illumination respectively, n = 8 each). In contrast, softening the substratum region anterior to the nucleus caused a striking reduction in spread area (-16 +/- 7%, 2 hr following the irradiation, n = 8). In addition, depending on the size, shape, and migration of the cell, the cell either reversed the direction of migration or migrated randomly within the illuminated region (Figs. 4.6 and 4.7). The response to frontal illumination was more striking than that following global illumination, likely due to the stronger imbalance of forces when the softening was limited to part of the cell. These results indicate that rigidity sensing is largely confined to the anterior region, consistent with the idea that active traction forces, which are concentrated in the frontal region, are involved in probing substrate rigidity (Dembo and Wang 1999; Beningo, Dembo et al. 2001).

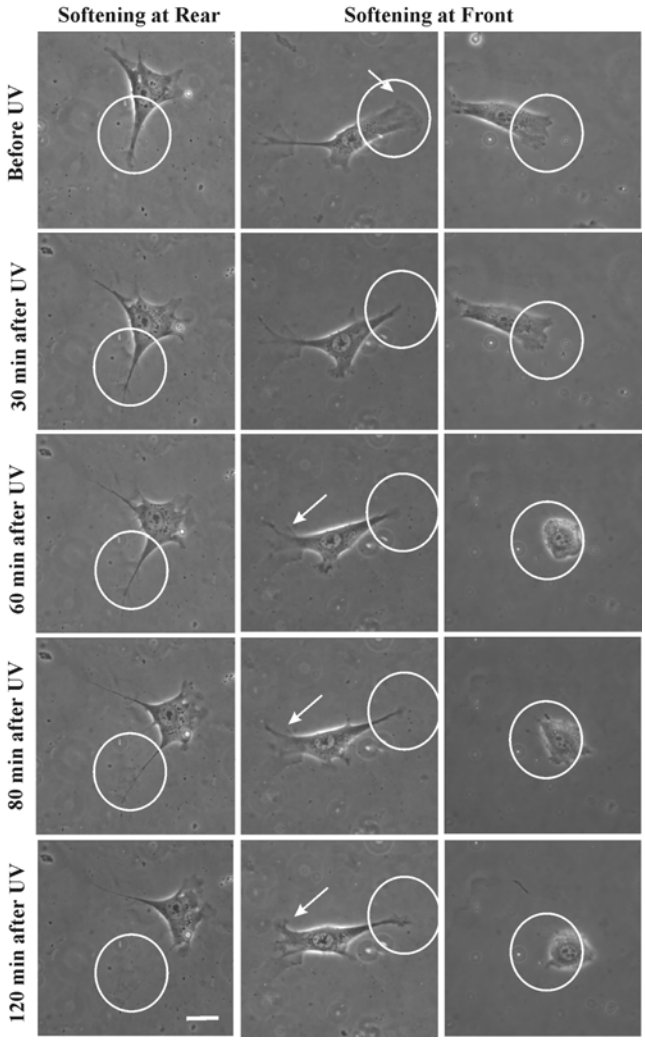

Figure 4.6. Localization of rigidity sensing to the cell anterior or posterior region

Softening of posterior substratum produces no change in area (left column). The cell often migrates away from the softened area. In contrast, softening of the anterior substratum elicits a dramatic response, whereby the cell either reverses its polarity (central column, arrows) or becomes trapped in the softened region (right column). Circles indicate irradiated areas. Scale bar, 20 μm.

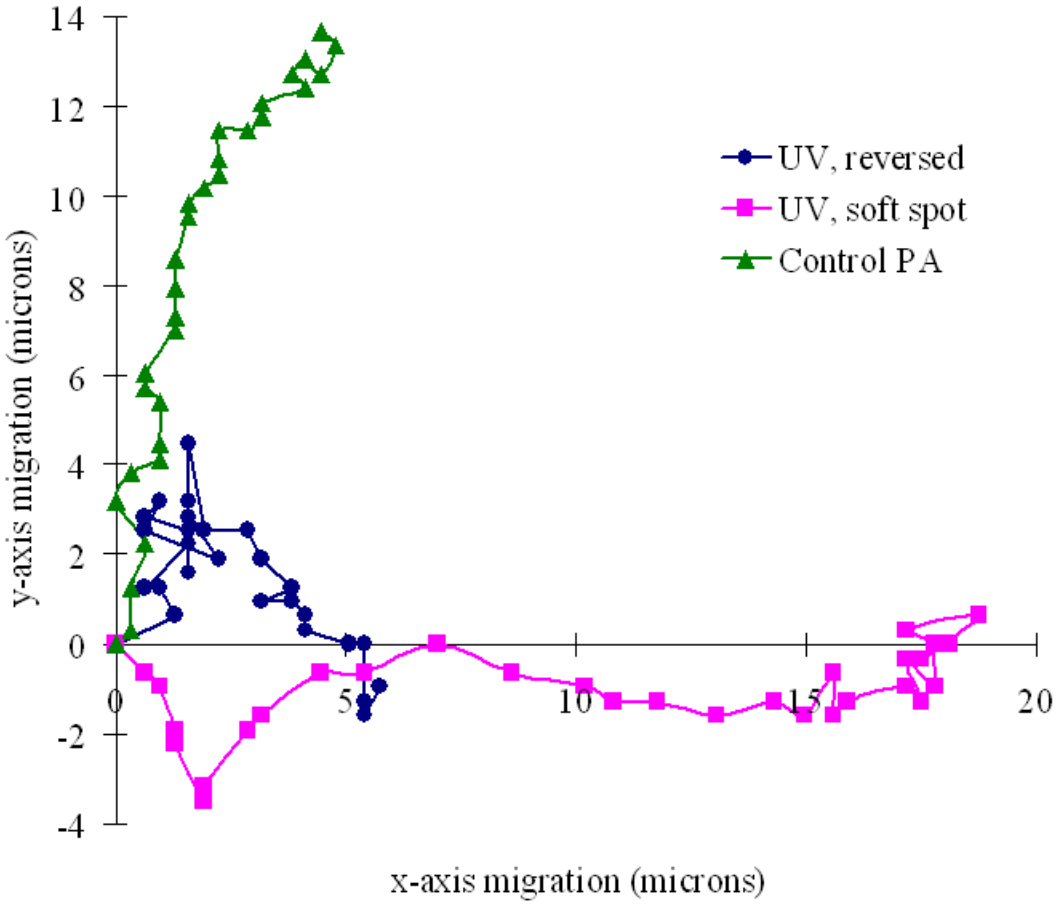

Figure 4.7. Persistence of cell migration before and after anterior illumination

Example plots of migration trajectory (total time of 2 hours in 4 min intervals) for cells on UV-softening gels or control PA gels after anterior illumination. Cells on UV-softening gels responded by either reversing polarity (●) or moving within the softening region (■). In contrast, anterior illumination of cells on control PA gels (▲) shows no effect on persistent migration. Origin represents initial position of the cell.

4.4.f. Detection of local responses to substrate rigidity at high resolution

To allow observations of local responses to substrate rigidity at a high magnification, substrates should be as thin as possible to accommodate the short working distance of the objective lens and reduce spherical aberration of oil lenses. However, the use of thin substrates also calls into question the ability of the cell to deform the material, as the substrate is tethered to the underlying immobile glass substrate. Additionally, it is important to rule out potential photobleaching and cellular damage by the focused light of high N.A. lenses. To address these concerns, the UV-sensitive layer of the substrates was made using just 15 µl of the solution. Cellular responses to global illumination (with a maximal energy equivalent to that using low N.A. lenses) were similar to those seen on thicker substrates. In contrast, cells on thin control substrates showed no detectable responses when exposed to the same dose of UV. Localized exposure of the anterior region of cells on UV-softening substrates had a similar effect to that seen at lower magnifications. Lastly, no photobleaching was detected after illumination of cells transfected with RFP-zyxin plated onto control PA and UV-softening gels.

4.5. Discussion

In summary, I showed that linear PA, functionalized and crosslinked with a photosensitive reagent and coated with FN, creates a UV-softening material suitable for probing the spatial and temporal responses of adherent cells to substrate rigidity. Cell spreading on the substrates before and after illumination show morphology similar to those on stiff and soft gels, respectively (Wang and Pelham Jr. 1998). By using spatial

control of softening, I show that mechanosensing is largely localized to the anterior of polarized cells. Similar studies at higher resolution are possible with this material, allowing for the molecular mechanisms to be studied in more detail, e.g. by using cells expressing fluorescently tagged structural or signaling components. The same chemical principles may be applied to other linear polymers to obtain a wide variety of UV-softening materials. In addition to probing cellular rigidity sensing, such materials may find wide applications in tissue engineering and regenerative medicine. Potential applications include the generation of micropatterned rigidity to differentially regulate cell polarity, growth and differentiation, as well as controlled timing for triggering these events at the optimal stage of tissue formation.

CHAPTER 5. SUMMARY AND DISCUSSION

Topographical and mechanical cues, such as substrata stiffness, have profound effects on cellular migration, spreading, adhesion, and differentiation. While the experimental systems used in these studies have been helpful in identifying these phenomena, the mechanisms that are responsible for these changes remain poorly understood. This study explored the differences in cell migration and spreading in response to topographical cues and substrate stiffness. This study also sought to identify some of the key molecules involved in the response to topography, and to create a novel softening substrate for probing the mechanisms involved in sensing substrate stiffness.

Although the phenomenon of contact guidance has been known for decades (Weiss 1941), the mechanism for sensing substrate topography remains elusive. By comparing normal, drug treated, and genetically manipulated cells plated on chemically identical substrates with flat surfaces or micron-sized pillars, I gained better understanding of the effects of topography on cellular responses and the molecules responsible, including FAK and myosin II (Chapter 2).

It is possible that the topographical features of the pillars induce changes to the shape of the cell membrane, such that the density of surface receptors and FAK-dependent reactions relative to the cell volume are increased. Interestingly, the migration speed increased despite the enhanced adhesion to the pillars. Although counterintuitive, this may be explained if the enhanced adhesion causes enhanced myosin II-dependent contractility. Indeed, attachment of cell extensions on the pillars was typically followed

by contraction that resulted in abrupt directional changes. Similar responses may be induced by other types of topographic and mechanical signals

The involvement of FAK in sensing and transmitting adhesion-mediated signals is also suggested by the reduced ruffling activities of FAK -/- cells on pillar substrates compared to FAK-expressing cells (Chapter 2) (Tilghman, Slack-Davis et al. 2005; Braren, Hu et al. 2006). FAK is known to autophosphorylate upon integrin activation at the Tyr-397 residue (Cary, Chang et al. 1996), which serves as a binding site for Src proteins and p130Cas. In response to integrin clustering, FAK likely recruits Src, which phosphorylates p130Cas (Petch, Bockholt et al. 1995; Vuori, Hirai et al. 1996). Tyrosine phosphorylated p130Cas then recruits Crk, an SH2/SH3 adaptor protein (Sakai, Iwamatsu et al. 1994). Interactions between complexed p130Cas-Crk and DOCK180-ELMO quinine nucleotide exchange factor (GEF) (Kiyokawa, Hashimoto et al. 1998; Kiyokawa, Hashimoto et al. 1998; Brugnera, Haney et al. 2002) leads to activation of the small GTPase, Rac1, which regulates cell migration by activation of the Arp2/3 complex (Miki, Yamaguchi et al. 2000) and the formation of lamellipodia and focal complexes at the leading edge (Nobes and Hall 1999). Therefore, FAK is likely involved in amplifying cytoplasmic chemical responses and providing a positive feedback to the adhesion signals at the leading edge.

Striking differences in cell migration and spreading were also found when cells were plated on polymer-based substrates with different rigidity (Pelham and Wang 1997). While there is a dramatic increase in the number of studies on the mechanism of rigidity

sensing, the quality of these studies relies on proper characterization of the mechanical properties of flexible substrates.

Although AFM represents an established, reliable and versatile approach, it is also costly and the analysis complicated. Testing soft samples using AFM is further complicated by inherently high error, mostly due to inaccuracies in the estimation of the contact point of the probe. Studies in Chapter 3 show that by using log-log plots of the force-indentation profiles, the data can be fit to the models of Hertz contact mechanics using simple, objective and reliable linear methods. Further improvements may be obtained by automatically determining the contact point of the AFM probe and the optimal range of analysis for fitting the data to the model. I have developed a program in Matlab to automate and increase the efficiency of this data analysis and to obtain more accurate values of Young's moduli.

I have further developed a new technique to measure substrate rigidity, using a microsphere at the tip of a flexible needle as an indenter following similar principles as AFM. Young's moduli obtained with this method agree with those obtained with AFM, validating its application in experiments that demand measurements on microscope stages, e.g. testing photo-modulatable gels (Chapter 4). This technique also represents a much simpler and more economical approach than AFM.

Despite lingering discrepancies between stiffness values obtained with different methods and even with the same method but by different parties, the responses of adherent cells to substrata stiffness have by now been well established. However, where these responses originate and how they are transduced remains to be determined. Recent

appreciation of the dynamics of signal complexes at focal adhesions has further led to a need for better understanding of the spatial and temporal elements of mechanotransduction.

This need spawned the invention of a photo-modulatable gel to allow spatial and temporal control of substrate stiffness at a high resolution (Chapter 4). The material responds within seconds of illumination in a dose-dependent matter, suitable for probing the responses that occur within seconds to minutes (Vogel and Sheetz 2006). The microsphere indentation technique proved to be highly efficient for assessing the stiffness and the photosensitivity of these gels during their optimization and application.

The photo-modulatable gel allowed me to determine the effects of both global and localized softening. Global softening included immediate inward retraction of the cell followed by a gradual decline in spread area, consistent with findings that cells generate internal tension to match that imposed by the substrate (Solon, Levental et al. 2007), and that cells spread more on stiffer substrates (Pelham and Wang 1997).

The photo-modulatable substrate also allows me to test localized rigidity sensing in relation to cell migration. Most models of cell migration agree that there are differences between adhesions at the cell posterior and anterior, which may thus respond differentially to rigidity signals. Softening at the posterior produced virtually no response, whereas softening at the anterior produces a response similar to, but more pronounced than global softening (Chapter 4). These results indicate that mechanosensing and/or transduction is localized at the cell anterior, consistent with response of cells to localized applications of the GRGDTP peptide (Munevar, Wang et al.

2001), a competitive inhibitor of integrin-ECM binding. A drastic and global decrease in traction force was seen after localized release of cell anterior, whereas release of the trailing edge by the same application caused no decrease in traction force elsewhere in the cell. Collectively, these results support a frontal towing and sensing model, whereby the leading edge is a mechanically distinct entity that exerts strong forces to tow the remaining anchored cell body forward while simultaneously responding to mechanical signals. These results are consistent with those of Munevar and coworkers (Munevar, Wang et al. 2001), and both are inconsistent with the tug-of-war model proposed by Bray (Bray 2001). Also consistent with this idea is the finding that nascent focal adhesions, concentrated at the leading edge, exert the strongest traction forces (Beningo, Dembo et al. 2001).

With the mechanosensitive region identified at the cell anterior, the next step would be to determine its sensitivity by answering the following questions. What is the smallest area over which a change in stiffness would result in a global cellular response? What is the smallest change in stiffness that a cell can detect? Furthermore, what is the mechanism(s) by which cells elicit the response to changes in stiffness?

To answer these questions, softening of the substrates can be performed at high resolution using laser microbeams. This should allow one to study the effects of incrementally smaller fields of illumination (softening), with the amount of softening controlled by the time of exposure. Furthermore, the responses in softened and adjacent unsoftened regions can be compared directly, to further elucidate the mechanisms involved in mechanosensing. Such insights may lead to the development of improved

medical devices, engineered tissues, and biomimetic materials for tissue repair and reconstruction. In addition, defects in mechanosensing and mechanotransduction may lead to poor wound healing, fibrosis, and cancer. Abnormal responses to extracellular mechanical cues may also underlie such diverse diseases as asthma, osteoporosis, atherosclerosis, diabetes, stroke, and heart failure (Ingber 2003). Therefore, molecules that mediate mechanotransduction could be potential targets in the therapeutic treatment of a variety of diseases. The present study, using substrata with topographical features and materials that allow spatial and temporal modulation at high resolution, represents a significant step toward elucidating these mechanisms.

BIBLIOGRAPHY

Abercrombie, M. and G. A. Dunn (1975). "Adhesions of fibroblasts to substratum during contact inhibition observed by interference reflection microscopy." Exp Cell Res **92**(1): 57-62.

Abraham, V. C., V. Krishnamurthi, et al. (1999). "The actin-based nanomachine at the leading edge of migrating cells." Biophys J **77**(3): 1721-32.

Akiri, G., E. Sabo, et al. (2003). "Lysyl oxidase-related protein-1 promotes tumor fibrosis and tumor progression in vivo." Cancer Res **63**(7): 1657-66.

Alberts, B., A. Johnson, et al. (2002). Molecular Biology of the Cell. New York, Garland Science.

Allingham, J. S., R. Smith, et al. (2005). "The structural basis of blebbistatin inhibition and specificity for myosin II." Nat Struct Mol Biol.

Alpin, J. and C. Hughes (1981). "Protein-derivatised glass coverslips for the study of cell-to-substratum adhesion." Anal. Biochem. **113**: 144-148.

Ausprunk, D. H. and J. Folkman (1977). "Migration and proliferation of endothelial cells in preformed and newly formed blood vessels during tumor angiogenesis." Microvasc Res **14**(1): 53-65.

Balaban, N. Q., U. S. Schwarz, et al. (2001). "Force and focal adhesion assembly: a close relationship studied using elastic micropatterned substrates." Nat Cell Biol **3**(5): 466-72.

Ballestrem, C., B. Hinz, et al. (2001). "Marching at the front and dragging behind: differential alphaVbeta3-integrin turnover regulates focal adhesion behavior." J Cell Biol **155**(7): 1319-32.

Bataller, R., P. Sancho-Bru, et al. (2005). "Liver fibrogenesis: a new role for the renin-angiotensin system." Antioxid Redox Signal **7**(9-10): 1346-55.

Bausch, A. R., U. Hellerer, et al. (2001). "Rapid stiffening of integrin receptor-actin linkages in endothelial cells stimulated with thrombin: a magnetic bead microrheology study." Biophys J **80**(6): 2649-57.

Beil, M., A. Micoulet, et al. (2003). "Sphingosylphosphorylcholine regulates keratin network architecture and visco-elastic properties of human cancer cells." Nat Cell Biol **5**(9): 803-11.

Beningo, K., C. Lo, et al. (2002). Flexible Polyacrylamide Substrata for the Analysis of Mechanical Interactions at Cell-Substrata Adhesions. Methods in Cell Biology, Elsevier Science (USA). **69:** 325-339.

Beningo, K. A., M. Dembo, et al. (2001). "Nascent focal adhesions are responsible for the generation of strong propulsive forces in migrating fibroblasts." J Cell Biol **153**(4): 881-8.

Beningo, K. A., M. Dembo, et al. (2004). "Responses of fibroblasts to anchorage of dorsal extracellular matrix receptors." Proc Natl Acad Sci U S A **101**(52): 18024-9.

Beningo, K. A., K. Hamao, et al. (2006). "Traction forces of fibroblasts are regulated by the Rho-dependent kinase but not by the myosin light chain kinase." Arch Biochem Biophys **456**(2): 224-31.

Bennig, G., C. F. Quate, et al. (1986). "Atomic Force Microscope." Phys Rev Lett **56**: 930-933.

Berry, C. C., G. Campbell, et al. (2004). "The influence of microscale topography on fibroblast attachment and motility." Biomaterials **25**(26): 5781-8.

Bershadsky, A., A. Chausovsky, et al. (1996). "Involvement of microtubules in the control of adhesion-dependent signal transduction." Curr Biol **6**(10): 1279-89.

Bershadsky, A. D., N. Q. Balaban, et al. (2003). "Adhesion-dependent cell mechanosensitivity." Annu Rev Cell Dev Biol **19**: 677-95.

Besaratinia, A., S. I. Kim, et al. (2007). "Riboflavin activated by ultraviolet A1 irradiation induces oxidative DNA damage-mediated mutations inhibited by vitamin C." Proc Natl Acad Sci U S A **104**(14): 5953-8.

Bhatt, A., I. Kaverina, et al. (2002). "Regulation of focal complex composition and disassembly by the calcium-dependent protease calpain." J Cell Sci **115**(Pt 17): 3415-25.

Bischoff, F. and G. Bryson (1964). "Carcinogenesis through Solid State Surfaces." Prog Exp Tumor Res **5**: 85-133.

Bondy, G. P., S. Wilson, et al. (1985). "Experimental metastatic ability of H-ras-transformed NIH3T3 cells." Cancer Res **45**(12 Pt 1): 6005-9.

Boudreau, N. J. and P. L. Jones (1999). "Extracellular matrix and integrin signalling: the shape of things to come." Biochem J **339 (Pt 3)**: 481-8.
Bourke, S. L., M. Al-Khalili, et al. (2003). "A photo-crosslinked poly(vinyl alcohol) hydrogel growth factor release vehicle for wound healing applications." AAPS PharmSci **5**(4): E33.
Boyd, N. F., G. A. Lockwood, et al. (1998). "Mammographic densities and breast cancer risk." Cancer Epidemiol Biomarkers Prev **7**(12): 1133-44.
Braet, F., R. de Zanger, et al. (2001). "A comparative atomic force microscopy study on living skin fibroblasts and liver endothelial cells." J Electron Microsc (Tokyo) **50**(4): 283-90.
Braren, R., H. Hu, et al. (2006). "Endothelial FAK is essential for vascular network stability, cell survival, and lamellipodial formation." J Cell Biol **172**(1): 151-62.
Bray, D. (2001). Cell movements: from molecules to motility. New York, Garland Publishing.
Brown, T. D. (2000). "Techniques for mechanical stimulation of cells in vitro: a review." J Biomech **33**(1): 3-14.
Brugnera, E., L. Haney, et al. (2002). "Unconventional Rac-GEF activity is mediated through the Dock180-ELMO complex." Nat Cell Biol **4**(8): 574-82.
Bulinski, J. C. and G. G. Gundersen (1991). "Stabilization of post-translational modification of microtubules during cellular morphogenesis." Bioessays **13**(6): 285-93.
Burnham, N., X. Chen, et al. (2003). "Comparison of Calibration Methods for Atomic-Force Microscopy Cantilevers." Nantechnology **14**: 1-6.
Burnham, N. and R. Colton (1989). "Measuring the nanomechanical properties and surface forces of materials using an atomic force microscope." J. Vac. Sci. Technol. A. **7**(4): 2906-2913.
Burridge, K. and M. Chrzanowska-Wodnicka (1996). "Focal adhesions, contractility, and signaling." Annu Rev Cell Dev Biol **12**: 463-518.
Calalb, M. B., T. R. Polte, et al. (1995). "Tyrosine phosphorylation of focal adhesion kinase at sites in the catalytic domain regulates kinase activity: a role for Src family kinases." Mol Cell Biol **15**(2): 954-63.
Calalb, M. B., X. Zhang, et al. (1996). "Focal adhesion kinase tyrosine-861 is a major site of phosphorylation by Src." Biochem Biophys Res Commun **228**(3): 662-8.
Cance, W. G., J. E. Harris, et al. (2000). "Immunohistochemical analyses of focal adhesion kinase expression in benign and malignant human breast and colon tissues: correlation with preinvasive and invasive phenotypes." Clin Cancer Res **6**(6): 2417-23.
Carlson, M. A., M. T. Longaker, et al. (2004). "Modulation of FAK, Akt, and p53 by stress release of the fibroblast-populated collagen matrix." J Surg Res **120**(2): 171-7.
Carter, S. B. (1967). "Haptotaxis and the mechanism of cell motility." Nature **213**(73): 256-60.
Cary, L. A., J. F. Chang, et al. (1996). "Stimulation of cell migration by overexpression of focal adhesion kinase and its association with Src and Fyn." J Cell Sci **109 (Pt 7)**: 1787-94.
Cary, L. A., D. C. Han, et al. (1998). "Identification of p130Cas as a mediator of focal adhesion kinase-promoted cell migration." J Cell Biol **140**(1): 211-21.
Cattaruzza, M., C. Lattrich, et al. (2004). "Focal adhesion protein zyxin is a mechanosensitive modulator of gene expression in vascular smooth muscle cells." Hypertension **43**(4): 726-30.
Chen, B. H., J. T. Tzen, et al. (2002). "Roles of Rho-associated kinase and myosin light chain kinase in morphological and migratory defects of focal adhesion kinase-null cells." J Biol Chem **277**(37): 33857-63.
Chen, C. S., M. Mrksich, et al. (1997). "Geometric control of cell life and death." Science **276**(5317): 1425-8.
Chen, C. S., M. Mrksich, et al. (1998). "Micropatterned surfaces for control of cell shape, position, and function." Biotechnol Prog **14**(3): 356-63.
Chen, C. S., J. Tan, et al. (2004). "Mechanotransduction at cell-matrix and cell-cell contacts." Annu Rev Biomed Eng **6**: 275-302.
Chen, H., D. M. Choudhury, et al. (2006). "Coincidence of actin filaments and talin is required to activate vinculin." J Biol Chem **281**(52): 40389-98.

Chen, J., B. Fabry, et al. (2001). "Twisting integrin receptors increases endothelin-1 gene expression in endothelial cells." Am J Physiol Cell Physiol **280**(6): C1475-84.
Chen, Q., M. S. Kinch, et al. (1994). "Integrin-mediated cell adhesion activates mitogen-activated protein kinases." J Biol Chem **269**(43): 26602-5.
Chen, W. T. (1981). "Surface changes during retraction-induced spreading of fibroblasts." J Cell Sci **49**: 1-13.
Chesmel, K. D., C. C. Clark, et al. (1995). "Cellular responses to chemical and morphologic aspects of biomaterial surfaces. II. The biosynthetic and migratory response of bone cell populations." J Biomed Mater Res **29**(9): 1101-10.
Choquet, D., D. P. Felsenfeld, et al. (1997). "Extracellular matrix rigidity causes strengthening of integrin-cytoskeleton linkages." Cell **88**(1): 39-48.
Chu, E. K., J. S. Foley, et al. (2005). "Bronchial epithelial compression regulates epidermal growth factor receptor family ligand expression in an autocrine manner." Am J Respir Cell Mol Biol **32**(5): 373-80.
Clark, P., P. Connolly, et al. (1987). "Topographical control of cell behaviour. I. Simple step cues." Development **99**(3): 439-48.
Clark, P., P. Connolly, et al. (1990). "Topographical control of cell behaviour: II. Multiple grooved substrata." Development **108**(4): 635-44.
Collinsworth, A. M., S. Zhang, et al. (2002). "Apparent elastic modulus and hysteresis of skeletal muscle cells throughout differentiation." Am J Physiol Cell Physiol **283**(4): C1219-27.
Colpaert, C., P. Vermeulen, et al. (2001). "The presence of a fibrotic focus is an independent predictor of early metastasis in lymph node-negative breast cancer patients." Am J Surg Pathol **25**(12): 1557-8.
Crouch, D. H., V. J. Fincham, et al. (1996). "Targeted proteolysis of the focal adhesion kinase pp125 FAK during c-MYC-induced apoptosis is suppressed by integrin signalling." Oncogene **12**(12): 2689-96.
Cukierman, E., R. Pankov, et al. (2001). "Taking cell-matrix adhesions to the third dimension." Science **294**(5547): 1708-12.
Cukierman, E., R. Pankov, et al. (2002). "Cell interactions with three-dimensional matrices." Curr Opin Cell Biol **14**(5): 633-9.
Curtis, A. and C. Wilkinson (2001). "Nantotechniques and approaches in biotechnology." Trends Biotechnol **19**(3): 97-101.
Curtis, A. S., B. Casey, et al. (2001). "Substratum nanotopography and the adhesion of biological cells. Are symmetry or regularity of nanotopography important?" Biophys Chem **94**(3): 275-83.
Dalby, M. J., M. O. Riehle, et al. (2005). "Morphological and microarray analysis of human fibroblasts cultured on nanocolumns produced by colloidal lithography." Eur Cell Mater **9**: 1-8; discussion 8.
Dalby, M. J., S. J. Yarwood, et al. (2002). "Increasing fibroblast response to materials using nanotopography: morphological and genetic measurements of cell response to 13-nm-high polymer demixed islands." Exp Cell Res **276**(1): 1-9.
Damianova, R., N. Stefanova, et al. (2008). "Three-dimensional matrix induces sustained activation of ERK1/2 via Src/Ras/Raf signaling pathway." Cell Biol Int **32**(2): 229-34.
Darby, I. A. and T. D. Hewitson (2007). "Fibroblast differentiation in wound healing and fibrosis." Int Rev Cytol **257**: 143-79.
Davidson, L. and R. Keller (2007). "Measuring mechanical properties of embryos and embryonic tissues." Methods Cell Biol **83**: 425-39.
Dedhar, S., E. Ruoslahti, et al. (1987). "A cell surface receptor complex for collagen type I recognizes the Arg-Gly-Asp sequence." J Cell Biol **104**(3): 585-93.
Dee, K., M. Freer, et al. (2002). "Apoptosis coincident with the differentiation of skeletal myoblasts is delayed by caspase 3 inhibition and abrogated by MEK-independent constitutive Ras signaling." Cell Death Differ **9**(2): 209-18.
Dee, K. C., D. A. Puleo, et al. (2002). An Introduction to Tissue-Biomaterial Interactions. Hoboken, NJ, John Wiley & Sons.

Delcommenne, M. and C. H. Streuli (1995). "Control of integrin expression by extracellular matrix." J Biol Chem **270**(45): 26794-801.
Dembo, M. and Y. L. Wang (1999). "Stresses at the cell-to-substrate interface during locomotion of fibroblasts." Biophys J **76**(4): 2307-16.
den Braber, E. T., J. E. de Ruijter, et al. (1998). "Orientation of ECM protein deposition, fibroblast cytoskeleton, and attachment complex components on silicone microgrooved surfaces." J Biomed Mater Res **40**(2): 291-300.
Dike, L. E., C. S. Chen, et al. (1999). "Geometric control of switching between growth, apoptosis, and differentiation during angiogenesis using micropatterned substrates." In Vitro Cell Dev Biol Anim **35**(8): 441-8.
Dimitriadis, E. K., F. Horkay, et al. (2002). "Determination of elastic moduli of thin layers of soft material using the atomic force microscope." Biophys J **82**(5): 2798-810.
Discher, D. E., P. Janmey, et al. (2005). "Tissue cells feel and respond to the stiffness of their substrate." Science **310**(5751): 1139-43.
Domke, J. and M. Radmacher (1998). "Measuring the elastic properties of thin polymer films with the atomic force microscope." Langmuir **14**: 3320-3325.
Dowell-Mesfin, N. M., M. A. Abdul-Karim, et al. (2004). "Topographically modified surfaces affect orientation and growth of hippocampal neurons." J Neural Eng **1**(2): 78-90.
Drees, B. E., K. M. Andrews, et al. (1999). "Molecular dissection of zyxin function reveals its involvement in cell motility." J Cell Biol **147**(7): 1549-60.
Dunn, G. A. (1983). "Characterising a kinesis response: time averaged measures of cell speed and directional persistence." Agents Actions Suppl **12**: 14-33.
Eckes, B., P. Zigrino, et al. (2000). "Fibroblast-matrix interactions in wound healing and fibrosis." Matrix Biol **19**(4): 325-32.
Edlund, M., M. A. Lotano, et al. (2001). "Dynamics of alpha-actinin in focal adhesions and stress fibers visualized with alpha-actinin-green fluorescent protein." Cell Motil Cytoskeleton **48**(3): 190-200.
Engler, A., L. Bacakova, et al. (2004). "Substrate compliance versus ligand density in cell on gel responses." Biophys J **86**(1 Pt 1): 617-28.
Engler, A., L. Richert, et al. (2004). "Surface probe measurements of the elasticity of sectioned tissue, thin gels and polyelectrolyte multilayer films: Correlation between substrate stiffness and cell adhesion." Surface Science **570**: 142-154.
Engler, A. J., M. A. Griffin, et al. (2004). "Myotubes differentiate optimally on substrates with tissue-like stiffness: pathological implications for soft or stiff microenvironments." J Cell Biol **166**(6): 877-87.
Engler, A. J., H. L. Sweeney, et al. (2007). "Extracellular matrix elasticity directs stem cell differentiation." J Musculoskelet Neuronal Interact **7**(4): 335.
Erickson, H. P. (1994). "Reversible unfolding of fibronectin type III and immunoglobulin domains provides the structural basis for stretch and elasticity of titin and fibronectin." Proc Natl Acad Sci U S A **91**(21): 10114-8.
Ezratty, E. J., M. A. Partridge, et al. (2005). "Microtubule-induced focal adhesion disassembly is mediated by dynamin and focal adhesion kinase." Nat Cell Biol **7**(6): 581-90.
Fan, H., Y. Lu, et al. (2000). "Rapid prototyping of patterned functional nanostructures." Nature **405**(6782): 56-60.
Fessler, H. and E. Ollerton (1957). "Contact stresses in toroids under radial loads." British Journal of Applied Physics **8**(387): 387-393.
Field, J. and M. Swain (1993). "A simple predictive model for spherical indentation." J Mater Res **8**: 297-305.
Finer, J. T., R. M. Simmons, et al. (1994). "Single myosin molecule mechanics: piconewton forces and nanometre steps." Nature **368**(6467): 113-9.
Flanagan, L. A., Y. E. Ju, et al. (2002). "Neurite branching on deformable substrates." Neuroreport **13**(18): 2411-5.
Folkman, J. and A. Moscona (1978). "Role of cell shape in growth control." Nature **273**(5661): 345-9.

Fonseca, P. M., N. Y. Shin, et al. (2004). "Regulation and localization of CAS substrate domain tyrosine phosphorylation." Cell Signal **16**(5): 621-9.
Freeman, A. (1987). Gel entrapment of whole cells in cross-linked prepolymerized polyacrylamide-hydrazide gels. Methods in Enzymology. S. P. Colowick and N. O. Kaplan. Orlando, FL, American Press, Inc. **135 B:** 216-222.
Frey, M., A. Engler, et al. (2007). Microscopic Methods for Measuring the Elasticity of Gel Substrates for Cell Culture: Microspheres, Microindenters, and Atomic Force Microscopy. Methods in Cell Biology, Elsevier, Inc. **83:** 45-63.
Frey, M. T., I. Y. Tsai, et al. (2006). "Cellular Responses to 3D Substrate Topography: Role of Myosin II and Focal Adhesion Kinase." Biophys J.
Friedl, P. and E. B. Brocker (2000). "The biology of cell locomotion within three-dimensional extracellular matrix." Cell Mol Life Sci **57**(1): 41-64.
Friedl, P., K. S. Zanker, et al. (1998). "Cell migration strategies in 3-D extracellular matrix: differences in morphology, cell matrix interactions, and integrin function." Microsc Res Tech **43**(5): 369-78.
Frisch, S. M., K. Vuori, et al. (1996). "Control of adhesion-dependent cell survival by focal adhesion kinase." J Cell Biol **134**(3): 793-9.
Fritz, G., I. Just, et al. (1999). "Rho GTPases are over-expressed in human tumors." Int J Cancer **81**(5): 682-7.
Gaggioli, C., S. Hooper, et al. (2007). "Fibroblast-led collective invasion of carcinoma cells with differing roles for RhoGTPases in leading and following cells." Nat Cell Biol **9**(12): 1392-400.
Galbraith, C. G. and M. P. Sheetz (1997). "A micromachined device provides a new bend on fibroblast traction forces." Proc Natl Acad Sci U S A **94**(17): 9114-8.
Galbraith, C. G., K. M. Yamada, et al. (2002). "The relationship between force and focal complex development." J Cell Biol **159**(4): 695-705.
Galvez, B. G., S. Matias-Roman, et al. (2001). "Membrane type 1-matrix metalloproteinase is activated during migration of human endothelial cells and modulates endothelial motility and matrix remodeling." J Biol Chem **276**(40): 37491-500.
Gaudet, C., W. A. Marganski, et al. (2003). "Influence of type I collagen surface density on fibroblast spreading, motility, and contractility." Biophys J **85**(5): 3329-35.
Gehlsen, K. R., W. S. Argraves, et al. (1988). "Inhibition of in vitro tumor cell invasion by Arg-Gly-Asp-containing synthetic peptides." J Cell Biol **106**(3): 925-30.
Geiger, B. and A. Bershadsky (2001). "Assembly and mechanosensory function of focal contacts." Curr Opin Cell Biol **13**(5): 584-92.
Geiger, B. and A. Bershadsky (2002). "Exploring the neighborhood: adhesion-coupled cell mechanosensors." Cell **110**(2): 139-42.
Geiger, B., A. Bershadsky, et al. (2001). "Transmembrane extracellular matrix-cytoskeleton crosstalk." Nat Rev Mol Cell Biol **2**(11): 793-805.
George, E. L., E. N. Georges-Labouesse, et al. (1993). "Defects in mesoderm, neural tube and vascular development in mouse embryos lacking fibronectin." Development **119**(4): 1079-91.
Georges, P. C., J. J. Hui, et al. (2007). "Increased stiffness of the rat liver precedes matrix deposition: implications for fibrosis." Am J Physiol Gastrointest Liver Physiol **293**(6): G1147-54.
Georges, P. C. and P. A. Janmey (2005). "Cell type-specific response to growth on soft materials." J Appl Physiol **98**(4): 1547-53.
Georges, P. C., W. J. Miller, et al. (2006). "Matrices with compliance comparable to that of brain tissue select neuronal over glial growth in mixed cortical cultures." Biophys J.
Ghosh, K., Z. Pan, et al. (2007). "Cell adaptation to a physiologically relevant ECM mimic with different viscoelastic properties." Biomaterials **28**(4): 671-9.
Giannone, G., G. Jiang, et al. (2003). "Talin1 is critical for force-dependent reinforcement of initial integrin-cytoskeleton bonds but not tyrosine kinase activation." J Cell Biol **163**(2): 409-19.
Giannone, G., P. Ronde, et al. (2004). "Calcium rises locally trigger focal adhesion disassembly and enhance residency of focal adhesion kinase at focal adhesions." J Biol Chem **279**(27): 28715-23.

Glogauer, M. and J. Ferrier (1998). "A new method for application of force to cells via ferric oxide beads." Pflugers Arch **435**(2): 320-7.
Goffin, J. M., P. Pittet, et al. (2006). "Focal adhesion size controls tension-dependent recruitment of alpha-smooth muscle actin to stress fibers." J Cell Biol **172**(2): 259-68.
Goldmann, W. H. and D. E. Ingber (2002). "Intact vinculin protein is required for control of cell shape, cell mechanics, and rac-dependent lamellipodia formation." Biochem Biophys Res Commun **290**(2): 749-55.
Golsteyn, R. M., M. C. Beckerle, et al. (1997). "Structural and functional similarities between the human cytoskeletal protein zyxin and the ActA protein of Listeria monocytogenes." J Cell Sci **110 (Pt 16)**: 1893-906.
Gray, D. S., J. Tien, et al. (2003). "Repositioning of cells by mechanotaxis on surfaces with micropatterned Young's modulus." J Biomed Mater Res A **66**(3): 605-14.
Griffin, M. A., A. J. Engler, et al. (2004). "Patterning, prestress, and peeling dynamics of myocytes." Biophys J **86**(2): 1209-22.
Griffith, L. M., S. M. Downs, et al. (1987). "Myosin light chain kinase and myosin light chain phosphatase from Dictyostelium: effects of reversible phosphorylation on myosin structure and function." J Cell Biol **104**(5): 1309-23.
Guha, M., M. Zhou, et al. (2005). "Cortical actin turnover during cytokinesis requires myosin II." Curr Biol **15**(8): 732-6.
Gundersen, G. G. and T. A. Cook (1999). "Microtubules and signal transduction." Curr Opin Cell Biol **11**(1): 81-94.
Guo, W. and F. G. Giancotti (2004). "Integrin signalling during tumour progression." Nat Rev Mol Cell Biol **5**(10): 816-26.
Guo, W. H., M. T. Frey, et al. (2006). "Substrate rigidity regulates the formation and maintenance of tissues." Biophys J **90**(6): 2213-20.
Guo, W. H. and Y. L. Wang (2007). "Retrograde fluxes of focal adhesion proteins in response to cell migration and mechanical signals." Mol Biol Cell **18**(11): 4519-27.
Habermann, B. (2004). "The BAR-domain family of proteins: a case of bending and binding?" EMBO Rep **5**(3): 250-5.
Harris, A. K., P. Wild, et al. (1980). "Silicone rubber substrata: a new wrinkle in the study of cell locomotion." Science **208**(4440): 177-9.
Harte, M. T., J. D. Hildebrand, et al. (1996). "p130Cas, a substrate associated with v-Src and v-Crk, localizes to focal adhesions and binds to focal adhesion kinase." J Biol Chem **271**(23): 13649-55.
Hertz, H. J. (1882). "Über die Berührung fester elastischer Körper." J. Reine Angew. Mathematik **92: p.156-171.**: 156-171.
Hill, M. A., Z. Sun, et al. (2007). "New technologies for dissecting the arteriolar myogenic response." Trends Pharmacol Sci **28**(7): 308-15.
Hill, S. A., S. Wilson, et al. (1988). "Clonal heterogeneity, experimental metastatic ability, and p21 expression in H-ras-transformed NIH 3T3 cells." J Natl Cancer Inst **80**(7): 484-90.
Hochmuth, R. M. (2000). "Micropipette aspiration of living cells." J Biomech **33**(1): 15-22.
Honer, B., S. Citi, et al. (1988). "Modulation of cellular morphology and locomotory activity by antibodies against myosin." J Cell Biol **107**(6 Pt 1): 2181-9.
Horwitz, A. R. and J. T. Parsons (1999). "Cell migration--movin' on." Science **286**(5442): 1102-3.
Hu, S., J. Chen, et al. (2003). "Intracellular stress tomography reveals stress focusing and structural anisotropy in cytoskeleton of living cells." Am J Physiol Cell Physiol **285**(5): C1082-90.
Huang, H., R. D. Kamm, et al. (2004). "Cell mechanics and mechanotransduction: pathways, probes, and physiology." Am J Physiol Cell Physiol **287**(1): C1-11.
Huang, S. and D. E. Ingber (2005). "Cell tension, matrix mechanics, and cancer development." Cancer Cell **8**(3): 175-6.
Humphries, J. D., P. Wang, et al. (2007). "Vinculin controls focal adhesion formation by direct interactions with talin and actin." J Cell Biol **179**(5): 1043-57.

Hungerford, J. E., M. T. Compton, et al. (1996). "Inhibition of pp125FAK in cultured fibroblasts results in apoptosis." J Cell Biol **135**(5): 1383-90.
Ilic, D., Y. Furuta, et al. (1995). "Reduced cell motility and enhanced focal adhesion contact formation in cells from FAK-deficient mice." Nature **377**(6549): 539-44.
Ilic, D., O. Genbacev, et al. (2001). "Plasma membrane-associated pY397FAK is a marker of cytotrophoblast invasion in vivo and in vitro." Am J Pathol **159**(1): 93-108.
Ilic, D., B. Kovacic, et al. (2004). "FAK promotes organization of fibronectin matrix and fibrillar adhesions." J Cell Sci **117**(Pt 2): 177-87.
Ingber, D. E. (2003). "Mechanobiology and diseases of mechanotransduction." Ann Med **35**(8): 564-77.
Ingber, D. E. (2008). "Can cancer be reversed by engineering the tumor microenvironment?" Semin Cancer Biol.
Ingber, D. E., J. A. Madri, et al. (1981). "Role of basal lamina in neoplastic disorganization of tissue architecture." Proc Natl Acad Sci U S A **78**(6): 3901-5.
Izard, T., G. Evans, et al. (2004). "Vinculin activation by talin through helical bundle conversion." Nature **427**(6970): 171-5.
Jacot, J. G., S. Dianis, et al. (2006). "A simple microindentation technique for mapping the microscale compliance of soft hydrated materials and tissues." J Biomed Mater Res A **79**(3): 485-94.
Janmey, P. A., P. C. Georges, et al. (2007). "Basic rheology for biologists." Methods Cell Biol **83**: 3-27.
Janmey, P. A. and C. A. McCulloch (2007). "Cell mechanics: integrating cell responses to mechanical stimuli." Annu Rev Biomed Eng **9**: 1-34.
Janmey, P. A. and D. A. Weitz (2004). "Dealing with mechanics: mechanisms of force transduction in cells." Trends Biochem Sci **29**(7): 364-70.
Jiang, G., A. H. Huang, et al. (2006). "Rigidity sensing at the leading edge through alphavbeta3 integrins and RPTPalpha." Biophys J **90**(5): 1804-9.
Johnson, K. L. (1985). Contact Mechanics. Cambridge, Cambridge University Press.
Juhasz, I., G. F. Murphy, et al. (1993). "Regulation of extracellular matrix proteins and integrin cell substratum adhesion receptors on epithelium during cutaneous human wound healing in vivo." Am J Pathol **143**(5): 1458-69.
Justesen, J., M. Lorentzen, et al. (2008). "Spatial and temporal changes in the morphology of preosteoblastic cells seeded on microstructured tantalum surfaces." J Biomed Mater Res A.
Kandow, C. E., P. C. Georges, et al. (2007). "Polyacrylamide hydrogels for cell mechanics: steps toward optimization and alternative uses." Methods Cell Biol **83**: 29-46.
Kass, L., J. T. Erler, et al. (2007). "Mammary epithelial cell: influence of extracellular matrix composition and organization during development and tumorigenesis." Int J Biochem Cell Biol **39**(11): 1987-94.
Katz, B. Z., L. Romer, et al. (2003). "Targeting membrane-localized focal adhesion kinase to focal adhesions: roles of tyrosine phosphorylation and SRC family kinases." J Biol Chem **278**(31): 29115-20.
Katz, B. Z., E. Zamir, et al. (2000). "Physical state of the extracellular matrix regulates the structure and molecular composition of cell-matrix adhesions." Mol Biol Cell **11**(3): 1047-60.
Kaverina, I., O. Krylyshkina, et al. (1999). "Microtubule targeting of substrate contacts promotes their relaxation and dissociation." J Cell Biol **146**(5): 1033-44.
Kellermayer, M. S., S. B. Smith, et al. (1997). "Folding-unfolding transitions in single titin molecules characterized with laser tweezers." Science **276**(5315): 1112-6.
Kiosses, W. B., S. J. Shattil, et al. (2001). "Rac recruits high-affinity integrin alphavbeta3 to lamellipodia in endothelial cell migration." Nat Cell Biol **3**(3): 316-20.
Kiyokawa, E., Y. Hashimoto, et al. (1998). "Activation of Rac1 by a Crk SH3-binding protein, DOCK180." Genes Dev **12**(21): 3331-6.
Kiyokawa, E., Y. Hashimoto, et al. (1998). "Evidence that DOCK180 up-regulates signals from the CrkII-p130(Cas) complex." J Biol Chem **273**(38): 24479-84.
Knight, M. M., T. Toyoda, et al. (2005). "Mechanical compression and hydrostatic pressure induce reversible changes in actin cytoskeletal organisation in chondrocytes in agarose." J Biomech.

Kolega, J. (2004). "Phototoxicity and photoinactivation of blebbistatin in UV and visible light." Biochem Biophys Res Commun **320**(3): 1020-5.
Kong, H. J., T. Boontheekul, et al. (2006). "Quantifying the relation between adhesion ligand-receptor bond formation and cell phenotype." Proc Natl Acad Sci U S A **103**(49): 18534-9.
Kostic, A. and M. P. Sheetz (2006). "Fibronectin rigidity response through Fyn and p130Cas recruitment to the leading edge." Mol Biol Cell **17**(6): 2684-95.
Kovacs, M., J. Toth, et al. (2004). "Mechanism of blebbistatin inhibition of myosin II." J Biol Chem **279**(34): 35557-63.
Kreitzer, G., G. Liao, et al. (1999). "Detyrosination of tubulin regulates the interaction of intermediate filaments with microtubules in vivo via a kinesin-dependent mechanism." Mol Biol Cell **10**(4): 1105-18.
Kwong, L., M. A. Wozniak, et al. (2003). "R-Ras promotes focal adhesion formation through focal adhesion kinase and p130(Cas) by a novel mechanism that differs from integrins." Mol Cell Biol **23**(3): 933-49.
Laukaitis, C. M., D. J. Webb, et al. (2001). "Differential dynamics of alpha 5 integrin, paxillin, and alpha-actinin during formation and disassembly of adhesions in migrating cells." J Cell Biol **153**(7): 1427-40.
Lee, A., S. T. Wong, et al. (1999). "Ca2+/calmodulin binds to and modulates P/Q-type calcium channels." Nature **399**(6732): 155-9.
Lee, C. H., H. J. Shin, et al. (2005). "Nanofiber alignment and direction of mechanical strain affect the ECM production of human ACL fibroblast." Biomaterials **26**(11): 1261-70.
Lee, J., M. Leonard, et al. (1994). "Traction forces generated by locomoting keratocytes." J Cell Biol **127**(6 Pt 2): 1957-64.
Lehenkari, P. P. and M. A. Horton (1999). "Single integrin molecule adhesion forces in intact cells measured by atomic force microscopy." Biochem Biophys Res Commun **259**(3): 645-50.
Lele, T. P., J. Pendse, et al. (2006). "Mechanical forces alter zyxin unbinding kinetics within focal adhesions of living cells." J Cell Physiol **207**(1): 187-94.
Levental, I., P. C. Georges, et al. (2007). "Soft biological materials and their impact on cell function." Soft Matter **3**: 299-306.
Li, S. C., G. F. Chen, et al. (2001). "Altered expression of extracellular matrix and proteinases in Noble rat prostate gland after long-term treatment with sex steroids." Prostate **49**(1): 58-71.
Lim, K. B., W. Bu, et al. (2008). "The Cdc42 effector IRSp53 generates filopodia by coupling membrane protrusion with actin dynamics." J Biol Chem.
Lin, S. X., G. G. Gundersen, et al. (2002). "Export from pericentriolar endocytic recycling compartment to cell surface depends on stable, detyrosinated (glu) microtubules and kinesin." Mol Biol Cell **13**(1): 96-109.
Liu, S., W. B. Kiosses, et al. (2002). "A fragment of paxillin binds the alpha 4 integrin cytoplasmic domain (tail) and selectively inhibits alpha 4-mediated cell migration." J Biol Chem **277**(23): 20887-94.
Lo, C. M., D. B. Buxton, et al. (2004). "Nonmuscle myosin IIb is involved in the guidance of fibroblast migration." Mol Biol Cell **15**(3): 982-9.
Lo, C. M., H. B. Wang, et al. (2000). "Cell movement is guided by the rigidity of the substrate." Biophys J **79**(1): 144-52.
Lochter, A., Z. Werb, et al. (1999). "Transcriptional regulation of stromelysin-1 gene expression is altered during progression of mouse mammary epithelial cells from functionally normal to malignant." Matrix Biol **18**(5): 455-67.
Lu, S., M. Huang, et al. (2000). "Alterations of basement membrane in di-isopropanolnitrosamine-induced carcinogenesis of the rat thyroid gland: an immunohistochemical study." Virchows Arch **436**(6): 595-601.
Maffini, M. V., J. M. Calabro, et al. (2005). "Stromal regulation of neoplastic development: age-dependent normalization of neoplastic mammary cells by mammary stroma." Am J Pathol **167**(5): 1405-10.
Maffini, M. V., A. M. Soto, et al. (2004). "The stroma as a crucial target in rat mammary gland carcinogenesis." J Cell Sci **117**(Pt 8): 1495-502.

Mahaffy, R. E., S. Park, et al. (2004). "Quantitative analysis of the viscoelastic properties of thin regions of fibroblasts using atomic force microscopy." Biophys J **86**(3): 1777-93.
Mahaffy, R. E., C. K. Shih, et al. (2000). "Scanning probe-based frequency-dependent microrheology of polymer gels and biological cells." Phys Rev Lett **85**(4): 880-3.
Maniotis, A. J., C. S. Chen, et al. (1997). "Demonstration of mechanical connections between integrins, cytoskeletal filaments, and nucleoplasm that stabilize nuclear structure." Proc Natl Acad Sci U S A **94**(3): 849-54.
Mansour, H., P. P. de Tombe, et al. (2004). "Restoration of resting sarcomere length after uniaxial static strain is regulated by protein kinase Cepsilon and focal adhesion kinase." Circ Res **94**(5): 642-9.
Marriott, G. and J. Ottl (1998). Synthesis and applications of heterobifunctional photocleavable cross-linking reagents. Methods in Enzymology. San Diego, Academic Press. **291:** 155-175.
Martin, P. (1997). "Wound healing--aiming for perfect skin regeneration." Science **276**(5309): 75-81.
Martines, E., K. McGhee, et al. (2004). "A parallel-plate flow chamber to study initial cell adhesion on a nanofeatured surface." IEEE Trans Nanobioscience **3**(2): 90-5.
Meyer, C. J., F. J. Alenghat, et al. (2000). "Mechanical control of cyclic AMP signalling and gene transcription through integrins." Nat Cell Biol **2**(9): 666-8.
Meyle, J., K. Gultig, et al. (1995). "Variation in contact guidance by human cells on a microstructured surface." J Biomed Mater Res **29**(1): 81-8.
Miki, H., H. Yamaguchi, et al. (2000). "IRSp53 is an essential intermediate between Rac and WAVE in the regulation of membrane ruffling." Nature **408**(6813): 732-5.
Mitra, S. K., D. A. Hanson, et al. (2005). "Focal adhesion kinase: in command and control of cell motility." Nat Rev Mol Cell Biol **6**(1): 56-68.
Morariu, M. D., N. E. Voicu, et al. (2003). "Hierarchical structure formation and pattern replication induced by an electric field." Nat Mater **2**(1): 48-52.
Munevar, S., Y. Wang, et al. (2001). "Traction force microscopy of migrating normal and H-ras transformed 3T3 fibroblasts." Biophys J **80**(4): 1744-57.
Munevar, S., Y. L. Wang, et al. (2001). "Distinct roles of frontal and rear cell-substrate adhesions in fibroblast migration." Mol Biol Cell **12**(12): 3947-54.
Nakamura, K., H. Yano, et al. (2000). "Tyrosine phosphorylation of paxillin alpha is involved in temporospatial regulation of paxillin-containing focal adhesion formation and F-actin organization in motile cells." J Biol Chem **275**(35): 27155-64.
Nelson, C. M. and C. S. Chen (2003). "VE-cadherin simultaneously stimulates and inhibits cell proliferation by altering cytoskeletal structure and tension." J Cell Sci **116**(Pt 17): 3571-81.
Nix, D. A. and M. C. Beckerle (1997). "Nuclear-cytoplasmic shuttling of the focal contact protein, zyxin: a potential mechanism for communication between sites of cell adhesion and the nucleus." J Cell Biol **138**(5): 1139-47.
Nobes, C. D. and A. Hall (1999). "Rho GTPases control polarity, protrusion, and adhesion during cell movement." J Cell Biol **144**(6): 1235-44.
Olaso, E., C. Salado, et al. (2003). "Proangiogenic role of tumor-activated hepatic stellate cells in experimental melanoma metastasis." Hepatology **37**(3): 674-85.
Ookawa, K., M. Sato, et al. (1993). "Morphological changes of endothelial cells after exposure to fluid-imposed shear stress: differential responses induced by extracellular matrices." Biorheology **30**(2): 131-40.
O'Toole, T. E., J. Ylanne, et al. (1995). "Regulation of integrin affinity states through an NPXY motif in the beta subunit cytoplasmic domain." J Biol Chem **270**(15): 8553-8.
Owen, J. D., P. J. Ruest, et al. (1999). "Induced focal adhesion kinase (FAK) expression in FAK-null cells enhances cell spreading and migration requiring both auto- and activation loop phosphorylation sites and inhibits adhesion-dependent tyrosine phosphorylation of Pyk2." Mol Cell Biol **19**(7): 4806-18.
Owens, L. V., L. Xu, et al. (1995). "Overexpression of the focal adhesion kinase (p125FAK) in invasive human tumors." Cancer Res **55**(13): 2752-5.

Padera, T. P., B. R. Stoll, et al. (2004). "Pathology: cancer cells compress intratumour vessels." Nature **427**(6976): 695.
Palazzo, A. F., C. H. Eng, et al. (2004). "Localized stabilization of microtubules by integrin- and FAK-facilitated Rho signaling." Science **303**(5659): 836-9.
Parsons, J. T. (1996). "Integrin-mediated signalling: regulation by protein tyrosine kinases and small GTP-binding proteins." Curr Opin Cell Biol **8**(2): 146-52.
Parsons, J. T. (2003). "Focal adhesion kinase: the first ten years." J Cell Sci **116**(Pt 8): 1409-16.
Paszek, M. J. and V. M. Weaver (2004). "The tension mounts: mechanics meets morphogenesis and malignancy." J Mammary Gland Biol Neoplasia **9**(4): 325-42.
Paszek, M. J., N. Zahir, et al. (2005). "Tensional homeostasis and the malignant phenotype." Cancer Cell **8**(3): 241-54.
Pelham, R. J., Jr. and Y. Wang (1997). "Cell locomotion and focal adhesions are regulated by substrate flexibility." Proc Natl Acad Sci U S A **94**(25): 13661-5.
Pelham, R. J., Jr. and Y. Wang (1999). "High resolution detection of mechanical forces exerted by locomoting fibroblasts on the substrate." Mol Biol Cell **10**(4): 935-45.
Petch, L. A., S. M. Bockholt, et al. (1995). "Adhesion-induced tyrosine phosphorylation of the p130 src substrate." J Cell Sci **108 (Pt 4)**: 1371-9.
Polte, T. R. and S. K. Hanks (1995). "Interaction between focal adhesion kinase and Crk-associated tyrosine kinase substrate p130Cas." Proc Natl Acad Sci U S A **92**(23): 10678-82.
Ponniah, S., D. Z. Wang, et al. (1999). "Targeted disruption of the tyrosine phosphatase PTPalpha leads to constitutive downregulation of the kinases Src and Fyn." Curr Biol **9**(10): 535-8.
Pool, R. (1988). "Trapping with optical tweezers." Science **241**(4869): 1042.
Radmacher, M. (2007). "Studying the mechanics of cellular processes by atomic force microscopy." Methods Cell Biol **83**: 347-72.
Radmacher, M., M. Fritz, et al. (1996). "Measuring the viscoelastic properties of human platelets with the atomic force microscope." Biophys J **70**(1): 556-67.
Rajagopalan, P., W. A. Marganski, et al. (2004). "Direct comparison of the spread area, contractility, and migration of balb/c 3T3 fibroblasts adhered to fibronectin- and RGD-modified substrata." Biophys J **87**(4): 2818-27.
Ren, X. D., W. B. Kiosses, et al. (2000). "Focal adhesion kinase suppresses Rho activity to promote focal adhesion turnover." J Cell Sci **113 (Pt 20)**: 3673-8.
Rhee, S., H. Jiang, et al. (2007). "Microtubule function in fibroblast spreading is modulated according to the tension state of cell-matrix interactions." Proc Natl Acad Sci U S A **104**(13): 5425-30.
Richert, L., A. J. Engler, et al. (2004). "Elasticity of native and cross-linked polyelectrolyte multilayer films." Biomacromolecules **5**(5): 1908-16.
Ridley, A. J. and A. Hall (1992). "The small GTP-binding protein rho regulates the assembly of focal adhesions and actin stress fibers in response to growth factors." Cell **70**(3): 389-99.
Ridley, A. J., H. F. Paterson, et al. (1992). "The small GTP-binding protein rac regulates growth factor-induced membrane ruffling." Cell **70**(3): 401-10.
Rief, M., M. Gautel, et al. (2000). "Unfolding forces of titin and fibronectin domains directly measured by AFM." Adv Exp Med Biol **481**: 129-36; discussion 137-41.
Rief, M., M. Gautel, et al. (1997). "Reversible unfolding of individual titin immunoglobulin domains by AFM." Science **276**(5315): 1109-12.
Riveline, D., E. Zamir, et al. (2001). "Focal contacts as mechanosensors: externally applied local mechanical force induces growth of focal contacts by an mDia1-dependent and ROCK-independent mechanism." J Cell Biol **153**(6): 1175-86.
Rotsch, C., K. Jacobson, et al. (1999). "Dimensional and mechanical dynamics of active and stable edges in motile fibroblasts investigated by using atomic force microscopy." Proc Natl Acad Sci U S A **96**(3): 921-6.
Rotsch, C. and M. Radmacher (2000). "Drug-induced changes of cytoskeletal structure and mechanics in fibroblasts: an atomic force microscopy study." Biophys J **78**(1): 520-35.

Rottner, K., A. Hall, et al. (1999). "Interplay between Rac and Rho in the control of substrate contact dynamics." Curr Biol **9**(12): 640-8.
Rottner, K., M. Krause, et al. (2001). "Zyxin is not colocalized with vasodilator-stimulated phosphoprotein (VASP) at lamellipodial tips and exhibits different dynamics to vinculin, paxillin, and VASP in focal adhesions." Mol Biol Cell **12**(10): 3103-13.
Rovin, J. D., H. F. Frierson, Jr., et al. (2002). "Expression of focal adhesion kinase in normal and pathologic human prostate tissues." Prostate **53**(2): 124-32.
Saez, A., A. Buguin, et al. (2005). "Is the mechanical activity of epithelial cells controlled by deformations or forces?" Biophys J **89**(6): L52-4.
Sakai, R., A. Iwamatsu, et al. (1994). "A novel signaling molecule, p130, forms stable complexes in vivo with v-Crk and v-Src in a tyrosine phosphorylation-dependent manner." Embo J **13**(16): 3748-56.
Sakamoto, T., J. Limouze, et al. (2005). "Blebbistatin, a myosin II inhibitor, is photoinactivated by blue light." Biochemistry **44**(2): 584-8.
Sandquist, J. C., K. I. Swenson, et al. (2006). "Rho kinase differentially regulates phosphorylation of nonmuscle myosin II isoforms A and B during cell rounding and migration." J Biol Chem **281**(47): 35873-83.
Sawada, Y. and M. P. Sheetz (2002). "Force transduction by Triton cytoskeletons." J Cell Biol **156**(4): 609-15.
Schaffer, E., T. Thurn-Albrecht, et al. (2000). "Electrically induced structure formation and pattern transfer." Nature **403**(6772): 874-7.
Schaller, M. D., J. D. Hildebrand, et al. (1999). "Complex formation with focal adhesion kinase: A mechanism to regulate activity and subcellular localization of Src kinases." Mol Biol Cell **10**(10): 3489-505.
Schaller, M. D. and J. T. Parsons (1995). "pp125FAK-dependent tyrosine phosphorylation of paxillin creates a high-affinity binding site for Crk." Mol Cell Biol **15**(5): 2635-45.
Schindler, M., I. Ahmed, et al. (2005). "A synthetic nanofibrillar matrix promotes in vivo-like organization and morphogenesis for cells in culture." Biomaterials **26**(28): 5624-31.
Schlaepfer, D. D., S. K. Hanks, et al. (1994). "Integrin-mediated signal transduction linked to Ras pathway by GRB2 binding to focal adhesion kinase." Nature **372**(6508): 786-91.
Schlaepfer, D. D., K. C. Jones, et al. (1998). "Multiple Grb2-mediated integrin-stimulated signaling pathways to ERK2/mitogen-activated protein kinase: summation of both c-Src- and focal adhesion kinase-initiated tyrosine phosphorylation events." Mol Cell Biol **18**(5): 2571-85.
Schlunck, G., H. Han, et al. (2008). "Substrate rigidity modulates cell matrix interactions and protein expression in human trabecular meshwork cells." Invest Ophthalmol Vis Sci **49**(1): 262-9.
Shahin, V. and N. P. Barrera (2008). "Providing unique insight into cell biology via atomic force microscopy." Int Rev Cytol **265**: 227-52.
Shi, Q. and D. Boettiger (2003). "A novel mode for integrin-mediated signaling: tethering is required for phosphorylation of FAK Y397." Mol Biol Cell **14**(10): 4306-15.
Shoelson, B., E. K. Dimitriadis, et al. (2004). "Evidence and implications of inhomogeneity in tectorial membrane elasticity." Biophys J **87**(4): 2768-77.
Singhvi, R., A. Kumar, et al. (1994). "Engineering cell shape and function." Science **264**(5159): 696-8.
Sneddon, I. N. (1965). "The relation between load and penetration in the axisymmetric Boussinesq problem for a punch of arbitrary profile." Int J Eng Sci **3**: 47-57.
Solon, J., I. Levental, et al. (2007). "Fibroblast adaptation and stiffness matching to soft elastic substrates." Biophys J **93**(12): 4453-61.
Steinberg, M. S. and P. M. McNutt (1999). "Cadherins and their connections: adhesion junctions have broader functions." Curr Opin Cell Biol **11**(5): 554-60.
Sternlicht, M. D., M. J. Bissell, et al. (2000). "The matrix metalloproteinase stromelysin-1 acts as a natural mammary tumor promoter." Oncogene **19**(8): 1102-13.
Sternlicht, M. D., A. Lochter, et al. (1999). "The stromal proteinase MMP3/stromelysin-1 promotes mammary carcinogenesis." Cell **98**(2): 137-46.

Straight, A. F., A. Cheung, et al. (2003). "Dissecting temporal and spatial control of cytokinesis with a myosin II Inhibitor." Science **299**(5613): 1743-7.
Stupack, D. G. and D. A. Cheresh (2002). "Get a ligand, get a life: integrins, signaling and cell survival." J Cell Sci **115**(Pt 19): 3729-38.
Su, J., M. Muranjan, et al. (1999). "Receptor protein tyrosine phosphatase alpha activates Src-family kinases and controls integrin-mediated responses in fibroblasts." Curr Biol **9**(10): 505-11.
Sun, Z., L. A. Martinez-Lemus, et al. (2008). "Extracellular Matrix Specific Focal Adhesions in Vascular Smooth Muscle Produce Mechanically Active Adhesion Sites." Am J Physiol Cell Physiol.
Sy, S. M., P. B. Lai, et al. (2006). "Novel identification of zyxin upregulations in the motile phenotype of hepatocellular carcinoma." Mod Pathol **19**(8): 1108-16.
Tachibana, K., T. Urano, et al. (1997). "Tyrosine phosphorylation of Crk-associated substrates by focal adhesion kinase. A putative mechanism for the integrin-mediated tyrosine phosphorylation of Crk-associated substrates." J Biol Chem **272**(46): 29083-90.
Takeichi, M. (1995). "Morphogenetic roles of classic cadherins." Curr Opin Cell Biol **7**(5): 619-27.
Tamada, M., M. P. Sheetz, et al. (2004). "Activation of a signaling cascade by cytoskeleton stretch." Dev Cell **7**(5): 709-18.
Tan, J. L., J. Tien, et al. (2003). "Cells lying on a bed of microneedles: an approach to isolate mechanical force." Proc Natl Acad Sci U S A **100**(4): 1484-9.
Tang, D., D. Mehta, et al. (1999). "Mechanosensitive tyrosine phosphorylation of paxillin and focal adhesion kinase in tracheal smooth muscle." Am J Physiol **276**(1 Pt 1): C250-8.
Taylor, J. R. (1997). An Introduction to Error Analysis, The study of Uncertainties in Physical Measurements. Sausalito, CA, University Science Books.
Thoreson, E. and N. Burnham (2004). "Standard-Deviation Minimization for Calibrating the Radii of Spheres Attached to AFM Cantilevers." Rev. Sci. Instruments **75**: 1359-1362.
Tilghman, R. W., J. K. Slack-Davis, et al. (2005). "Focal adhesion kinase is required for the spatial organization of the leading edge in migrating cells." J Cell Sci **118**(Pt 12): 2613-23.
Tremblay, L., W. Hauck, et al. (1996). "Focal adhesion kinase (pp125FAK) expression, activation and association with paxillin and p50CSK in human metastatic prostate carcinoma." Int J Cancer **68**(2): 164-71.
Tsai, I. Y., A. J. Crosby, et al. (2007). "Surface patterning." Methods Cell Biol **83**: 67-87.
Turner, A. M., N. Dowell, et al. (2000). "Attachment of astroglial cells to microfabricated pillar arrays of different geometries." J Biomed Mater Res **51**(3): 430-41.
Uttayarat, P., G. K. Toworfe, et al. (2005). "Topographic guidance of endothelial cells on silicone surfaces with micro- to nanogrooves: orientation of actin filaments and focal adhesions." J Biomed Mater Res A **75**(3): 668-80.
van Kooten, T. G. and A. F. von Recum (1999). "Cell adhesion to textured silicone surfaces: the influence of time of adhesion and texture on focal contact and fibronectin fibril formation." Tissue Eng **5**(3): 223-40.
Vasiliev, J. M. (1958). "The role of connective tissue proliferation in invasive growth of normal and malignant tissues: a review." Br J Cancer **12**(4): 524-36.
Vogel, V. and M. Sheetz (2006). "Local force and geometry sensing regulate cell functions." Nat Rev Mol Cell Biol **7**(4): 265-75.
von Wichert, G., B. Haimovich, et al. (2003). "Force-dependent integrin-cytoskeleton linkage formation requires downregulation of focal complex dynamics by Shp2." Embo J **22**(19): 5023-35.
von Wichert, G., G. Jiang, et al. (2003). "RPTP-alpha acts as a transducer of mechanical force on alphav/beta3-integrin-cytoskeleton linkages." J Cell Biol **161**(1): 143-53.
Vuori, K., H. Hirai, et al. (1996). "Introduction of p130cas signaling complex formation upon integrin-mediated cell adhesion: a role for Src family kinases." Mol Cell Biol **16**(6): 2606-13.
Walboomers, X. F., W. Monaghan, et al. (1999). "Attachment of fibroblasts on smooth and microgrooved polystyrene." J Biomed Mater Res **46**(2): 212-20.
Wang, H. B., M. Dembo, et al. (2001). "Focal adhesion kinase is involved in mechanosensing during fibroblast migration." Proc Natl Acad Sci U S A **98**(20): 11295-300.

Wang, H. B., M. Dembo, et al. (2000). "Substrate flexibility regulates growth and apoptosis of normal but not transformed cells." Am J Physiol Cell Physiol **279**(5): C1345-50.
Wang, N., J. P. Butler, et al. (1993). "Mechanotransduction across the cell surface and through the cytoskeleton." Science **260**(5111): 1124-7.
Wang, N. and D. E. Ingber (1994). "Control of cytoskeletal mechanics by extracellular matrix, cell shape, and mechanical tension." Biophys J **66**(6): 2181-9.
Wang, Y.-L. and R. J. Pelham Jr. (1998). Preparation of a Flexible, Porous Polyacrylamide Substrate for Mechanical Studies of Cultured Cells. Methods in Enzymology, Academic Press. **298:** 489-496.
Weiner, T. M., E. T. Liu, et al. (1994). "Expression of growth factor receptors, the focal adhesion kinase, and other tyrosine kinases in human soft tissue tumors." Ann Surg Oncol **1**(1): 18-27.
Weisenhorn, A. L., P. K. Hansma, et al. (1989). "Forces in atomic force microscopy in air and water." Appl Phys Lett **54**: 2651-2653.
Weiss, P. (1941). Nerve patterns: the mechanics of nerve growth. Third Growth Symposium.
Weiss, P. (1945). "Experiments on cell and axon orientation in vitro: The role of colloidal exudates in tissue organization." J Exp Zool **100**: 353-386.
Wessels, D., D. R. Soll, et al. (1988). "Cell motility and chemotaxis in Dictyostelium amebae lacking myosin heavy chain." Dev Biol **128**(1): 164-77.
White, C. R., M. Haidekker, et al. (2001). "Temporal gradients in shear, but not spatial gradients, stimulate endothelial cell proliferation." Circulation **103**(20): 2508-13.
Wierzbicka-Patynowski, I. and J. E. Schwarzbauer (2003). "The ins and outs of fibronectin matrix assembly." J Cell Sci **116**(Pt 16): 3269-76.
Wiseman, B. S. and Z. Werb (2002). "Stromal effects on mammary gland development and breast cancer." Science **296**(5570): 1046-9.
Wittelsberger, S. C., K. Kleene, et al. (1981). "Progressive loss of shape-responsive metabolic controls in cells with increasingly transformed phenotype." Cell **24**(3): 859-66.
Wojciak-Stothard, B., Z. Madeja, et al. (1995). "Activation of macrophage-like cells by multiple grooved substrata. Topographical control of cell behaviour." Cell Biol Int **19**(6): 485-90.
Wong, J. Y., J. B. Leach, et al. (2004). "Balance of chemistry, topography, and mechanics at the cell-biomaterial interface: Issues and challenges for assessing the role of substrate mechanics on cell response." Surface Science **570**: 119-133.
Wozniak, M. A., R. Desai, et al. (2003). "ROCK-generated contractility regulates breast epithelial cell differentiation in response to the physical properties of a three-dimensional collagen matrix." J Cell Biol **163**(3): 583-95.
Wozniak, M. A. and P. J. Keely (2005). "Use of three-dimensional collagen gels to study mechanotransduction in T47D breast epithelial cells." Biol Proced Online **7**: 144-61.
Wozniak, M. A., K. Modzelewska, et al. (2004). "Focal adhesion regulation of cell behavior." Biochim Biophys Acta **1692**(2-3): 103-119.
Wynn, T. A. (2008). "Cellular and molecular mechanisms of fibrosis." J Pathol **214**(2): 199-210.
Xia, H., R. S. Nho, et al. (2004). "Focal adhesion kinase is upstream of phosphatidylinositol 3-kinase/Akt in regulating fibroblast survival in response to contraction of type I collagen matrices via a beta 1 integrin viability signaling pathway." J Biol Chem **279**(31): 33024-34.
Yano, Y., J. Geibel, et al. (1996). "Tyrosine phosphorylation of pp125FAK and paxillin in aortic endothelial cells induced by mechanical strain." Am J Physiol **271**(2 Pt 1): C635-49.
Yeung, T., P. C. Georges, et al. (2005). "Effects of substrate stiffness on cell morphology, cytoskeletal structure, and adhesion." Cell Motil Cytoskeleton **60**(1): 24-34.
Yi, J., S. Kloeker, et al. (2002). "Members of the Zyxin family of LIM proteins interact with members of the p130Cas family of signal transducers." J Biol Chem **277**(11): 9580-9.
Ylanne, J., Y. Chen, et al. (1993). "Distinct functions of integrin alpha and beta subunit cytoplasmic domains in cell spreading and formation of focal adhesions." J Cell Biol **122**(1): 223-33.
Yoffe, E. H. (1984). "Modified Hertz theory for spherical indentation." Philosophical Magazine A **50**(6): 813-828.

Yoshigi, M., L. M. Hoffman, et al. (2005). "Mechanical force mobilizes zyxin from focal adhesions to actin filaments and regulates cytoskeletal reinforcement." J Cell Biol **171**(2): 209-15.
Zaidel-Bar, R., C. Ballestrem, et al. (2003). "Early molecular events in the assembly of matrix adhesions at the leading edge of migrating cells." J Cell Sci **116**(Pt 22): 4605-13.
Zamir, E. and B. Geiger (2001). "Molecular complexity and dynamics of cell-matrix adhesions." J Cell Sci **114**(Pt 20): 3583-90.
Zamir, E., M. Katz, et al. (2000). "Dynamics and segregation of cell-matrix adhesions in cultured fibroblasts." Nat Cell Biol **2**(4): 191-6.
Zhai, J., H. Lin, et al. (2003). "Direct interaction of focal adhesion kinase with p190RhoGEF." J Biol Chem **278**(27): 24865-73.
Zhao, S., A. Suciu, et al. (1995). "Synergistic effects of fluid shear stress and cyclic circumferential stretch on vascular endothelial cell morphology and cytoskeleton." Arterioscler Thromb Vasc Biol **15**(10): 1781-6.
Zhao, Y. P., X. Shi, et al. (2003). "Effect of work of adhesion on nanoindentation." Rev. Adv. Mater. Sci. **5**: 348-353.
Zheng, X. M., R. J. Resnick, et al. (2000). "A phosphotyrosine displacement mechanism for activation of Src by PTPalpha." Embo J **19**(5): 964-78.
Zheng, X. M., Y. Wang, et al. (1992). "Cell transformation and activation of pp60c-src by overexpression of a protein tyrosine phosphatase." Nature **359**(6393): 336-9.
Zhong, C., M. Chrzanowska-Wodnicka, et al. (1998). "Rho-mediated contractility exposes a cryptic site in fibronectin and induces fibronectin matrix assembly." J Cell Biol **141**(2): 539-51.
Zhong, C., M. S. Kinch, et al. (1997). "Rho-stimulated contractility contributes to the fibroblastic phenotype of Ras-transformed epithelial cells." Mol Biol Cell **8**(11): 2329-44.
Zimmerberg, J. and S. McLaughlin (2004). "Membrane curvature: how BAR domains bend bilayers." Curr Biol **14**(6): R250-2.
Zinger, O., K. Anselme, et al. (2004). "Time-dependent morphology and adhesion of osteoblastic cells on titanium model surfaces featuring scale-resolved topography." Biomaterials **25**(14): 2695-711.

APPENDICES

Appendix 1. Matlab code for solving E from force-indentation profiles obtained with AFM

```
%% AFMModulusSolver_Master file last edited on 03/02/07 by M.T. Frey.
%% Imports AFM data and solves for Young's modulus values for either
%% spherical or conical tips over set and automatically determined ROA
%% (Range of analysis).

%% Instructions for use:
%% Change settings on lines 24-27, enter number of datasets for analysis
%% on line 32 and change data information in Part Ib on line 39 accordingly.
%% NOTE: If you use this algorithm for your data analysis, please acknowledge
%% accordingly.

%% Part Ia.  Algorithm settings and data input
%%%%%%%%%%%%%%%%%%%%%%%%%%%%%%%%%%%%%%%%%%%
%%%%%%%%%%%%%%%%%%%%%%%%%%%%%%%

%% Start of algorithm clears all history and defines formal and variables
%% used in other subalgorithms
   clc; clear all; close all;
   format long;
   global start_point s c del_sphere logF_sphere del_cone logF_cone k del_punch Es v
del2 logF_punch;
%%  Settings on data collection (do not change these without first consulting NA
Burnham)
   VoverN=1.0;
   caliberror=0.0;
%% Settings on compilation file names for figures and data exporting
   cantilever = 'Spherical_';
   sampletype = '5_010_';
   v=0.45;
   save=1; % enter 0 for no for quick peek at data, enter 1 to save all images and data
%% Settings on range of analysis (ROA), or range of del over which data will be
analyzed
   ROAstart=10;%set this to 10 for best results
   ROAend=50;%set this to 50 for best results
%% Settings on samples to be compiled
   datasets=14; % equals number of samples;
%% Data sets to compile, note that settings for tip information only needs
%% to be entered on the first set as long as the settings are the same on
```

```
%% subsequent data sets, else enter the new values where needed.
   dataindex=1;
   for dataindex=1:datasets;
     if (dataindex==1);
         shape=1; %enter 1 for sphere, 2 for cone
         sample_thickness=150000; % estimated based on volume addition
         frequency=1; %value in Hz of sampling rate
         probe=1;%'DNP_5micron';
         k=0.0503;
         r=2.5725*1E3; %in nm, find accurate number from calibration
         test = '101005_010_1_a1';
     elseif (dataindex==2);
         test = '101005_010_1_a3';
     elseif (dataindex==3);
         test = '101005_010_1_c1';
     elseif (dataindex==4);
         test = '101005_010_1_c2';
     elseif (dataindex==5);
         test = '101005_010_1_c3';
     elseif (dataindex==6);
         test = '101005_010_1_f1';
     elseif (dataindex==7);
         test = '101005_010_1_h1';
     elseif (dataindex==8);
         test = '101005_010_1_l1';
     elseif (dataindex==9);
         test = '101005_010_1_l2';
     elseif (dataindex==10);
         test = '101005_010_1_l3';
     elseif (dataindex==11);
         test = '101005_010_1_m2';
     elseif (dataindex==12);
         shape=1;
         sample_thickness=150000; % estimated based on volume addition
         frequency=1; %value in Hz of sampling rate
         probe=3;%'?';
         k=0.087;
         r=2.4925*1E3;
         test = '102505_010_1_c1';
     elseif (dataindex==13);
         shape=1;
         sample_thickness=150000; % estimated based on volume addition
         frequency=1; %value in Hz of sampling rate
```

```
    probe=2;%'Dlever';
    k=0.212;
    r=10.04*1E3;
    test = '111805_100_1_b100';
  elseif (dataindex==14);
    test = '111805_100_1_a100';
  end;

%% Part II.  Converts all positive and non-linear raw data to usable F-del data
%%%%%%%%%%%%%%%%%%%%%%%%%%%%%%%%%%%%%%%%%%%%%%%%%%%%%%%%%%%%%%%%%%%%%%%%%%%%
%%%%%%%%%%%%%%%%%%%%%%%%%%%%%%%%%%%%%%%%%%%%%%%%%%%%%%%%%%%%%%%%%%%%%%%%%%%%

%% Loads file names and data for each data set to label saved files accordingly
  extension = '.txt';
  name=[test,extension];
  data=dlmread(name,' ',3,0);
%% Assigns specific portions of raw data just imported to the variables for
%% force and displacement for both retraction and approach curves:
  AppDis=data(:,2);
  AppForce=data(:,3);
  RetDis=data(:,5);
  RetForce=data(:,6);
%% Semi-converted values:
  d0r=1E9/k/VoverN*RetForce;
  z0r=RetDis*1000;
  del0r=RetDis*1000+d0r*(1-caliberror/100);
  F0r=k*d0r;
  d0a=1E9/k/VoverN*AppForce;
  z0a=AppDis*1000;
  del0a=AppDis*1000+d0a*(1-caliberror/100);
  F0a=k*d0a;
%% Plots Raw Data offset to zero and cropped between zero and maximum of
%% non-linear data, with red approach curve, blue retraction curve:
  figure;
  subplot(3,1,1);
  plot(z0a,d0a,'r',z0r,d0r,'b');
  legend('approach','retraction',1);
  legend('boxoff');
  xlabel('Scanner Position (nm)');
  ylabel('Deflection (nm)');
  title('Raw Data');
%% The following calculates the zero offset for the curve such that there
%% can be only one change in slope to occur at the contact point.  This will
```

```
%% be double checked visually on the plotted curves.
   a=1;
   slope=0;
   zerodel=0;
   zeroF=0;
   while slope==0;
      slope=F0r(4+a)-F0r(a);
      zerodel=z0r(3+a);
      zeroF=F0r(3+a);
      a=a+1;
   end;
   deloff=-zerodel;
   Foff=-zeroF;
   da=(1E9*AppForce+Foff)/k/VoverN;
   za=(z0a+deloff);
   dela=-(z0a+da*(1-(caliberror/100))+deloff);
   Fa=da*k;
   d=(1E9*RetForce+Foff)/k/VoverN;
   z=(z0r+deloff);
   del=-(z0r+d*(1-(caliberror/100))+deloff);
   F=d*k;
%% Removes all data where del < 0 for analysis
   index=find(del>0);
   start=min(index);
   del(1:start,:)=[];
   F(1:start,:)=[];
   dela(1:start,:)=[];
   Fa(1:start,:)=[];
   z(1:start,:)=[];
   d(1:start,:)=[];
   za(1:start,:)=[];
   da(1:start,:)=[];
   [sizea,sizeb]=size(del);

%% Removes linear (equilibrium) portion at upper portion of curve (from z-d curve), if it
exists
   [bb,cc]=size(d);
   if bb>3;
      g=bb;
      p=4;
      change=d(p)-d(p-3);
      stop=p;
      for p=4:g-1;
```

```
        if (change > 0);
            p=p+1;
            change=d(p)-d(p-3);
            stop=p-2;
        else end;
    end;
    if (stop < bb);
        del(stop:g,:)=[];
        F(stop:g,:)=[];
        dela(stop:g,:)=[];
        Fa(stop:g,:)=[];
        z(stop:g,:)=[];
        d(stop:g,:)=[];
        za(stop:g,:)=[];
        da(stop:g,:)=[];
    else end;
else end;

%% Part IIa. Trims data to portion between user defined range of analysis values for
%% del (ROAstart to ROAend).
%%%%%%%%%%%%%%%%%%%%%%%%%%%%%%%%%%%%%%%%%%%%%%%%%%%%%%%%%%%%%%%%%%%%%%%%%%%%%%%
%%%%%%%%%%%%%%%%%%%%%%%%%%%%%%%%%%%%%%%%%%%%%%%%%%%%%%%%%%%%%%%%%%%%%%%%%%%%%%%

%% If the ROAend chosen exceeds the maximum del, this resets the
%% ROAend to the index at the maximum value of del for analysis only.
%% Of interest will be del0 and F0, the offset and trimmed retraction data.
index=find(del>ROAstart);
start2=min(index);
index2=find(del==max(del));
%% Sets condition that if the ROAend chosen is larger than the size of
%% the data, this sets the last data point as the end for analysis
    if (ROAend > del(index2));
        stop2=index2;
        d0=d(start2:stop2);
        d0a=da(start2:stop2);
        z0=z(start2:stop2);
        z0a=za(start2:stop2);
        del0=del(start2:stop2);
        del0a=dela(start2:stop2);
        F0=F(start2:stop2);
        F0a=Fa(start2:stop2);
    else;
        index2=find(del>ROAend);
```

```
        stop2=min(index2);
        d0=d(start2:stop2);
        d0a=da(start2:stop2);
        z0=z(start2:stop2);
        z0a=za(start2:stop2);
        del0=del(start2:stop2);
        del0a=dela(start2:stop2);
        F0=F(start2:stop2);
        F0a=Fa(start2:stop2);
    end;

%% Kicks out linear data (i.e. those data sets with less than 10 data
%% points)
  if max(del) < min(del0);
    display('Poor Sample Data');
    subplot(3,1,3);
    title('Poor Sample Data');
  else;
    [cc,dd]=size(del0);
    if (cc < 10);
      display('Linear Data');
      subplot(3,1,3);
      title('Linear Data');
    else;

%% Analysis for Spherical Tips
%%%%%%%%%%%%%%%%%%%%%%%%%%%%%%%%%%%%%%%%%%%%%%%%%%%%%%%%%%%%%%%%%%%%%%%
%%%%%%%%%%%%%%%%%%%%%%%%%%%%%%%%%%%%%%%%%%%%%%%%%%%%%%%%%%%%%%%%%%%%%%%

%% Part IIIa. Fits all user defined (set) ROA data to Hertz Sphere Model
%% or deletes linear data.
  if (shape==1);
    s=3/4*(1-v^2)/(r^0.5);
    del_sphere=del0;
    del0_sphere=del0;
    F_sphere=F0;
    F0_sphere=F0;
    del032=del_sphere.^1.5;
    E0=s*F_sphere./del032;
    logF_sphere=log10(F_sphere);
    start_point=E0(1);
    [estimates,modelsphere] = FitHertzSphere_MSI(logF_sphere,start_point);
    E0s=estimates; % GPa
```

```
      F0s=E0s*del032./s;
      logFs0=log10(F0s);
%% Calculates correlation between F_sphere (data) and F0s (model) for set ROA
      R = corrcoef(F_sphere,F0s);
      R2_FF0s=R(1,2);
%% Determines difference between data and model for ALL data
      Fs_all=E0s*del.^1.5/s;
      logFs_all=log10(Fs_all);
      logF=log10(F);
      logFs_diff_all=logFs_all-logF;
%% Finds all data points where the model and data compare (indexaa) within the
%% set condition by using binary numbers (1 if it fits, 0 if it does not)
      [aa,bb]=size(logFs_diff_all);
      eval=zeros(size(logFs_diff_all));
      m=1;
      condition=0.05; % this value appears to be optimal
      for m=1:aa;
         if abs(logFs_diff_all(m)) < condition;
         eval(m)=1;
         else eval(m)=0;
         end;
      m=m+1;
      end;
%% Yields data indices of values for which the model fits within the condition
      indexaa=find(eval==max(eval));
      [cc,dd]=size(indexaa);
%% Kicks out linear data (i.e. those data sets with less than 10 points
%% that fit the model within the criterion)
   if (cc < 10);
      display('Poor Fit to Model, Data Not Analyzed');
      subplot(3,1,3);
      title('Poor Fit to Model, Data Not Analyzed');
   else;

%% Part IIIb. Determines ROA automatically based on where the model and data
compare well
%%%%%%%%%%%%%%%%%%%%%%%%%%%%%%%%%%%%%%%%%%%%%%%%%%%%%%%%%%%%%%%%%%%%%%%%
%%%%%%%%%%%%%%%%%%%%%%%%%%%%%%%%%%%%%%%%%%%%%%%%%%%%%%%%%%%%%%%%%%%%%%%%

%% Designates the upper and lower values as those of the automatically
%% determined ROA for the spherical fit
      startsphere_auto=indexaa(1);
      stopsphere_auto=indexaa(cc);
```

```
%% Assigns lower index values to fit the punch model
    startpunch_auto=1;
    if indexaa(1)>1;
       stoppunch_auto=indexaa(1)-1;
    else;
       stoppunch_auto=1;
    end;
%% Finds the highest index between the set and auto ROAs to set the upper
%% point for plotting
    maxvalue=max([stop2,stopsphere_auto]);
%% Resizes F, del data to plot up to the maximum value between the two
%% sets of data
    deldata=del(1:maxvalue);
    Fdata=F(1:maxvalue);
%% Calculates discrete values of E for all data considered
    del32=deldata.^1.5;
    E=s*Fdata./del32;

%% Part IV. Fits the automatically determined ROA to the spherical model
%% and assigns lower data to the punch data and fits it to the punch model.
%%%%%%%%%%%%%%%%%%%%%%%%%%%%%%%%%%%%%%%%%%%%%%%%%%%%%%%%%%%%%%%%%%%%%%%
%%%%%%%%%%%%%%%%%%%%%%%%%%%%%%%%%%%%%%%%%%%%%%%%%%%%%%%%%%%%%%%%%%%%%%%
    del_punch=del(startpunch_auto:stoppunch_auto);
    F_punch=F(startpunch_auto:stoppunch_auto);
    del_sphere=del(startsphere_auto:stopsphere_auto);
    F_sphere=F(startsphere_auto:stopsphere_auto);
    ROAstart_auto=del(startsphere_auto);
    ROAend_auto=del(stopsphere_auto);
%% Fits respective data set to either the Hertz Sphere Model to solve
%% for E or the model for a Punch to solve for the respective punch radius
    %% Spherical data
       logF_sphere=log10(F_sphere);
       start_point=mean(E0);
       [estimates,modelsphere] = FitHertzSphere_MSI(logF_sphere,start_point);
       Es=estimates;
       Fs=Es*del_sphere.^1.5/s;
       Fs_all=Es*deldata.^1.5/s;
       logFs=log10(Fs);
    %% Calculates correlation between F (data) and Fs (model)
       R = corrcoef(F_sphere,Fs);
       R2_FFs=R(1,2);
    %% Punch data
       PunchRadius=r/20;
```

```
            logF_punch=log10(F_punch);
            start_point=PunchRadius;
            [estimates,modelpunch] = FitPunch_MSI(logF_punch,start_point);
            PunchRadius=estimates;
            Fp=2*Es/(1-v^2)*del_punch.*PunchRadius;
        %% Calculates F_punch over larger data set of del to see more clearly on plot
            Fp_all=2*Es/(1-v^2)*deldata.*PunchRadius;
        %% Calculates maximal strain from Dimitriadis (Biophysical Journal, 2002),
        %% where a = contact radius (nm)
            a1=Fs./Es;
            a=(3/4*(1-v^2)/r*a1*1E6).^(1/3);
            strain=2/3.14*(1/(1-v^2))*a/r;
            maxstrain=max(strain);

%% Part V. Data plotting
%%%%%%%%%%%%%%%%%%%%%%%%%%%%%%%%%%%%%%%%%%%
%%%%%%%%%%%%%%%%%%%%%%%%%%%%%%%%%%%%%%%

    %% Plots Raw Data offset to zero and cropped between zero and maximum of
    %% non-linear data, with red approach curve, blue retraction curve:
        subplot(3,1,2);
        plot(-z,d,'b');
        xlabel('Scanner Position (-nm)');
        ylabel('Deflection (nm)');
        title('Raw Data Offset to Zero');
    %% Plots values of E vs. indentation depth for set and auto ROA data and model
        subplot(3,1,3);
        E_auto_matrix=zeros(size(deldata));
        E_auto_matrix(:,1)=Es*1E6;
        E0_matrix=zeros(size(del0));
        E0_matrix(:,1)=E0s*1E6;
        plot(deldata,E*1E6,'b*',deldata,E_auto_matrix,'m+',del0,E0_matrix,'ko');
        legend('discrete','ROA_a_u_t_o','ROA_s_e_t',-1);
        legend('boxoff');
        xlabel('Indentation (nm)');
        ylabel('E (kPa)');
    %% Saves the figure
        if (save==1);
            Fig_name1 = 'Fig1_';
            extension = '.tiff';
            Fig_name1 = [Fig_name1, test, extension];
            saveas(gcf,Fig_name1);
        else end;
```

```
   %% Plots log-log values of force-indentation for set ROA data and model
      figure;
      subplot(2,2,1);
      loglog(deldata,Fs_all,'g',del0_sphere,F0_sphere,'g*');
      xlabel('Log of Indentation (nm)');
      ylabel('Log of Force (nN)');
   %% Plots force-indentation profiles for set ROA data and model
      subplot(2,2,2);
      plot(deldata,Fs_all,'g',del0_sphere,F0_sphere,'g*');
      legend('sphere','ROA_s_e_t sphere',2);
      legend('boxoff');
      xlabel('Indentation (nm)');
      ylabel('Force (nN)');
   %% Plots log-log values of force-indentation for auto ROA data and model
      subplot(2,2,3);

loglog(deldata,Fp_all,'m',del_punch,F_punch,'mo',deldata,Fs_all,'g',del_sphere,F_sphere,'
g*');
      xlabel('Log of Indentation (nm)');
      ylabel('Log of Force (nN)');
   %% Plots force-indentation profiles for auto ROA data and model
      subplot(2,2,4);

plot(deldata,Fp_all,'m',del_punch,F_punch,'mo',deldata,Fs_all,'g',del_sphere,F_sphere,'g*
');
      legend('punch','ROA_a_u_t_o punch','sphere','ROA_a_u_t_o sphere',2);
      legend('boxoff');
      xlabel('Indentation (nm)');
      ylabel('Applied Force (nN)');
  %% Saves the figure
      if (save==1);
         Fig_name2 = 'Fig2_';
         extension = '.tiff';
         Fig_name2 = [Fig_name2, test, extension];
         saveas(gcf,Fig_name2);
      else end;

%% Solves for Indentation Modulus, K_ind (kPa)
   K_ind=4*Es/3/(1-v^2);
%% Calculates the percentage the sample thickness is indented at maximum
%% data point
   maxind=max(deldata);
   maxperind_t=maxind/sample_thickness*100;
```

```
%% Calculation of necessity of thin film correction - percentage of
%% thickness strained
   thin_film=((1+maxstrain)*maxind)/sample_thickness*100; %should be less than 100%
%% Saves data of interest into excel spreadsheet as one matrix
   export(dataindex,1)=dataindex;
   export(dataindex,2)=probe;
   export(dataindex,3)=v;
   export(dataindex,4)=k;
   export(dataindex,5)=r/1000;
   export(dataindex,6)=frequency;
   export(dataindex,7)=sample_thickness/1000;
   export(dataindex,8)=ROAstart;
   export(dataindex,9)=ROAend;
   export(dataindex,10)=ROAstart_auto;
   export(dataindex,11)=ROAend_auto;
   export(dataindex,12)=E0s*1E6;
   export(dataindex,13)=Es*1E6;
   export(dataindex,14)=R2_FF0s;
   export(dataindex,15)=R2_FFs;
   export(dataindex,16)=K_ind;
   export(dataindex,17)=maxstrain;
   export(dataindex,18)=thin_film;
   export(dataindex,19)=(maxperind_t)';
   export(dataindex,20)=PunchRadius;
   export(dataindex,21)=min(del_sphere);
   export(dataindex,22)=max(del_sphere);
   export(dataindex,23)=min(del_punch);
   export(dataindex,24)=max(del_punch);

%% End of analysis on data set
   end;
%%%%%%%%%%%%%%%%%%%%%%%%%%%%%%%%%%%%%%%%%%%%%%%%%%%%%%%%%%%%%%%%%%%%%%%
%%%%%%%%%%%%%%%%%%%%%%%%%%%%%%%%%%%%%%%%%%%%%%%%%%%%%%%%%%%%%%%%%%%%%%%

%% Analysis for Conical Tips
%%%%%%%%%%%%%%%%%%%%%%%%%%%%%%%%%%%%%%%%%%%%%%%%%%%%%%%%%%%%%%%%%%%%%%%
%%%%%%%%%%%%%%%%%%%%%%%%%%%%%%%%%%%%%%%%%%%%%%%%%%%%%%%%%%%%%%%%%%%%%%%

%% Part IIIa. Fits all user defined ROA data to Hertz Cone Model
%%%%%%%%%%%%%%%%%%%%%%%%%%%%%%%%%%%%%%%%%%%%%%%%%%%%%%%%%%%%%%%%%%%%%%%
%%%%%%%%%%%%%%%%%%%%%%%%%%%%%%%%%%%%%%%%%%%%%%%%%%%%%%%%%%%%%%%%%%%%%%%
   elseif (shape==2);
   %% removes upper range of F-del data to eliminate potential errors in model
```

```
   %% fitting, as the cone model should fit relatively close to values slightly
   %% greater than R
      del=del(del<175);
      indexstop=size(del);
      F=F(1:indexstop);
      s=3/4*(1-v^2)/(r^0.5);
      c=2*tan(angle*3.14/180)/3.14/(1-v^2);
      del_cone=del0;
      del0_cone=del_cone;
      F_cone=F0;
      F0_cone=F0;
      del0sq=del0_cone.^2;
      ratio=F0./del0sq;
      E0=ratio/c;%in GPa
      [ff,ee]=size(del0_cone);
      logdel_cone=log10(del0_cone);
      logF_cone=log10(F0_cone);
      start_point=mean(E0);
      [estimates,modelcone] = FitHertzCone_MSI(logF_cone,start_point);
      E0c=estimates;
      F0c=del0sq.*E0c*c;
      logF0c=log10(F0c);
%% Calculates correlation between F0_cone (data) and F0c (model)
      R = corrcoef(F0_cone,F0c);
      R2_FF0c=R(1,2);

%% Part IIIb1. Determines ROA automatically based on differential of error between
%% logarithmic data and model values for conical tips
%%%%%%%%%%%%%%%%%%%%%%%%%%%%%%%%%%%%%%%%%%%%%%%%%%%%%%%%%%%%%%%%%%%%%%%%%%%%
%%%%%%%%%%%%%%%%%%%%%%%%%%%%%%%%%%%%%%%%%%%%%%%%%%%%%%%%%%%%%%%%%%%%%%%%%%%%

%% Determines difference between data and model for ALL data
      Fc_all=del.^2*E0c*c;
      logFc_all=log10(Fc_all);
      logF=log10(F);
      logFc_diff_all=logFc_all-logF;
%% Finds all data points where the model and data compare (indexaa) within the
%% set condition by using binary numbers (1 if it fits, 0 if it does not)
      [aa,bb]=size(logFc_diff_all);
      eval=zeros(size(logFc_diff_all));
      m=1;
      condition=0.05;
      for m=1:aa;
```

```
    if abs(logFc_diff_all(m)) < condition;
    eval(m)=1;
    else eval(m)=0;
    end;
  m=m+1;
  end;
%% Yields indices of minimum and maximum (range) values for which the model fits
%% within the condition
  indexaa=find(eval==max(eval));
  [cc,dd]=size(indexaa);
  start5=indexaa(1);
  stop5=indexaa(cc);
%% Fits the somewhat trimmed data to the conical model again for
%% better accuracy
  del_cone=del(start5:stop5);
  del_conesq=del_cone.^2;
  F_cone=F(start5:stop5);
  logdel_cone=log10(del_cone);
  logF_cone=log10(F_cone);
  start_point=E0c;
  [estimates,modelcone] = FitHertzCone_MSI(logF_cone,start_point);
  Ec=estimates;
  Fc=del_conesq.*Ec*c;
  logF0c=log10(Fc);
%% Determines difference between data and model for this trimmed data
  Fc_all=del.^2*Ec*c;
  logFc_all=log10(Fc_all);
  logF=log10(F);
  logFc_diff_all=logFc_all-logF;
%% Calculates correlation between F_cone (conical data) and Fc (conical model)
  R = corrcoef(F_cone,Fc);
  R2_FFc=R(1,2);
%% Finds data points where the model and data compare (indexaa) within the
%% set condition by using binary numbers (1 if it fits, 0 if it does not)
  [aa,bb]=size(logFc_diff_all);
  eval=zeros(size(logFc_diff_all));
  m=1;
  condition=0.05;
  for m=1:aa;
    if abs(logFc_diff_all(m)) < condition;
    eval(m)=1;
    else eval(m)=0;
    end;
```

```
      m=m+1;
      end;
%% Yields indexes of values for which the model fits within the condition
      indexaa=find(eval==max(eval));
      [cc,dd]=size(indexaa);
%% Kicks out linear data (i.e. those data sets with less than 10 points
%% that fit the model within the criterion)
   if (cc < 10);
      display('Poor Fit to Model, Data Not Analyzed');
      subplot(3,1,3);
      title('Poor Fit to Model, Data Not Analyzed');
   else;
%% Determines the range of analysis (stop5:start5) for the fit to the conical
%% model.  Five (5) points are analyzed at a time starting from the highest point.
%% At least 3 of the 5 have to fit.  The algorithm sets the start point for analysis
%% to be the lowest point of the fit or the lowest point of the range if all fit.
      maxa=max(indexaa);
      mina=min(indexaa);
      inc=5;
      n=cc;
      eval2=indexaa(n)-indexaa(n-inc+1);
      diff12=eval2-inc;
      stop5=indexaa(cc);
      start5=indexaa(n-inc+1);
      for n=cc:-1:5;
         if start5 > mina+2;
            if (diff12 < 3);
               eval2=indexaa(n)-indexaa(n-inc+1);
               diff12=eval2-inc;
               start5=start5-1;
            else end;
         else end;
      end;
      if start5-indexaa(1)<4;
         start5=indexaa(1);
      else end;
%% Kicks out linear data (i.e. those data sets with less than 10 points
%% that fit the model within the criterion)
   if (stop5-start5+1 < 10);
      display('Poor Fit to Model, Data Not Analyzed');
      subplot(3,1,3);
      title('Poor Fit to Model, Data Not Analyzed');
   else;
```

```
%% Designates the upper and lower values as those of the automatically
%% determined ROA for the conical fit
    startcone=start5;
    stopcone=stop5;
    del_cone=del(startcone:stopcone);
    F_cone=F(startcone:stopcone);
%% Finds ROA for automatically determined range
    ROAstart_auto=del(startcone);
    ROAend_auto=del(stopcone);
%% Finds the highest index between the set and auto ROAs to set the upper
%% point for plotting
    maxvalue=max([stop2,stopcone]);
%% Resizes F and del data to plot up to the maximum value between the two
%% sets of data
    deldata=del(1:maxvalue);
    Fdata=F(1:maxvalue);
    Fc_all=deldata.^2*Ec*c;

%% Part IIIb2. Fits Remainder of Data to Other Models: Spherical and Punch
%%%%%%%%%%%%%%%%%%%%%%%%%%%%%%%%%%%%%%%%%%%%%%%%%%%%%%%%%%%%%%%%%%%%%%%
%%%%%%%%%%%%%%%%%%%%%%%%%%%%%%%%%%%%%%%%%%%%%%%%%%%%%%%%%%%%%%%%%%%%%%%

%% Assigns lower index values to fit the spherical model
    startsphere=1;
    stopsphere=startcone-1;
%% Redefines data set according to automatically determined ROA
    del_sphere=del(startsphere:stopsphere);
    F_sphere=F(startsphere:stopsphere);
    del_cone=del(startcone:stopcone);
    F_cone=F(startcone:stopcone);
%% Obtains original estimate of fit to Hertz Sphere Model using set ROA
%% data
    logF_sphere=log10(F_sphere);
    del32=del_sphere.^1.5;
    ratio=F_sphere./del32;
    E0s=ratio.*s;
    start_point=E0s(1);
    [estimates,modelsphere] = FitHertzSphere_MSI(logF_sphere,start_point);
    E0s=estimates;
    Fs=E0s*del_sphere.^1.5/s;
    Fs_all=E0s*del(1:maxvalue).^1.5/s;
    logFs=log10(Fs);
%% Determines difference between data and model for lower values of data
```

```
    logFs_diff=logFs-logF_sphere;
    Fs_diff=Fs-F_sphere;
%% Finds all data points where the spherical model and data compare (indexaa)
%% within the set condition by using binary numbers (1 if it fits, 0 if it
%% does not) for later assignment of values to punch model
      [aa,bb]=size(logFs_diff);
      eval=zeros(size(logFs_diff));
      m=1;
      condition=0.05; % appears to be optimal value
      for m=1:aa;
        if abs(logFs_diff(m)) < condition;
          eval(m)=1;
        else eval(m)=0;
        end;
        m=m+1;
      end;
%% Yields indexes of values for which the model fits within the condition
      indexaa=find(eval==max(eval));
      [cc,dd]=size(indexaa);
%% Assigns data to spherical models
      stopsphere=max(startcone-1);
      startsphere=min(indexaa);
      del_sphere=del(startsphere:stopsphere);
      F_sphere=F(startsphere:stopsphere);
    %% if all lower data fit the spherical model, then assigns punch data
    %% to first data point of punch only to line up curve
      if startsphere>1;
        del_punch=del(1:startsphere-1);
        F_punch=F(1:startsphere-1);
      else;
        del_punch=del(1);
        F_punch=F(1);
      end;
    %% Fits cropped spherical portion of data to Hertz Sphere Model
      logF_sphere=log10(F_sphere);
      del32=del_sphere.^1.5;
      ratio=F_sphere./del32;
      Es=ratio.*s;
      start_point=Es(1);
      [estimates,modelsphere] = FitHertzSphere_MSI(logF_sphere,start_point);
      Es=estimates;
      Fs=Es*del_sphere.^1.5/s;
      Fs_all=Es*del(1:maxvalue).^1.5/s;
```

```
    logFs=log10(Fs);
  %% Calculates correlation between Fs (spherical data) and Fs (spherical model)
    [gg,hh]=size(Fs);
    if gg==1;
      R2_FFs=0; % to avoid errors in spreadsheet exporting
    else;
      R = corrcoef(F_sphere,Fs);
      R2_FFs=R(1,2);
    end;
  %% Determines difference between data and model for lower values of data
    logFs_diff=logFs-logF_sphere;
    Fs_diff=logFs-F_sphere;
  %% Fits portion of punch data to punch model to solve for punch radius
    PunchRadius=r/20;
    logF_punch=log10(F_punch);
    start_point=PunchRadius;
    [estimates,modelpunch] = FitPunch_MSI(logF_punch,start_point);
    PunchRadius=estimates;
    Fp=2*Es/(1-v^2)*del_punch.*PunchRadius;
  %% Calculates F_punch over larger data set of del to see more clearly on plot
    Fp_all=2*Es/(1-v^2)*del(1:maxvalue).*PunchRadius;
  %% Calculates maximal strain from Dimitriadis (Biophysical Journal, 2002),
  %% where a = contact radius (nm)
    a1=Fs./Es;
    a=(3/4*(1-v^2)*r*a1).^(1/3);
    strain=2/3.14*(1/(1-v))*a/r;
    maxstrain=max(strain);

%% Part IV. Data plotting
%%%%%%%%%%%%%%%%%%%%%%%%%%%%%%%%%%%%%%%%%%%%%%%%%%%%%%%%%%%%%%%%%%%%%%%%%%%%%%%%

  %% Plots Raw Data offset to zero and cropped between zero and maximum of
  %% non-linear data, with red approach curve, blue retraction curve:
    subplot(3,1,2);
    plot(-z,d,'b');
    xlabel('Scanner Position (-nm)');
    ylabel('Deflection (nm)');
    title('Raw Data Offset to Zero');
  %% Plots values of E vs. indentation depth for set and auto ROA data and model
    subplot(3,1,3);
    E_auto_matrixc=zeros(size(del_cone));
    E_auto_matrixc(:,1)=Ec*1E6;
```

```
        E0_matrixc=zeros(size(del0));
        E0_matrixc(:,1)=E0c*1E6;
        E_auto_matrixs=zeros(size(del_sphere));
        E_auto_matrixs(:,1)=Es*1E6;
        del32=deldata.^1.5;
        Es_dis=s*Fdata./del32*1E6;
        delsqc=deldata.^2;
        ratioc=Fdata./delsqc;
        Ec_dis=ratioc./c*1E6;

plot(deldata,Ec_dis,'b*',del_cone,E_auto_matrixc,'k+',del0,E0_matrixc,'k',deldata,Es_dis,
'bo',del_sphere,E_auto_matrixs,'g+');
        legend('cone model','cone ROA_a_u_t_o','cone ROA_s_e_t','sphere model','sphere
ROA_a_u_t_o',-1);
        legend('boxoff');
        xlabel('Indentation (nm)');
        ylabel('E (kPa)');
    %% Saves the figure
        if (save==1);
            Fig_name1 = 'Fig1_';
            extension = '.tiff';
            Fig_name1 = [Fig_name1, test, extension];
            saveas(gcf,Fig_name1);
        else end;
    %% Plots log-log values of force-indentation for set ROA data and model
        figure;
        subplot(2,2,1);
        loglog(deldata,Fc_all,'k',del0_cone,F0_cone,'k*');
        xlabel('Log of Indentation (nm)');
        ylabel('Log of Force (nN)');
    %% Plots force-indentation profiles for set ROA data and model
        subplot(2,2,2);
        plot(deldata,Fc_all,'k',del0_cone,F0_cone,'k*');
        legend('cone model','cone ROA_s_e_t',2);
        legend('boxoff');
        xlabel('Indentation (nm)');
        ylabel('Force (nN)');
    %% Plots log-log values of force-indentation for auto ROA data and model
        subplot(2,2,3);

loglog(deldata,Fp_all,'m',del_punch,F_punch,'m+',deldata,Fs_all,'g',del_sphere,F_sphere,'
go',deldata,Fc_all,'k',del_cone,F_cone,'k*');
        xlabel('Log of Indentation (nm)');
```

```
        ylabel('Log of Force (nN)');
    %% Plots force-indentation profiles for auto ROA data and model
        subplot(2,2,4);

plot(deldata,Fp_all,'m',del_punch,F_punch,'m+',deldata,Fs_all,'g',del_sphere,F_sphere,'go
',deldata,Fc_all,'k',del_cone,F_cone,'k*');
        legend('punch model','punch data','sphere model','sphere data','cone model','cone
data',2);
        legend('boxoff');
        xlabel('Indentation (nm)');
        ylabel('Applied Force (nN)');
  %% Saves the figure
        if (save==1);
            Fig_name2 = 'Fig2_';
            extension = '.tiff';
            Fig_name2 = [Fig_name2, test, extension];
            saveas(gcf,Fig_name2);
        else end;

%% Part V. Other analysis and entry of data into spreadsheet
%%%%%%%%%%%%%%%%%%%%%%%%%%%%%%%%%%%%%%%%%%%%%%%%%%%%%%%%%%%%%%%%%%%%%%%%%%%%%%%%%%%%%%%%%%%%%
%%%%%%%%%%%%%%%%%%%%%%%%%%%%%%%%%%%%%%%%%%%%%%%%%%%%%%%%%%%%%%%%%%%%%%%%%%%%%%%%%%%%%

%% Solves for Indentation Modulus, K_ind (kPa)
    K_ind=4*Es*1E6/3/(1-v^2);
%% Calculates the percentage the sample thickness is indented at maximum
%% data point
    maxind=max(deldata);
    maxperind_t=maxind/sample_thickness*100;
%% Calculation of necessity of thin film correction - percentage of
%% thickness strained
    thin_film=((1+maxstrain)*maxind)/sample_thickness*100; %should be less than 100%
%% Saves data of interest into excel spreadsheet as one matrix
    export(dataindex,1)=dataindex;
    export(dataindex,2)=probe;
    export(dataindex,3)=v;
    export(dataindex,4)=k;
    export(dataindex,5)=r/1000;
    export(dataindex,6)=frequency;
    export(dataindex,7)=sample_thickness/1000;
    export(dataindex,8)=ROAstart;
    export(dataindex,9)=ROAend;
    export(dataindex,10)=ROAstart_auto;
```

```
   export(dataindex,11)=ROAend_auto;
   export(dataindex,12)=PunchRadius;
   export(dataindex,13)=Es*1E6;
   export(dataindex,14)=deloff;
   export(dataindex,15)=Foff;
   export(dataindex,16)=K_ind;
   export(dataindex,17)=maxstrain;
   export(dataindex,18)=thin_film;
   export(dataindex,19)=(maxperind_t)';
   export(dataindex,20)=angle;
   export(dataindex,21)=E0c*1E6;
   export(dataindex,22)=Ec*1E6;
   export(dataindex,23)=R2_FF0c;
   export(dataindex,24)=R2_FFc;
   export(dataindex,25)=min(del_cone);
   export(dataindex,26)=max(del_cone);
   export(dataindex,27)=min(del_sphere);
   export(dataindex,28)=max(del_sphere);
   export(dataindex,29)=min(del_punch);
   export(dataindex,30)=max(del_punch);

%% End of analysis on data set
%%%%%%%%%%%%%%%%%%%%%%%%%%%%%%%%%%%%%%%%%%%%%%%%%%%%%%%%%%%%%%%%%%%%%%%
%%%%%%%%%%%%%%%%%%%%%%%%%%%%%%%%%%%%%%%%%%%%%%%%%%%%%%%%%%%%%%%%%%%%%%%
      end;
   end;
   end;
end;
end;
%% Increments algorithm to run again for next data set
   dataindex=dataindex+1;
end;

%% Part VI.  Deletion of data based upon set criterion
%%%%%%%%%%%%%%%%%%%%%%%%%%%%%%%%%%%%%%%%%%%%%%%%%%%%%%%%%%%%%%%%%%%%%%%
%%%%%%%%%%%%%%%%%%%%%%%%%%%%%%%%%%%%%%%%%%%%%%%%%%%%%%%%%%%%%%%%%%%%%%%
%%  Saves all data to spreadsheet
   if (save==1);
      name = 'allsummary';
      extension = '.xls';
      name = [sampletype, name, extension];
      wk1write(name,export);
   else end;
```

```
%% Deletes data from summary due to the following conditions:
%% May want to add this back per individual requirements
      alldata=export;
      [a_all,b_all]=size(alldata);
      for dataindex3=1:a_all;
%% deletes data where strain exceeds depth of sample and thin film
%% correction would be necessary:
      if (alldata(dataindex3,18) > 100.0);
         alldata(dataindex3,:)=0;
      else end;
% %% Strain condition for materials that are not necessary linear elastic
% %% over large strain conditions, set strain condition to not exceed 10%
% %% (strain_cond=0.1), this is optional and will be exceeded with conical
% %% tips easily
%             strain_cond=0.1;
%             if (alldata(dataindex3,17) > strain_cond);
%                alldata(dataindex3,:)=0;
%             else end;
% %% Condition that kicks out data where R2>0.99
%           if (shape==1);
%              if (alldata(dataindex3,14) < 0.99);
%                 alldata(dataindex3,:)=0;
%              elseif (alldata(dataindex3,15) < 0.99);
%                 alldata(dataindex3,:)=0;
%              else end;
%           elseif (shape==2);
%              if (alldata(dataindex3,23) < 0.99);
%                 alldata(dataindex3,:)=0;
%              elseif (alldata(dataindex3,24) < 0.99);
%                 alldata(dataindex3,:)=0;
%              else end;
%           end;
      dataindex3=dataindex3+1;
      end;
      % Removes zero data from further compilation
      alldata = sortrows(alldata);
      index=find(alldata(:,1) == 0);
      alldata(index,:)=[];

%% Part VII.  Plots compilation of good data only
%%%%%%%%%%%%%%%%%%%%%%%%%%%%%%%%%%%%%%%%%%%%%%%%%%%%%%%%%%%%%%%%%%%%%%%
%%%%%%%%%%%%%%%%%%%%%%%%%%%%%%%%%%%%%%%%%%%%%%%%%%%%%%%%%%%%%%%%%%%%%%%
```

```
%% Plots stiffness vs. contact radius
   figure;
   if (shape==1);
      plot(alldata(:,14),alldata(:,12),'b+',alldata(:,15),alldata(:,13),'bo');
      legend('ROA_s_e_t','ROA_a_u_t_o',0);
      legend('boxoff');
      title('Modulus vs. Fit to Spherical Model');
      xlabel('Correlation Coefficient');
      ylabel('E (kPa)');
   elseif (shape==2);
      plot(alldata(:,23),alldata(:,21),'g+',alldata(:,24),alldata(:,22),'go');
      legend('ROA_s_e_t','ROA_a_u_t_o',0);
      legend('boxoff');
      title('Modulus vs. Fit to Conical Model');
      xlabel('Correlation Coefficient');
      ylabel('E (kPa)');
   end;
%%  Saves data compilation figure
   if (save==1);
      Fig_name3 = 'goodsummary';
      extension = '.tiff';
      Fig_name3 = [cantilever,sampletype,Fig_name3, extension];
      saveas(gcf,Fig_name3);
   else end;
%% Calculates averages and standard deviations for stiffness values
   [size1,size2]=size(alldata);
   n2=size1
   if shape==1
      Es_avg=sum(alldata(:,12))/n2
      Es_std=STD(alldata(:,12))
      Es_auto_avg=sum(alldata(:,13))/n2
      Es_auto_std=STD(alldata(:,13))
      alldata(size1+1,12)=Es_avg;
      alldata(size1+2,12)=Es_std;
      alldata(size1+3,12)=n2;
      alldata(size1+2,13)=Es_auto_std;
      alldata(size1+1,13)=Es_auto_avg;
      alldata(size1+3,13)=n2;
   elseif shape==2;
      Es_auto_avg=sum(alldata(:,13))/n2
      Es_auto_std=STD(alldata(:,13))
      Ec_avg=sum(alldata(:,21))/n2
      Ec_std=STD(alldata(:,21))
```

```
    Ec_auto_avg=sum(alldata(:,22))/n2
    Ec_auto_std=STD(alldata(:,22))
    alldata(size1+1,13)=Es_auto_avg;
    alldata(size1+2,13)=Es_auto_std;
    alldata(size1+3,13)=n2;
    alldata(size1+1,21)=Ec_avg;
    alldata(size1+2,21)=Ec_std;
    alldata(size1+3,21)=n2;
    alldata(size1+1,22)=Ec_auto_avg;
    alldata(size1+2,22)=Ec_auto_std;
    alldata(size1+3,22)=n2;
  else end;
%%  Saves good data to spreadsheet
  if (save==1);
    name2 = 'goodsummary';
    extension = '.xls';
    name = [cantilever, sampletype, name2, extension];
    wk1write(name,alldata);
  else end;

%% Indicates the end of the algorithm
%%%%%%%%%%%%%%%%%%%%%%%%%%%%%%%%%%%%%%%%%%%%
%%%%%%%%%%%%%%%%%%%%%%%%%%%%%%%%%%%%
  disp('Game Over');

return;
%%%%%%%%%%%%%%%%%%%%%%%%%%%%%%%%%%%%%%%%%%%%
%%%%%%%%%%%%%%%%%%%%%%%%%%%%%%%%%%%%
```

Appendix 2. Matlab code for solving E from force-indentation profiles obtained with AFM, Hertz Cone Model Fitting

```
%% FitHertzCone_MSI algorithm to be used in conjuction with
%% ModulusSolver_MicrosphereIndentation algorithm to solve for
%% Young's modulus, E, of sample by minimation of sum of square
%% error between the logarithmic F-del data of the sample (data)
%% and the theoretical Hertz sphere model.
%% M. T. Frey, 10/30/06

function [estimates,modelcone] = FitHertzCone_MSI(logF_cone,start_point);
   modelcone = @logfit;
   estimates = fminsearch(modelcone,start_point);
   function [sse, FittedCurve] = logfit(params);
      global c del_cone logF_cone;
      Ecfit = params(1);
      Fcfit = Ecfit*c*del_cone.^2;
      logFcfit = log10(Fcfit);
      Error = logF_cone - logFcfit;
      sse = sum(Error.^ 2);
```

Appendix 3. Matlab code for solving E from force-indentation profiles obtained with AFM, Hertz Sphere Model Fitting

```
%% FitHertzSphere_MSI algorithm to be used in conjuction with
%% ModulusSolver_MicrosphereIndentation algorithm to solve for
%% Young's modulus, E, of sample by minimation of sum of square
%% error between the logarithmic F-del data of the sample (data)
%% and the theoretical Hertz sphere model.
%% M. T. Frey, 10/30/06

function [estimates,modelsphere] = FitHertzSphere_MSI(logF_sphere,start_point);
   modelsphere = @logfit;
   estimates = fminsearch(modelsphere, start_point);
   function [sse, FittedCurve] = logfit(params);
      global s del_sphere logF_sphere;
      Esfit = params(1);
      Fsfit = Esfit*del_sphere.^1.5/s;
      logFsfit = log10(Fsfit);
      Error = logFsfit - logF_sphere;
      sse = sum(Error.^ 2);
```

Appendix 4. Matlab code for solving E from force-indentation profiles obtained with AFM, Punch Radius Fitting

```
%% FitPunch_MSI algorithm to be used in conjuction with
%% ModulusSolver_MicrosphereIndentation algorithm to solve for
%% punchfactor by minimation of sum of square
%% error between the logarithmic F-del data of the sample (data)
%% and the theoretical punch data.
%% M. T. Frey, 01/04/07

function [estimates,modelpunch] = FitPunch_MSI(logF_punch,start_point);
   modelpunch = @logfit;
   estimates = fminsearch(modelpunch,start_point);
   function [sse, FittedCurve] = logfit(params);
      global Es v del_punch logF_punch;
      PunchRadius = params(1);
      F_p=2*Es*del_punch.*PunchRadius/(1-v^2);
      logF_p = log10(F_p);
      Error = logF_p - logF_punch;
      sse = sum(Error.^ 2);
```

Appendix 5. Matllab code for solving E from force-indentation profiles obtained with Microsphere Indentation

```
%% Master file (06/12/07) for compilation of MSI data created by M.T. Frey

clc; clear all; close all;
global c p del logFd;

%  Settings on data collection
   % Micrometer calibration
      increment_dial_mic=10;
      increment_frame_mic=225;
   % Stiffness calibration from deflection, length is cut dimension of
   % wire (inches)
      increment_frame_d=900;
   % Conversion of microns to pixels for images taken at 40X (from scalebar image):
      micronsperpixel=100/314;
   % Settings on sample data collection: Poisson's ratio, v and frame increment
      v=0.45;
      increment_frame_data=225;

% Imports vertical calibration data of micromanipulator movement
      vert = load ('vertical.txt');

% Settings on compilation file names for figures and data exporting
      cantilever = '17_';
      sampletype = 'Wong2_gels';
      save=0; % enter 0 for no for quick peek at data, enter 1 to save all images and data

% Data sets to compile, note that settings for individual tests only need
% to be entered on the first set if the settings are the same on several
% data sets, else enter the new values.

   dataindex=1
   stop=6;
   for dataindex=1:stop;
     extension = '.txt';
     if (dataindex==1);
        calibration = load ('calibration17.txt');
        diameter = load ('diameter17.txt');
        length_in = 3/16;
```

```
        cant = 17; %for later identification in data
        test='17_060707_Wong_A2'
        sample_thickness = 50000;
    elseif (dataindex==2)
        test='17_060707_Wong_A3C'
    elseif (dataindex==3)
%           test='17_060707_Wong_A4'
%       elseif (dataindex==4)
        test='17_060807_Wong_B2'
    elseif(dataindex==4);
        test='17_060807_Wong_B3'
    elseif(dataindex==5);
        test='17_061107_Wong_C1B'
    elseif(dataindex==6);
        test='17_061107_Wong_C2'
    end;

% Loads file names and data for each data set to label saved files accordingly
    name=[test,extension];
    data=load(name);

% Conversion of dial movement on micromanipulator to vertical distance (nm):
    [a,b] = size(vert);
    nm_per_dialtick=((sum(vert)/a)*increment_frame_mic/increment_dial_mic);

% Conversion of calibration data to bending stiffness, k (nN/nm):
  % Calculates force (nN) from mass (mg)
    length_mm=25.4*length_in;
    m=calibration(:,1).*length_mm;
    f=m*9.81*1E3;
  % Calculates average vertical deflection, d (nm), of microsphere:
    frames1=calibration(:,2);
    frames2=calibration(:,3);
    frames3=calibration(:,4);
    frames=(frames1+frames2+frames3)/3;
    d=frames*increment_frame_d;
  % Calculates vertical bending stiffness (nN/nm):
    k_z=zeros(size(d));
    k_z=d\f;
  % Fits a line to data and finds the goodness of fit, R^2:
    Fz=k_z*d;
    R = corrcoef(f,Fz);
    R2_k=R(1,2);
```

```
   % Plots indenter deflection converted to microns only for graphing
      figure;
      subplot(2,2,1);
      plot(d/1000,f/1000,'gx:',d/1000,Fz/1000,'k-');
      xlabel('Cantilever Deflection (microns)');
      ylabel('Force (microN)');
      title('Cantilever Stiffness Calibration');
% Conversion of diameter measurement in pixels to radius in nm:
      [m,n]=size(diameter);
      r=(sum(diameter)/m)/2*micronsperpixel*1000;

% Indentation data from sample converted from raw data
   % Note that data matrices are increased in size by one due to the manner
   % in which data is taken (i.e. no line of data at maximum indentation depth)
      [p,q] = size(data);
      p=p+1;
   % Converts micromanipulator dial movement to vertical indenter movement (nm)
      zd=data(:,1);
      zd=zd*nm_per_dialtick;
      zd0=zeros(p,1);
      zd0(2:p)=zd;
   % Converts raw indenter deflection to nm deflection
      zc=data(:,3);
      zc=zc*increment_frame_data;
      zc0=zeros(p,1);
      zc0(1:p-1)=zc(p-1:-1:1);
      zc0(p)=0;
      zc0(1:p)=zc0(p:-1:1);
   % Converts indentation depth in number of frames to nm indentation
   % Uses last measurement of (B-A) values in case of differences
      del_0=data(p-1,2)*increment_frame_data;
   %  Calculates del at each point (B-A)
      del=zeros(p,1);
      del(1)=del_0;
      del(2:p)=del_0-zc;
      del(del<0)=0;
      del(1:p)=del(p:-1:1);
   % Converts lateral displacement, y, from pixels to nm
      y=data(:,4);
      ymax=max(y);
      y=ymax-y;
      y(1:p-1)=y(p-1:-1:1);
      lat=zeros(p,1);
```

```
        lat(1:p-1)=y;
        lat(p)=ymax;
        lat=lat*micronsperpixel*1000;
    % Calculates net displacement of microsphere tip
        tip_dis=(zc0.^2+lat.^2).^0.5;

% Calculation of applied force after determination of contact point and
% offsetting the vertical measurements to the contact point
    % Contact point estimation from extrapolation of tip displacement
        slope=(tip_dis(p)-tip_dis(p-1))/(zd0(p)-zd0(p-1));
        z_contact=zd0(p-1)-(tip_dis(p-1)/slope);
        zoff=zd0-z_contact;
        zoff(1)=0;
    % Plots the original and offset values for tip displacement (converted to
    % microns for plotting)
        extrapolation_z=size(tip_dis);
        extrapolation_r=size(tip_dis);
        extrapolation_z(1)=z_contact/1000;
        extrapolation_z(2:p)=zd0(2:p)/1000;
        extrapolation_r(1)=0;
        extrapolation_r(2:p)=tip_dis(2:p)/1000;
        subplot(2,2,2);
        plot(zd0(2:p)/1000,tip_dis(2:p)/1000,'ro-
',extrapolation_z,extrapolation_r,'r:+',zoff/1000,tip_dis/1000,'ko-');
        xlabel('Micromanipulator Movement (microns)');
        ylabel('Tip Displacement (microns)');
        legend('data','extrapolation','data_a_d_j');
    % Calculates force applied to sample, F, from vertical movement (adjusted)
        zdiff=zoff-zc0;
        zdiff(zdiff<0)=0;
        Fd=k_z*zdiff;
    % Test for linearity of tip displacement data by extrapolating a straight line
    % from the first two points of the tip displacement-Fd curve, comparing
    % the last value to the value of the straight line calculated at that point
        SL_slope=Fd(p-1)/tip_dis(p-1);
        SL_p=tip_dis(p-1)*(((Fd(p)-Fd(p-1))/Fd(p-1))+1);
        SL=size(tip_dis(p));
        SL(1:p-1)=tip_dis(1:p-1);
        SL(p)=SL_p;
        SL_diff=SL_p/tip_dis(p);
    % Plots force vs. indenter displacement
        subplot(2,2,3);
```

```
      plot(del/1000,Fd/1000,'bx-',lat/1000,Fd/1000,'g*-',tip_dis/1000,Fd/1000,'k+-',
SL/1000,Fd/1000,'ro-');
      legend('z','y','total','linear');
      xlabel('Tip Displacement (microns)');
      ylabel('Applied Force (microN)');
% Calculates material stiffness, E (kPa), from Hertz Sphere Model
      c=3/4*(1-v^2)/(r^0.5);
      del32=del(2:p).^1.5;
   % Calculation of E (kPa) at discrete points
      E=c*Fd(2:p)./del32*1E6
      E_avg=(E(2)+E(1))/2
      E_diff=(E-E_avg)/E_avg;
      E_diff=max(E_diff)
      Fs=E_avg/1E6/c*del.^1.5;
   % Plots force-indentation profiles for data and model
      subplot(2,2,4);
      plot(del/1000,Fd/1000,'bx-',del/1000,Fs/1000,'ko:');
      legend('data', 'model');
      xlabel('Indentation (microns)');
      ylabel('Applied Force (microN)');
   % Saves the figure
      Fig_name1 = 'Fig1_';
      extension = '.tiff';
      Fig_name1 = [Fig_name1, test, extension];
      if (save==1);
         saveas(gcf,Fig_name1);
      else end;

% Calculates contact area and amount of indentation relative to radius and thickness
      perind_t=del(2:p)/sample_thickness*100;
      a=(del(2:p).*r).^(0.5);
      contact_ratio=a/r;
      perind_r=contact_ratio.^2
      rind_diff=perind_r(2)-perind_r(1);
%  Correction for large indentation per Yoffe (Philo. Mag. A, 1984, 813-828)
   % Table of values for v=0.4 material
      d=[0.04 0.068   0.092   0.18    0.24    0.4]';
      aoverR=[0.141  0.225   0.279   0.43    0.53    0.73]';
      D=[1    1   0.99    0.96    0.94    0.86]';
      [w,x]=size(d);
   % Extrapolates values at higher indentation, else interpolates from table values
         for i=1:(p-1);
            if (contact_ratio(i) > aoverR(w));
```

```
            pos(i)=(contact_ratio(i)-aoverR(w-2))/(aoverR(w)-aoverR(w-2));
            d(i)=d(w-2)+((d(w)-d(w-2))*pos(i));
            D(i)=D(w-2)+((D(w)-D(w-2))*pos(i));
            E_corr(i)=(1-0.1317*d(i))^1.5/D(i)^0.5*E(i);
            else;
            d_int(i)=interp1(aoverR,d,contact_ratio(i));
            D_int(i)=interp1(aoverR,D,contact_ratio(i));
            E_corr(i)=(1-0.1317*d_int(i))^1.5/D_int(i)^0.5*E(i);
            end;
         end;
         E_Yoffe=E_corr';
         E_corr_diff=(E_Yoffe-E)./E*100;

   % Calculates maximal strain from Dimitriadis (Biophysical Journal, 2002),
   % where a = contact radius (nm)
      a1=Fs(2:p)./E_avg;
      a=(3/4*(1-v^2)*r*a1*1E6).^(1/3);
      strain=2/3.14*(1/(1-v))*a/r

   % Calculation of necessity of thin film correction - percentage of
   % thickness strained
      thin_film=((1+strain(p-1))*del(p))/sample_thickness*100; %should be less than
100%

   % Plots stiffness vs. force for data, model, and Yoeffe correction
      figure;
      subplot(3,1,1);
      plot(Fd(2:p)/1000,E,'b+-',Fd(2:p)/1000,E_Yoffe,'gx-',Fd(2:p)/1000,E_avg,'ko:');%
      legend('data','corrected','model');
      xlabel('Applied Force (microN)');
      ylabel('E (kPa)');
   % Plots stiffness vs. indentation ratio (% of R)
      subplot (3,1,2);
      plot(perind_r,E,'b+-',perind_r,E_Yoffe,'gx-',perind_r,E_avg,'ko:');%
      legend('data','corrected','model');
      xlabel('Indentation/Radius');
      ylabel('E (kPa)');
   % Plots stiffness vs. indentation of thickness (% of t)
      subplot (3,1,3);
      plot(perind_t,E,'b+-',perind_t,E_Yoffe,'gx-',perind_t,E_avg,'ko:');%
      legend('data','corrected','model');
      xlabel('Indentation/Thickness');
      ylabel('E (kPa)');
```

```
    % Saves the figure
       Fig_name2 = 'Fig2_';
       extension = '.tiff';
       Fig_name2 = [Fig_name2, test, extension];
       if (save==1);
          saveas(gcf,Fig_name2);
       else end;

% Saves data of interest into excel spreadsheet as one matrix
       export(dataindex,1)=dataindex;
       export(dataindex,2)=cant;
       export(dataindex,3)=v;
       export(dataindex,4)=k_z;
       export(dataindex,5)=r/1000;
       export(dataindex,6:7)=(del(2:p)/1000)';
       export(dataindex,8:9)=(Fd(2:p)/1000)';
       export(dataindex,10:11)=(E)';
       export(dataindex,12)=E_diff;
       export(dataindex,13:14)=(Fs(2:p)/1000)';
       export(dataindex,15)=E_avg;
       export(dataindex,16:17)=(perind_r)';
       export(dataindex,18)=rind_diff;
       export(dataindex,19)=(export(dataindex,16)+export(dataindex,17))/2;
       export(dataindex,20)=sample_thickness/1000;
       export(dataindex,21:22)=(perind_t)';
       export(dataindex,23)=SL_diff;
       export(dataindex,24:25)=(E_Yoffe)';
       export(dataindex,26:27)=(E_corr_diff)';
       export(dataindex,28:29)=(strain)';
       export(dataindex,30)=thin_film;
% Deletes data if condition of tip displacement linearity is not met
         if (SL_diff < 0.90);
           export(dataindex,:)=0;
           display('Nonlinear data');
         elseif (SL_diff > 1.00);
           SL_diff_new = SL_diff - 1.0;
           if (SL_diff_new > 0.10);
              export(dataindex,:)=0;
              display('Nonlinear data');
           else end;
         else end;
% Deletes data from summary if contact area exceeds R (perarea > 1.0)
         if (export(dataindex,17) > 1.0);
```

```
            export(dataindex,:)=0;
            display('indentation too large');
          else end;

% Increments to run algorithm on next set of data
       dataindex=dataindex+1
  end;

% Sorts the data matrix in ascending order to graph non-zero data
       alldata = export;
       alldata = sortrows(alldata);
       index=find(alldata(:,1) == 0);
       alldata(index,:)=[];
% Saves all data to spreadsheet
       extension = '.xls';
       filename1='alldata';
       name = [cantilever, sampletype, filename1, extension];
       if (save==1);
          wk1write(name,export);
       else end;

% Graphing of all data:
   % Plots Stiffness vs. indentation depth
       figure;
       subplot(2,2,1);
       plot(alldata(:,16),alldata(:,10),'bo',alldata(:,17),alldata(:,11),'bo');
       xlabel('Indentation/Radius');
       ylabel('E_d_a_t_a (kPa)');
       hold on;
   % Plots Model Calculated Stiffness vs. Average Indentation of Radius
       subplot(2,2,2);
       plot(alldata(:,19),alldata(:,15),'bo');
       xlabel('Average Indentation/Radius');
       ylabel('E_m_o_d_e_l (kPa)');
       hold on;
   % Plots Maximum Indentation as a % or R vs. Difference between
   % model calculated value of E
       subplot(2,2,3);
       plot(alldata(:,12),alldata(:,17),'mo');
       xlabel('Difference of E values');
       ylabel('Maximum Indentation (% or R)');
       hold on;
   % Plots difference between indentations vs. Difference between
```

```
   % calculated values of E
      subplot(2,2,4);
      plot(alldata(:,12),(alldata(:,17)-alldata(:,16)),'mo');
      xlabel('Difference of E values');
      ylabel('Differential Indentation (% of R)');
      hold on;
   % Saves image of data summary
      extension = '.tiff';
      name = [cantilever, sampletype, filename1, extension];
      if (save==1);
         saveas(gcf,name);
      else end;

% Deletes data from summary if fit is poor, if difference between discretely
% calculated values of E is > 0.33, and if minimum indentation is < 0.3r
      [a_all,b_all]=size(alldata);
      dataindex2=1
      for dataindex2=1:a_all;
         if (alldata(dataindex2,12) > 0.33);
            alldata(dataindex2,:)=0;
            display('Large difference in E');
         else end;
         if (alldata(dataindex2,16) < 0.30);
            alldata(dataindex2,:)=0;
            display('Smallest indentation too shallow');
         else end;
         if (alldata(dataindex2,28) > 1.0);
            alldata(dataindex2,:)=0;
            display('Large strain-thin film correction required');
         else end;
         if (alldata(dataindex2,29) > 1.0);
            alldata(dataindex2,:)=0;
            display('Large strain-thin film correction required');
         else end;
      dataindex2=dataindex2+1
      end;
      alldata = sortrows(alldata);
      index=find(alldata(:,1) == 0);
      alldata(index,:)=[];
   % Plots Stiffness vs. indentation depth
      subplot(2,2,1);
      plot(alldata(:,16),alldata(:,10),'b+',alldata(:,17),alldata(:,11),'b+');
      xlabel('Indentation/Radius');
```

```
    ylabel('E_d_a_t_a (kPa)');
  % Plots Model Calculated Stiffness vs. Average Indentation of Radius
    subplot(2,2,2);
    plot(alldata(:,19),alldata(:,15),'b+');
    legend('all','compiled');
    xlabel('Average Indentation/Radius');
    ylabel('E_m_o_d_e_l (kPa)');
  % Plots Maximum Indentation as a % or R vs. Difference between
  % model calculated value of E
    subplot(2,2,3);
    plot(alldata(:,12),alldata(:,17),'m+');
    legend('all','compiled');
    xlabel('Difference of E values');
    ylabel('Maximum Indentation (% or R)');
  % Plots difference between indentations vs. Difference between
  % calculated values of E
    subplot(2,2,4);
    plot(alldata(:,12),(alldata(:,17)-alldata(:,16)),'m+');
    legend('all','compiled');
    xlabel('Difference of E values');
    ylabel('Differential Indentation (% of R)');
  % Saves image of data summary
    filename2='allgooddata';
    extension = '.tiff';
    name = [cantilever, sampletype, filename2, extension];
    if (save==1);
       saveas(gcf,name);
    else end;
  % Plots differences between corrected and calculated E (Yoffe vs. Hertz) vs.
indentation ratio
    figure;
    subplot(2,2,1);
    plot(alldata(:,16),alldata(:,26),'b+',alldata(:,17),alldata(:,27),'b+');
    xlabel('Indentation/Radius');
    ylabel('Diff of E_c_o_r_r vs. E_c_a_l_c (%)');
  % Plots Model Calculated Stiffness vs. Average Indentation of Radius
    subplot(2,2,2);
    plot(alldata(:,16),alldata(:,28),'b+',alldata(:,17),alldata(:,29),'b+');
    xlabel('Indentation/Radius');
    ylabel('Strain');
  % Plots Maximum Indentation as a % or R vs. Difference between
  % model calculated value of E
    subplot(2,2,3);
```

```
    plot(alldata(:,15),alldata(:,30),'m+');
    xlabel('E_H_e_r_t_z');
    ylabel('% of Thickness Strained');
  % Saves image of data summary
    filename3='allgooddata2';
    extension = '.tiff';
    name = [cantilever, sampletype, filename3, extension];
    if (save==1);
       saveas(gcf,name);
    else end;

% Calculates average model-calculated value for stiffness, Es (kPa)
% with standard error for data that fit well to model
    [size1,size2]=size(alldata);
    Es_avg=mean(alldata(:,15))
    Es_SE=std(alldata(:,15))/((size1)^0.5)
    n2=size1
    alldata(size1+1,15)=Es_avg;
    alldata(size1+2,15)=Es_SE;
    alldata(size1+3,15)=n2;
% Saves all good data to spreadsheet
    extension = '.xls';
    name = [cantilever, sampletype, filename2, extension];
    if (save==1);
       wk1write(name,alldata);
    else end;

% Indicates the end of the algorithm
    disp('Game Over');
return
```

Appendix 6. Preparation of UV-Softening Substrates for Cell Culture Studies

Materials:

1. HMW-polyacrylamide (PAAm, 600,000 – 1,000,000), 10% in water
2. Hydrazine hydrate (HH), 25% in water
3. Glass coverslips: 22 mm diameter and 45 x 50 mm, #1
4. Dimethyldichlorsilane (Supelco, Bellefonte, PA)
5. 1.0N NaOH
6. 3-Aminopropyltrimethoxysilane
7. Gluteraldehyde (70%)
8. Boric acid (BA), 10 mM solution at pH 12.0
9. 2-(N Morpholino) ethane sulfonic acid (MES), 0.1 M solutions at pH 6.0
10. Dimethyl sulfoxide (DMSO)
11. 12 x 75 mm culture tubes
12. 4-Bromomethyl-3-nitrobenzoic acid (BNBA)
13. 1-Ethyl-3-(3-dimethylaminopropyl) carbodiimide HCL (EDC) weighed in small, dry aliquots upon receipt and stored in freezer with desiccant
14. Acrylamide (40%, Bio-Rad)
15. Bis (2%, Bio-Rad)
16. TEMED (Bio-Rad)
17. Ammonium persulfate (Bio-Rad) solution, 10 mg in 100 µl distilled water prepared immediately before use
18. Acrylic acid N-hydroxy succinimide (NHS) ester (Sigma-Aldrich, St. Louis, MO)
19. 1X and 10X PBS
20. Channel dishes

Methods:

I. Creation of PAAH (polyacrylamide modified with hydrazine hydrate).

1. Pipette ~1 ml HM-PAAm from bottle into 1.5 ml centrifuge tubes and dry in speed vacuum at high heat for more accurate weight determination. Cap the tubes and store desiccated in freezer until use.
2. Weigh entire contents of one tube of the dry PAAm and place in 15 ml glass centrifuge tube. Repeat 5 times.
3. Dissolve each tube of PAAm in HH at a final concentration of 26.4 mg/ml (this follows the protocol in *Methods in Enzymology* to create partially substitute PA with acyl hydrazide groups, PAAH, at ~0.9 µmol HH/mg PA). Wear gloves and avoid contact with HH.
4. Cover with parafilm and incubate for 3 hrs in a water bath at 50˚C. Vortex at 20 minute intervals to thoroughly dissolve the PAAm, or mix if possible.

5. Precipitate each with 3 volumes ice cold MeOH and centrifuge at 15,000 rpm for 20 min (Sorvall RC28S centrifuge with F-28/50 rotor and temperature settings of 4 – 25˚C).
6. Remove excess MeOH and repeat step 5 if needed once or twice to form pellet and remove the MeOH.
7. Wash (3 x 10 min each) with 2 ml MeOH and remove excess MeOH. Centrifuge instead, if necessary.
8. Cover tube with parafilm and dry with N2 under hood to remove residual MeOH.
9. Rehydrate pellet in ~3 ml distilled water, stir at room temperature until completely dissolved. This may take overnight and several rounds of vortexing.
10. Pipette ~1 ml each of completely dissolved PAAH solution into 1.5 ml centrifuge tubes.
11. Dry PAAH in speed vacuum on high heat until dry.
12. Cap tubes and store desiccated at –20˚C.

II. Coverslip activation and preparation:

1. Preparation of bottom coverslips:
    a. Mark one side of #1 coverslip (45 x 50 mm).
    b. Thoroughly flame coverslips and place on rack.
    c. Smear 1.0N NaOH and let air dry.
    d. Smear 3-aminopropyltrimethoxysilane over surface and let sit for 5 minutes in chemical hood.
    e. Wash twice on shaker in distilled water.
    f. Cover surfaces with 0.5% glutaraldehyde (for 16 coverslips, use 15 ml distilled water and 107.1 μL of 70% gluteraldehyde) and incubate for 30 min. Wear gloves and avoid contact with glutaraldehyde.
    g. Wash twice in distilled water and let air dry.
    h. Store in desiccator at room temperature until use.
2. Preparation of top coverslips:
    a. Coat 22 mm diameter coverslips on both sides with dimethyldichlorsilane. Wear gloves and do this in chemical hood. Let air dry.
    b. Wash coverslips in distilled water.
    c. Wipe off excess residue with Kim Wipe.
    d. store in desiccator at room temperature until use.

III. Creation of UV-cleavable gel:

1. Make fresh buffer solutions or adjust pH of relatively fresh buffers:
    a. Make a 10 mM solution of BA (61.8 mg/100ml), adjust pH to 12.5 with KOH.
    b. Make a 100 mM solution of MES (1.952g/100ml), adjust pH to 6.0 with NaOH.
2. First Reaction of PAAH and BNBA (crosslinking to create PAAH-NBA):
    NOTE: Do the remaining steps of this protocol with the overhead lights turned off.

a. Dilute PAAH in BA at desired concentration (40-60 mg/ml), stir in a 12 x 75 mm glass test tube until completely dissolved (can take up to 15 min with periodic vortexing).
b. While vortexing, add a 5% (w/v) solution of BNBA in DMSO slowly to 3 volumes of BA. The BNBA will not dissolve in BA alone and the BNBA/DMSO will get cloudy with the addition of BA, presumably from partial precipitation. Therefore, mix this fresh and use immediately.
c. Add BNBA solution to PAH solution at the desired molar concentration (0.7 – 1.3 molar ratio of BNBA: theoretical HH, or add volume of BNBA, µl = 4.92*molar ratio*mg PAAH), cover and stir for 2 hours.

3. Neutralize reaction with MES and add supplemental PAAH:
   a. Stop reaction with addition of MES (pH = 6.0) in equal volume to all BA. Stir.
   b. Add additional dried PAAH (weight equal to half the initial PAAH used) and dissolve completely (with mixing and periodic vortexing can take up to 15 minutes).
   c. Degas the solution for ~10 min.
4. Create crosslinked, UV-sensitive gel atop activated coverslip:
   a. Remove EDC aliquot from freezer and allow equilibration to room temperature before opening or mixing. Dissolve EDC in MES at selected concentration (10-30 molar ratio of EDC:BNBA) immediately before use.
   b. Pipette 8 µl EDC solution into individual 12 x 75 mm glass test tubes.
   c. Clip end of pipette slightly and pipette 42 µl PAAH-NBA into tube, mix immediately a few times, then add same volume onto activated CS, flatten immediately with 22 mm top coverslip. Allow crosslinking reaction (carboxyl groups of BNBA to amine groups of supplemental PAAH by EDC) to proceed for 30 minutes.
   d. Soak substrates in 1X PBS and gently remove top CS.
   e. Wash (3 x 10 min each) in 1X PBS.
5. Polymerization of top layer of PA with acrylic acid derivative (NHS-ester):
   a. Add the desired volume of 40% acrylamide solution: 200 µl
   b. Add the desired volume of 2% bis-acrylamide solution: 30 µl
   c. Add 100 µl of 1X PBS
   d. Add 2 µl TEMED
   e. Add 468 µl water
   f. Add stir bar and place on magnetic mixer.
   g. Check pH of solution (it will be around pH 10-11)
   h. Add 0.1N HCl (drop by drop) until pH is 7.4 +/- 0.3
   i. Add 50 µl of FN (diluted at 1 mg/ml for 50 µg)
   j. Add 10 µl beads if necessary. Sonicate first for ~2 min.
   k. Add 1 ul of NHS-ester (aqueous dilution at 10 mg/ml) (the ester is toxic, wear gloves when handling this chemical!!) Once you are done measuring the ester, put the bottle back in the refrigerator immediately.

l. Adjust volume to 999.5 µl.
m. Degas for 20 minutes.
n. Add 5 µl of Ammonium Persulfate solution (100mg/ml) and mix gently.
o. Pipet 30 µl immediately onto activated coverslips and cover with a 22 mm top coverslip.
p. Wait 15 minutes. Assemble substrates into channel dishes. Soak in 1X PBS briefly to remove the coverslips.
q. Rinse 3x quickly with PBS.
r. Wash with PBS for 10 min.
s. Store in PBS in refrigerator until use or proceed with cell plating.

IV. Cell plating:

1. Equilibrate with 1 ml media for 45 min to block non-specific binding.
2. Replace media (2 ml)
3. Add cells and incubate overnight.